Palaeoenvironmental reconstruction of late Holocene climate dynamics in Southwest Africa using a multi-proxy characterization of Namaqualand mudbelt sediments

Robyn Granger

Thesis presented for the Degree of

Master of Science

in the Department of Environmental & Geographical Science

UNIVERSITY OF CAPE TOWN

January 2016

Acknowledgments

Firstly, I would like to thank my primary supervisor, Prof. Mike Meadows for his advice and support throughout the project. Prof. Meadows introduced me to the world of palaeoenvironments, and steadily pointed me in the right direction throughout my studies. I am also eternally grateful to my co-supervisor, Dr. Enno Schefuß, who tirelessly assisted me in pursuit of my goals, teaching me as much about what, why, how and when to write up scientific research, as he did about organic geochemistry and data interpretation. Constantly setting aside time to critique my work despite being on the other side of the world, he pushed me to achieve my very best, while still managing to crack a joke or two in between conversations about upwelling systems. The outstanding editorial skill of these two scientists has improved the quality of this thesis by several degrees, as has the input from my additional co-supervisor, Dr. John Compton, whose knowledge of marine geology in South Africa is unsurpassed.

Furthermore, I acknowledge the contributions of the following members of Marum, Bremen, to this research: Dr. Matthias Zabel, for facilitating my travel between universities, as well as contributing to discussions surrounding my research; Dr. Annette Hahn, for sharing her data as well as her access to the university kayak club; Ralph Kreutz and Jens Hefner, for patiently assisting me in the laboratory; Dr. James Collins, for his insight into my data and his encouragement; and my German office-mates Nicole Herrmann and Xuequin Zhao, who always answered my questions with thoughtfulness and enthusiasm. Further thanks are due to Jore von Holdt at UCT, for her assistance in the laboratory.

This project would not have been possible without the aid of generous funding received from the National Research Foundation (NRF), Deutscher Akademischer Austauschdienst (DAAD), and the University of Cape Town Postgraduate Funding Office. The financial assistance provided by the NRF in assistance of this Master's study is hereby recognised.

Contents

List of Figures

List of Tables

Glossary

A list of commonly used terms in this thesis.

Term	Definition
BCE	Before Common Era (equivalent to BC in calendar years)
BUS	Benguela Upwelling System (see Chapter 1: 3 for the full list of features associated with this marine system)
C_3	Calvin Cycle (C_3, C_4 and CAM are all methods of carbon fixation in plants)
C_4	Hatch-Slack Cycle
CAM	Crassulacean acid metabolism
CE	Common Era (equivalent to AD in calendar years)
FB	Fynbos Biome (South Africa)
LIA	Little Ice Age (a Northern Hemisphere term for the cool epoch that existed from ca. 1300 - 1850 CE)
MCA	Medieval Climate Anomaly (a Northern Hemisphere term for the warm epoch that existed from ca. 950 - 1250 CE)
SK	Succulent Karoo Biome (South Africa)
SRZ	Summer Rainfall Zone
SST	Sea surface temperature
VPDB	Vienna Pee Dee Belemnite standard
VSMOW	Vienna Standard Mean Ocean Water standard
WRZ	Winter Rainfall Zone

Abstract

Despite the recognized importance of understanding late Holocene climatic changes in southern Africa, a dearth of available evidence has resulted in a fragmented view of the recent past. South Africa has been identified as a key focus region for palaeoclimatic studies, as it reflects the dynamics of both tropical and temperate climate regimes. This study aims to create a catchment-integrated view of palaeoenvironmental conditions in the country's Winter Rainfall Zone (WRZ) and Southern Benguela region during the late Holocene, in order to establish the linkages between oceanic and terrestrial climate components. A multiproxy analysis was conducted on a west coast mudbelt sediment core, where continuous deposition over the last 2,250 years has aided the production of an uninterrupted age model. Alkenone and isotopic analyses were conducted at a multi-decadal resolution to assist in the reconstruction of sea-surface temperature (SST) in the St. Helena Bay region, and hydrological variation in the WRZ. Changes in moisture availability were inferred via the application of inorganic proxies, including grain size variation (promoted through the use of an end-member proxy algorithm) and the Fe/K ratio, a proxy interpreted to be representative of changes in chemical weathering. Furthermore, a newly-developed proxy, TEX_{86}, was used as an alternative palaeothermometer. TEX_{86} produced an additional record of SST, independent of alkenones, eliciting a comparative study between SST_{TEX86} and $SST_{UK'37}$. The comparison facilitated a review of the effectiveness of TEX_{86} within the Benguela Upwelling System, and assisted in quantifying reasons for the observed differences between the two methods. The results of the multiproxy analysis shed new light on southwest African late Holocene climatic dynamics. This study documents a decrease in SST accompanied by increasing WRZ rainfall, which is hypothesized to be a result of large-scale changes in the position and/or intensity of the austral westerly wind belt. A northerly migration/increase in intensity of the winds acts to produce cooler SSTs and wetter west coast continental conditions, both of which were most acutely experienced during the Little Ice Age (LIA) (1300 – 1850 CE). Zonal symmetry across the Southern Hemisphere is hypothesized to be a consequence of the large geographical extent of the westerly winds, as cooler and wetter conditions have been experienced in coastal,

winter-rainfall areas of Chile and Australia. Only subtle changes in vegetation were observed in the region, and the δ^{13}C and δD records chiefly reflected changes in water use efficiency. However, δD also reflects significant spatial variation of rainfall within the WRZ, with a shift towards isotopically-enriched rainfall in coastal regions that evolved during the last millennium. Finally, the recently-developed SST proxy, TEX_{86}, was determined to be an unreliable indicator of Southern Benguela SSTs, but may instead be relevant as a gauge for productivity variation. This study enriches the late Holocene palaeoenvironmental history of South Africa's WRZ, and demonstrates the linkages between oceanic and continental processes. Furthermore, several indications of inter- and intra-hemispheric relationships between southwest Africa and other continents reveal intriguing avenues for future research. These include investigations into the driving mechanisms of Northern and Southern hemispheric late Holocene climatic change, as well as exploring the large- and fine-scale controls on upwelling systems during this time.

Key words: Palaeoclimate; Benguela; Holocene; SST; Mudbelt; Rainfall; Southwest Africa; Winter Rainfall Zone; Inter-hemispheric linkages; Organic geochemistry.

Part I

Introduction

1 Southern Africa during the late Holocene

Once considered a relatively stable period during the late Quaternary[1], the Holocene is now recognized as an epoch that displays considerable climate variation throughout the last several thousand years (Mayewski et al. 2004). Reconstructions of the late Holocene are particularly vital as, in addition to providing a perspective on the nature of climate dynamics, they offer insights into the complex relationship between humans and the environment in which they live. Examples of societal collapse due to rapid climate change have been evidenced through the drought-related demise of the Mayan civilization around 1200 years ago as well as the breakdown of Greenland colonies during the Little Ice Age (LIA) (1300 - 1850 CE) (Mayewski et al. 2004). Climate fluctuations during the late Holocene are also arguably the best indicators of what to expect with regards to near-future climate conditions, and can serve as critical input data for models.

However, palaeoenvironmental conditions in southern Africa remain relatively unknown due to the scarcity of available evidence. Key to addressing this lack of knowledge is determining environmental changes within the Winter Rainfall Zone (WRZ). This area occupies the south west of South Africa, and due to its latitudinal position, records changes in both tropical and temperate climate regimes (Carr et al. 2006; Chase et al. 2013). Furthermore, the region's proximity to the cool Benguela Current leads to complex ocean-atmosphere interactions which significantly affect climate. There is thus an increasing need for palaeoenvironmental reconstructions of southwest Africa, not only to increase the accuracy and robustness of future model outputs, but also to understand the

[1]The geological epoch known as the Quaternary represents the last 2.6 million years (Pillans & Naish 2004). The Holocene epoch is a small subsection within the Quaternary, representing the last 11.5 ka years.

nature of the past and present relationships between oceanic and continental variables more comprehensively (Gersonde et al. 2005; Haberzettl et al. 2007).

The thesis presented here aims to address this knowledge deficit, by establishing a novel outlook on oceanic and terrestrial climatic changes in the WRZ during the late Holocene. Specific aims and objectives are subsequently outlined in this chapter.

2 Ages and time periods

The ages reported here are derived from ^{14}C dates. These have been converted to calendar ages, with the suffix "CE" (1950 CE = 1950 AD). Note that in figures, the number -250 CE is used as an equivalent to 250 BCE. The term "late Holocene" is used to cover the last 2,250 years, a period which encompasses the LIA (1300 – 1850 CE) and the Medieval Climate Anomaly (MCA = 950 – 1250 CE) (Mann et al. 2009; Nicholson et al. 2013). The term "ca." is used to indicate the approximation of a date; this approximation takes into account age model uncertainty; therefore, when referring to variation in GeoB8323-2, this study rounds to the nearest 50 years.

3 The Benguela Upwelling System

Although the mechanisms of the modern Benguela Upwelling System (BUS) have been well studied (eg. Nelson & Hutchings 1983; Demarcq et al. 2003; Weeks et al. 2006; Hutchings et al. 2009), the relationship between oceanic and continental climate during the late Quaternary has not yet been fully resolved. The BUS is a complex oceanographic system, chiefly known for its high levels of productivity and northward-flowing eastern boundary current. Situated roughly between 14°-37°S (Shannon & Nelson 1996), the system includes the following elements (shown in Figure 1):

i. the Benguela Current;

ii. the coastal upwelling system;

iii. the Poleward Undercurrent;

iv. the mudbelt;

v. multiple upwelling cells and filaments;

vi. the eastern limb of the South Atlantic Gyre; and

vii. warm water perturbations that enter the region through Agulhas Rings.

The Poleward Undercurrent and the mudbelt are briefly described here in order to explain the value of the palaeoenvironmental records from this region. Other particular features are discussed in later chapters, where relevant.

Sediment arriving at the mouths of West Coast Rivers is moved southwards via the Poleward Undercurrent, and contributes to the formation of the mudbelt. The mudbelt therefore contains records of both oceanic and terrestrial conditions, and is a feature that demonstrates high potential for palaeoclimatic reconstruction. Marine cores sampled in this region may help to redress the problems of non-continuous deposits and hiatuses in age models, which occur in terrestrial cores. There is less erosion on the coastal shelf than on land, and the deposition of fluvially-transported material gives rise to broad, catchment-integrated signals. Unfortunately, there are relatively few Benguela studies from the late Quaternary, despite the research cruise M57/1 *Meteor* successfully recovering several cores off the west coast of South Africa and Namibia (see Herbert & Compton 2007). These cores have arguably been underutilized; although recovered in 2003, organic geochemical analyses were only performed on GeoB8323-2 in 2014.

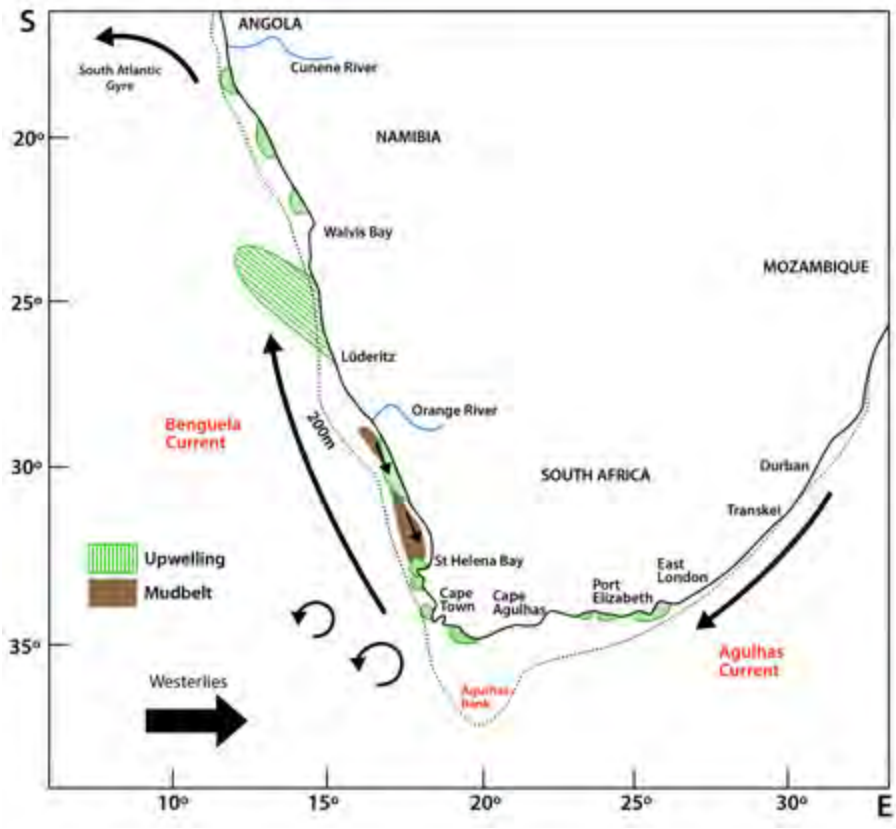

Figure 1: A schematic diagram of Southern African oceanographic, climatic and sedimentological features (adapting features identified in *Hutchings et al. 2009*). Important features of the Benguela Upwelling System include the equatorward-flowing current, multiple upwelling cells (shaded green), a poleward return flow of water along the west coast, the west coast mudbelt, and warm water perturbations entering the system via Agulhas Rings (circular arrows). The system's boundary current forms the eastern arm of the anticlockwise-flowing South Atlantic Gyre (top left), and the austral westerly winds (bottom left) blow over the Southern Ocean, migrating latitudinally over long- and short-term time scales.

4 Existing terrestrial and oceanic palaeoenvironmental research in southwest Africa

Existing palaeoclimate data from terrestrial sites has provided some idea of the hydrological and vegetative conditions in the WRZ during the Holocene (eg. Meadows et al. 2010, Chase et al. 2013). Proxies are often used in combination, and include stable isotopes (carbon, hydrogen, nitrogen and oxygen), pollen, diatoms, and charcoal. These studies have helped to build up a more robust view of changing environmental conditions during the late Quaternary.

Sites relevant to this study are shown in Figure 2. Sediments from the coastal lake Verlorenvlei have been successfully used in the reconstruction of Holocene environments (Meadows et al. 1996; Meadows & Baxter 2001; Stager et al. 2012; Carr et al. 2015), and the relatively recent technique of using hyrax middens in various isotopic analyses has resulted in an increasing number of viable mountain sites being identified in the region (Meadows et al. 2010; Quick et al. 2011; Chase et al. 2013; Valsecchi et al. 2013). The majority of these studies provide datasets for relatively small regions, and are sometimes unable to resolve variation at a scale necessary for the observation of rapid climate changes (ie. decadal or bi-centennial). In addition, there remains ongoing discussion surrounding the driving factors of proxy records used in hydrological reconstructions. The relative strengths of these factors appear to rely heavily on site location, and as there exist limited catchment-scale studies, research has thus far been unable to resolve this issue.

Despite this, several climate trends have been identified on the basis of existing research. Findings from hyrax middens at the De Rif site suggest that the last 2,200 years have been significantly more humid than during the early to mid- Holocene (Valsecchi et al. 2013). However, isotopic analysis of hyrax middens from the mountain sites of Katbakkies Pass and Truitjes Kraal indicate a shift from wet conditions (450 BCE – 650 CE) to dry conditions (650 CE – 1350 CE) (Meadows et al. 2010). Consistent with these results, a prominent shift from wet to dry is again revealed through the analyses of a

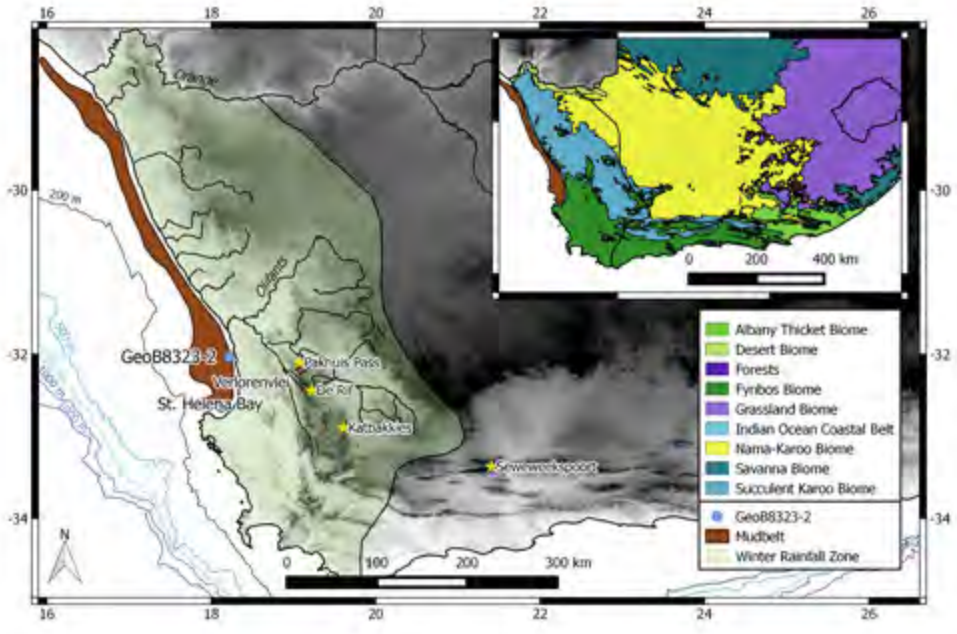

Figure 2: Map of southwest Africa, showing the position of Core GeoB8323-2 (blue circle). The map shows height above sea-level, which is overlain by the Winter Rainfall Zone. Also featured are West Coast rivers, sites mentioned in text (stars), the mudbelt from which GeoB8323-2 is sourced, the continental shelf (200m) and bathymetric contours (500m intervals). The vegetative biomes of South Africa are displayed in the top right corner using data from *Mucina & Rutherford (2006)*.

second hyrax record recovered from Katbakkies Pass (Chase et al. 2015). However, in this record, aridity increases from ca. 350 CE, resulting in a discrepancy of some 300 years which the authors attribute to differences in age models and sampling resolution (Chase et al. 2015).

A shift towards more arid conditions from ca. 50 CE is also documented in the coastal regions of the WRZ, where a Verlorenvlei diatom record is interpreted as showing relatively dry conditions (Meadows & Baxter 2001). The authors attributed recent diversification of pollen spectra in core-top sediments to human disturbance, but freshwater inputs during this time are also indicative of increased humidity. In correspondence with this, a high resolution diatom study by Stager et al. (2012) proposes a more humid climate in the Verlorenvlei region during the last several hundred years (1250 - 1950 CE). A short period of aridity occurred around the time of the MCA, before rainfall increased at ca. 1000 CE. Precipitation in the Verlorenvlei region rose notably during the LIA, a conclusion that is reiterated by Hahn et al. (2015), whose multiproxy analysis of two marine cores exhibit wet periods at ca. 50 CE and 1450 CE. Furthermore, like Stager et al. (2012), Hahn et al. (2015) identified a distinctly arid WRZ signal coinciding with the time of the MCA, despite the climatological effects of the epoch being recognized as less widespread than the LIA.

Links such as these affirm strong connections between oceanic and atmospheric systems in southwest Africa and other systems further afield. Precipitation in the WRZ increases during times of sea-ice expansion (Antarctic cold events), with the Southern Hemisphere mid-latitude westerly winds hypothesized to have moved northwards or intensified during these times (Stuut et al. 2004; Chase et al. 2013; Hahn et al. 2015). Sea-ice and winds are also closely tied to the position of the ocean fronts, which migrate parallel to the winds (Stuut et al. 2004). Thus it is likely that the winds associated with winter cold front systems lay to the north of their present position and/or were most intense during the LIA (Hahn et al. 2015). Since then, Weldeab et al. (2013) posit that the westerlies (and ocean fronts) have been shifting southwards, decreasing rainfall

amount in the WRZ. The inter-relationships between the ocean and atmosphere in this region advocate for a greater number of multiproxy studies which explore the connections between the WRZ and BUS.

Prior to this study, palaeoceanographic conditions had not been determined south of 29°S (Leduc et al. 2010). The role of the most southerly section of the BUS during the Holocene thus remains relatively unknown, and the two studies that have been conducted by Farmer et al. (2005) and Leduc et al. (2010) have demonstrated that variability within the BUS is not uniform. Offshore of the Orange River, SST was at a maximum at 1250 CE and 50 BCE, which exhibited coeval negative trends with Morocco and a positive correlation with Greenland. Further north, within the Lüderitz upwelling cell (Figure 1), the more coarsely-resolved record showed a minimum at 1250 CE and maximum at 1300 and 1900 CE. In addition, variation in SST offshore of Namibia showed an amplitude of double that of the region off the coast of the Orange River. The lack of correlation between the two datasets is recounted in more detail in Chapter 2.

This contrast is compounded by the absence of further data, and has left several questions relating to the BUS largely unexplored. What significant oceanic changes were experienced along the southwest coast during the past few thousand years? Has variation in the BUS been driven predominantly by local forcing factors such as bathymetry and local winds, or have larger-scale atmospheric features exerted a substantial influence? What effect, if any, have changes in the interaction between the Benguela and Agulhas Currents had on the upwelling system? This study is aimed at answering some of these questions surrounding the BUS during the late Holocene, and to link oceanic variation with hydrological and vegetative changes that occurred in southwest Africa.

While a comprehensive and detailed assessment of late Holocene climatic changes in southwest Africa remains elusive, the studies reviewed here suggest that some progress has indeed been made towards a better understanding of late Quaternary dynamics. They have revealed meaningful insights into the hydrology, vegetation, and oceanic conditions of the region over the last few thousand years, and have also begun to draw connections

between local variation and changes in Southern Ocean and Antarctic influences and other drivers of climate variability.

5 Site setting

Core GeoB8323-2 is located within the southern section of the west coast mudbelt, within the BUS and in close proximity to St. Helena Bay (Figure 2). The mudbelt is thin at this latitude (in comparison to the north), and has a depth range of between 80 and 140m (Gray et al. 2000; Herbert & Compton 2007). The coordinates of GeoB8323-2 are 32°01.89 S and 18°13.19 E, positioned just south of the mouth of the Olifants River, in water depth of 92 metres.

6 General objectives and research questions

There is a need for increased high-resolution, multi-proxy palaeoclimate datasets in order to build up a clearer picture of climate variation in the WRZ during the late Holocene. This study aims to establish a high resolution continuous record of Benguela Current SSTs over the late Holocene period, and to examine the interactions between oceanic and continental processes that existed during the late Holocene.

For this thesis, four research questions were identified in relation to the characteristics of sediments in GeoB8323-2:

1. What trends and variability in SST have been observed over the past 2,250 years?
2. What are the drivers of change in isotopic composition in the WRZ, and what inferences can be made regarding terrestrial changes in hydrology and vegetation type during this time?
3. How do the identified marine and terrestrial proxy records compare with one another, and how do they compare with what is known about regional and global

climate dynamics during this time? Are the conclusions drawn from this study of southwest Africa applicable at a wider geographical scale?

4. How do TEX_{86} SST results compare with those obtained via the $U^{K'}_{37}$ method? What accounts for differences between the records and what does this mean for further GDGT studies in the St. Helena Bay region?

7 Format of this thesis

This thesis is divided into 5 chapters (parts I - V). Chapters 2 and 3 of this thesis are structured as standalone scientific papers (submitted and soon to be submitted to peer-reviewed journals) relating to changing climatic conditions in southwest Africa. These papers make use of multiple proxies to reconstruct oceanic and continental climate dynamics of this region during the late Holocene. The paper in Chapter 2 is entitled *Coupling between late Holocene sea surface temperature and terrestrial hydrology in southwestern Africa*, and is predominantly marine-focused. The paper in Chapter 3, *Controls on $\delta^{13}C$ and δD in South Africa's Winter Rainfall Zone during the late Holocene*, focuses more on terrestrial variation and the utility of isotope analysis within the region of southwest Africa. Combined, the two papers present a comprehensive view of palaeoclimatic changes in the WRZ, using a multi-proxy approach. Methods include stable carbon and hydrogen isotope analyses, alkenone-SST analyses, grain size analyses, end-member analyses, and elemental ratio analyses.

Whilst now an integral part of this thesis, the status of these two chapters as standalone scientific papers, with separate abstracts, acknowledgments and references, has been preserved. Therefore, although some similarity of material exists between the two in certain sub-sections, this material has been retained, giving rise to some degree of repetition that would not otherwise have been included.

Chapter 4 briefly describes the results of two additional proxy methods (TEX_{86} and Branched vs Isoprenoid Tetraether index), which were obtained from GeoB8323-2, and

are described separately. Chapter 5 summarizes the main findings of this thesis and discusses them with regards to the research objectives outlined in this chapter, as well as commenting on possible future research opportunities.

Part II

Coupling between late Holocene sea surface temperature and terrestrial hydrology in southwestern Africa

Robyn Granger [a], Michael E. Meadows [a], Annette Hahn[b],
Jan-Berend W. Stuut[b,c], Nicole Herrmann[b], Matthias Zabel[b],
Enno Schefuß[b]

[a]Department of Environmental and Geographical Science, University of Cape Town, South Africa

[b]MARUM – Center for Marine Environmental Sciences, University of Bremen, Bremen, Germany

[c]NIOZ, Royal Netherlands Institute for Sea Research, Texel, the Netherlands

Abstract

Southwest Africa is an important region for palaeoclimatic studies, being influenced by both tropical and temperate climate regimes. Despite the understanding of the climate of the recent past being critically important for studies of the near-future, relatively little is known about late Holocene climatic changes in this region, in particular regarding the linkages between oceanic and atmospheric circulation changes. To improve our understanding of these linkages we investigated a marine sediment core in the southernmost Benguela Upwelling System (BUS), in order to reconstruct climate in this region for the past 2,250 years. Our aim was to obtain records of sea surface temperature changes within the coastal upwelling zone, as well as hydrological variations in South Africa's Winter Rainfall Zone (WRZ). Alkenone analysis was used to acquire SST values, and grain size measurements in combination with geochemical analysis were conducted to reconstruct changes in fluvial sediment discharge and weathering intensity. Results show that this specific region of the Southern Benguela is distinctive from the remainder of the system. A trend towards lower SSTs was observed from about 700 CE onwards, culminating during the Little Ice Age (LIA, 1300-1850 CE). This was accompanied by increasing river discharge from the WRZ. A cooler southernmost BUS with increasing precipitation in the WRZ was driven by long-term changes towards a more northerly position of the austral westerly winds, emphasizing the impact of global climate changes on southwest Africa.

Keywords

Southwest Africa; Holocene; Hydrology; Marine sediments; Sea surface temperature; Grain size; End-member modeling.

1 Introduction

Southern Africa displays a dynamic late Holocene climate history (Walker 1990; Chase et al. 2013). Southwest African climate in particular is significant with regard to palaeo-climatic studies, primarily due to its latitudinal position between tropical and temperate climate zones (Chase & Meadows 2007; Chase et al. 2013; Hahn et al. 2015). However, despite the recognized importance of the region, Holocene climatic variability in south-west Africa remains relatively unknown. High resolution palaeo-climatic records during the late Holocene are sparse and palaeo-oceanographic records of adjacent coastal waters during this time period even more so. In addition, and of relevance due to increasing anthropogenic influences on proxy data and climate, Southern Africa is of substantial archaeological importance, with several human occupation sites existing along the country's west coast (Smith et al. 1991).

Due to this scarcity of continuous marine records in the region, the ocean-climate linkage in the Winter Rainfall Zone (WRZ) during the late Holocene has thus far not been fully established. In the past, research has been focused on climate changes at specific sites, but this study aims to provide a catchment-integrated signal. In order to improve our understanding of the late Holocene climate history of the WRZ and its relationship to oceanic changes, we investigated marine sediment core (GeoB8323-2), situated near St. Helena Bay in the west coast mudbelt to establish a continuous record of terrestrial and oceanic climate changes for the past 2,250 years. A high-resolution record of SST variations in the southwest region of the Benguela Upwelling System (BUS) is reconstructed using the alkenone-based $U^{K'}{}_{37}$ proxy. In addition, we determined hydrological changes on the adjacent continent using sediment grain size and elemental changes of discharged terrestrial material. With these records, we document the as yet unknown relationship between the marine and terrestrial climatic components of this region.

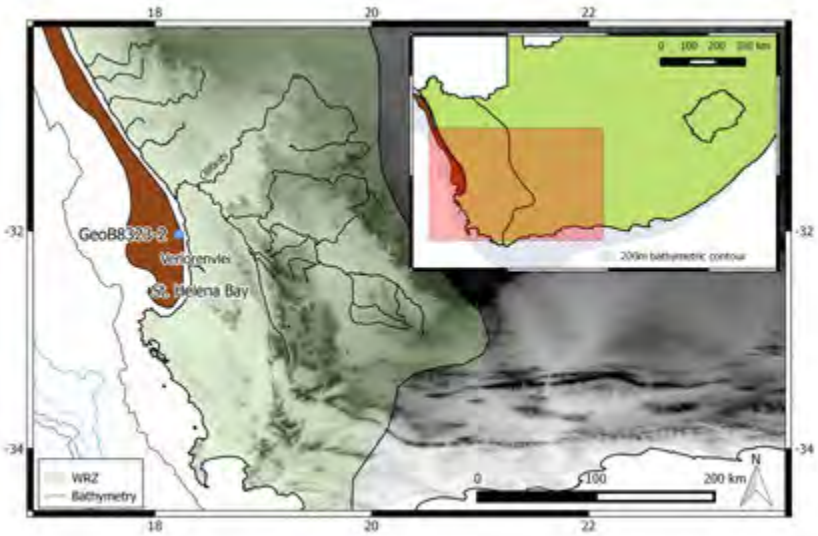

Figure 3: Map of southwest Africa showing the extent of the Winter Rainfall Zone (WRZ) within the greater South Africa region, and the rivers that drain towards the west coast of the country, including the Olifants River. GeoB8323-2 is located within the mudbelt at 32°01.89 S, 18°13.19 E. Bathymetric contours are 200m, 500m, 1000m, 1500m and 2000m. The core site is north of St. Helena Bay, and in close proximity to the estuarine lake Verlorenvlei.

1.1 Regional setting

South Africa is positioned between two ocean boundary currents: the warm western-boundary Agulhas Current and the cool eastern-boundary Benguela Current, and is influenced by both tropical and temperate water masses and climate systems (Tyson et al. 1996; Shannon & Nelson 1996; Chase & Meadows 2007; Chase et al. 2013). Tropical systems bring summer rainfall to the northern and eastern parts of the Summer Rainfall Zone (SRZ) where moisture from the Indian Ocean is the dominant source of precipitation (Chase & Meadows 2007). In contrast, the WRZ, a smaller, southwestern section, is affected by temperate climatic influences. Precipitation here occurs as a result of seasonal

northward shifts of the rain-bearing austral westerly winds around the southernmost tip of Africa (Tyson & Preston-Whyte 2000). Storm systems travel within the winds systems, precipitating moisture out over land.

In recent years there has been an increasing palaeo-climatological focus on the WRZ, partly due to the belief that local environmental changes (variation in precipitation, vegetation and adjacent ocean temperatures) within the WRZ are indicative of large-scale shifts in tropical and temperate climate zones (Carr et al. 2006; Chase & Meadows 2007). These shifts have been prominently documented over glacial-interglacial time scales, but they have also been shown to have significant effects on the Southern Hemisphere over millenial timescales. Noticeable changes during the last few decades have even been observed through satellite imagery (Toggweiler et al. 2006; Shindell & Schmidt 2004). It is unknown to what extent these modern-day changes are a result of anthropogenic effects, but the rapidity of the variation has given rise to the hotly-debated term, the Anthropocene, which is used to describe the era in which the consequences of human impact can be observed (Zalasiewicz et al. 2011). It is therefore becoming increasingly difficult to distinguish between natural cycles and those enhanced by humans; as a consequence modern data should be interpreted with caution.

The generally arid western half of southern Africa is traversed by several rivers, both seasonal and perennial, the largest of which is the Orange River, which borders South Africa and Namibia and drains a substantial part of the SRZ (Meadows et al. 2002) (Figure 3). All rivers within the 500 km coastal stretch between the Orange River and St. Helena Bay drain into the mudbelt on the shelf of southwest Africa, which is an important source of high-resolution sedimentary archives (Herbert & Compton 2007). The majority of the sediment is terrigenous in origin and transported by the Orange River, as well as by the more southerly Olifants and Berg Rivers and other small or ephemeral rivers in Namaqualand such as the Holgat, Spoeg, Buffels and Groen rivers (Herbert & Compton 2007; Leduc et al. 2010; Weldeab et al. 2013). Close to St. Helena Bay the Olifants River discharges a large catchment extending into the southern

WRZ. The fine terrestrial material derived from all rivers is transported southward along the inner shelf by the southward-flowing polar undercurrent (Herbert & Compton 2007). Coarser sand and gravel grains are deposited at the mouth of the Orange River are too heavy to be transported by the undercurrent, and follow the main path of the Benguela Current, moving northwards via long-shore drift (Garzanti et al. 2014).

Aeolian transport of material is not considered to be a significant factor at this location due to prevailing westerly wind direction. Contrary to locations further north, there is very limited dust export from southern Africa's west coast towards the southeast Atlantic. A latitudinal transect showing terrestrially-derived material off the southwest African coast demonstrates that very little dust is deposited in the Atlantic south of 20°S (Rommerskirchen et al. 2003). Furthermore, high-resolution satellite imagery from SeaWIFS identify almost no dust plumes occurring south of 28°S, ie. south of the Orange River mouth (Eckardt & Kuring 2005). In a separate study, satellite imagery was used to detect absorbing aerosols, and showed that although the Kalahari Desert currently is a large sand surface, there is very little dust activity in southwest Africa (Prospero et al. 2002). Regarding the deposition of dust from sources further north, Gingele (1996) notes that the prevailing wind directions in this region (southerly and westerly) account for the lack of marine aeolian-deposited material in this region, suggesting that only minor dust input into the southeast Atlantic has occurred during the last 4,000 years.

1.2 The Winter Rainfall Zone

Alongside the Benguela Current, a very steep north-south rainfall gradient along the western coast of South Africa promotes the existence of several biomes within the WRZ, namely, the Namib Desert, Succulent Karoo, Nama Karoo, and Fynbos Biomes (Cowling et al. 1999; Desmet & Cowling 1999) (Figure 3). This steep rainfall gradient is a contributing factor to the difficulty in establishing reliable, continuous palaeo-environmental records from the region; rainfall patterns at one location may not be representative of conditions further afield (Meadows et al. 2010). Due to the arid and semi-arid nature

of the WRZ, there is a general paucity of terrestrial sedimentary archives suitable for palaeo-climatological research (Chase et al. 2009).

Traditional methods of palaeoclimatological reconstruction are also hampered by the high relief environment resulting in prominent erosion, and extreme seasonality (Meadows et al. 2010). Nevertheless, several successful Holocene palaeoenvironmental reconstructions have been made from Verlorenvlei and the Cederberg Mountains (Meadows et al. 1996; Meadows & Baxter 2001; Stager et al. 2012; Carr et al. 2015). These studies have consistently identified low amplitude vegetation changes in the WRZ during the Holocene. More recently, pollen and isotope analysis of hyrax middens have revealed more continuous and detailed palaeoenvironmental evidence spanning the Holocene (Meadows et al. 2010) and even further back in time (Quick et al. 2011; Valsecchi et al. 2013).

Since the region is highly sensitive to hemispheric-scale climate changes, and links with the austral westerly winds have been documented (Chase & Meadows 2007; Stager et al. 2012; Chase et al. 2013; Weldeab et al. 2013; Carr et al. 2015), studies have drawn the conclusions that millennial-scale equatorward shifts in the westerly winds coincide with rainfall increases in the WRZ, whereas southward migrations lead to drier conditions. A sharp shift towards wetter conditions has been documented by several studies as having occurred at around 700 or 600 years ago, a period coincident with the Little Ice Age (LIA) (Stager et al. 2012; Meadows et al. 2010; Weldeab et al. 2013; Carr et al. 2015).

1.3 The Benguela Current

1.3.1 Upwelling

The BUS, one of the world's major upwelling zones, follows the southwest African coast between 17-34°S. The BUS is unique among Eastern Boundary systems since both its northern and southern boundaries consist of warm water systems, namely, the Angola and the Agulhas Currents (Shillington 1998; Demarcq et al. 2003).

A classical coastal upwelling system is one in which alongshore winds induce Ekman pumping of cool subsurface waters to the surface leading to enhanced primary production

and lower SST (Stewart 2009). In austral summer, when the South Atlantic anti-cyclone is farthest south, alongshore south-easterly winds induce near-shore upwelling accompanied by lower SSTs and higher primary productivity (Shannon & Nelson 1996; Hutchings et al. 2009). In contrast, during winter months, westerly winds affect the region, suppressing upwelling and subsequently leading to higher SSTs and lower productivity (Lamont et al. 2015).

1.3.2 St Helena Bay

St. Helena Bay, the southernmost part of the BUS, is a climatologically complex region due to its irregular coastline and close proximity to the warm Agulhas Current (Figure 3). The bay is the closest identifiable terrestrial feature, at a workable satellite-imagery scale, to the site of GeoB8323-2, lying 80 km south of the core, thereby affecting current flow in the area. The shape of the embayment promotes recirculation, which alters the natural equatorward flow of the equatorward current (Pitcher & Nelson 2006). For this reason, and also due to the proximity of strong upwelling near Cape Columbine to the south, and the Namaqua upwelling cell to the north, St. Helena Bay does not display a "classical" upwelling signal, but instead reacts to other forcing mechanisms that may not be significant in more northerly parts of the system (Pitcher et al. 2010; Dewar et al. 2012).

Despite not being situated within one of the multiple intense upwelling cells, which are prominent features of the BUS, the coastal section alongside St. Helena Bay still experiences strong near-shore upwelling inshore of the shallow 300m continental shelf upon which the mudbelt is formed (Lamont et al. 2015). Modern satellite-derived SSTs in St. Helena Bay range from 14.3°C in summer to 15.6°C in winter with a mean annual SST of 14.9°C (Locarini et al. 2013).

The interaction between the Agulhas Current and the BUS partly accounts for SST variations in St. Helena Bay, as warm Agulhas water can enter the BUS by means of warm-water "ring-shedding" at the point of Agulhas retroflection (de Ruijter et al. 1999;

Garzoli et al. 1999; Schouten et al. 2000). The amount of warm water entrained into the BUS is hypothesized by Hardman-Mountford et al. (2003) and Weldeab et al. (2013) to be regulated by changes in the position of the austral westerly wind belt: a northerly position of the westerlies is thought to limit the amount of warm water through-flow passing from the Agulhas to the Benguela waters, since in this position, the wind belt effectively "blocks" westward-moving rings (Rouault et al. 2010; Weldeab et al. 2013). Therefore, southward shifts in the westerly winds would allow for increased frequency of warm water incursions, thereby decreasing upwelling and productivity, and increasing SST. Although little research has been done regarding the interaction between terrestrial and oceanic palaeoclimate changes in this region, latitudinal changes in the westerly wind belt appear integral to both BUS SSTs and continental rainfall. Due to the southerly position of St. Helena Bay and the shape of the embayment, this location is ideal for observing westerly wind-related palaeoclimatic changes.

2 Methods

2.1 Chronology

Gravity core GeoB8323-2 was recovered during the M57/1 *Meteor* cruise in January/February 2003 from 32°01.89 S and 18°13.19 E. The core was taken from the west coast mudbelt at a depth of 92 metres water depth offshore the Olifants River on the west coast of South Africa.

An age model for GeoB8323-2 was published by Herbert & Compton (2007), and updated by Hahn et al. (2015) based on a linear-interpolation of 6 radiocarbon dates from bottom-dwelling gastropods and bivalves. The age model was established using a reservoir age of 146 ± 85 14C years (Dewar et al. 2012) and the marine calibration curve (Reimer 2013).

GeoB8323-2 is 2.85 m in length, but results from both Herbert & Compton (2007) and Hahn et al. (2015) indicate the presence of a hiatus in the lower part of the core (below

227cm). The sediment directly above the hiatus was dated to 337 years BCE (Herbert & Compton 2007). The sedimentation rate is consistently around 1 mm per year with the exception of the interval between 124 and 112 cm (766 - 832 CE) where the sedimentation rate nearly doubles to 1.8 mm per year.

2.2 Core sub-sampling

GeoB8323-2 is stored at the MARUM Core Repository at the University of Bremen, at a temperature of 4°C. For alkenone analysis, 43 samples were taken with an initial resolution of 5 cm (equivalent to an average sample resolution of 25 years) until 150 cm, below which a 10 cm resolution was used (ca. 100 years between samples). Sample volumes ranged from between 3 and 5 ml of sediment, with dry sample weights between 2.5 and 6.5 g. All samples were freeze-dried and manually ground by mortar and pestle before analysis. For grain size analysis, separate samples were taken, with the uppermost 114 cm of the core being sampled at 1 cm intervals; thereafter it was sampled every 2 cm until 226 cm. Samples for grain size analyses were air-dried before analysis. The upper core was sampled at a higher frequency than the lower in order to obtain a more detailed perspective of the recent past, particularly during the epochs referred to as the Medieval Climate Anomaly (MCA) and LIA.

2.3 Alkenone analysis

Ground samples were extracted via accelerated solvent extraction in a DIONEX ASE200 at 100°C and 1000 psi. A solvent mixture of dichloromethane (DCM): methanol (MeOH) = 9:1 was used for extraction. For extraction, 3 cycles of 5 minutes were run. Afterwards lipid extracts were concentrated by rotary evaporation, after which asphaltene was precipitated via column separation using Na_2SO_4. Following saponification with 0.1M KOH at 85ºC for 2 hours to remove wax esters which potentially interfere with alkenone quantification, neutral fractions were separated by column chromatography using 1%-deactivated silica and hexane to remove a hydrocarbon fraction and DCM to isolate a ketone fraction.

Alkenone unsaturation ratios were determined by gas chromatography/flame ionization detection (GC-FID) using a ThermoFischer Scientific Focus GC-FID at MARUM, University of Bremen. The GC-FID was equipped with a split/splitless injector and a 60m DB-5ms column. Analyses of an external alkane standard of known concentrations were performed repeatedly. Precision of compound quantifications based on replicate standard measurements (1σ) is 5%. The $U^{K'}_{37}$ method, based on the di- and tri-unsaturated C_{37} alkenones, is described in Prahl & Wakeham (1987). $U^{K'}_{37}$ is calculated using the following ratio:

$$U_{37}^{K'} = \frac{C37:2}{C37:2 + C37:3}$$

The index is converted to SST using the calibration by Müller et al. (1998):

$$SST = \frac{U_{37}^{K'} + 0.044}{0.033}$$

All samples were measured in duplicate, yielding an absolute $U^{K'}_{37}$ error of 0.010 $U^{K'}_{37}$ units, translating to a mean error in SST estimation of 0.09 °C.

2.4 Grain size and end-member analysis

Grain size analyses were performed using a Malvern® Mastersizer 2000, which resulted in 78 size classes, from 0.28 to 2000 μm. Grain size measurements were conducted in duplicate for each sample. An end-member modeling algorithm (Weltje 1997) was applied to the results of the grain size analysis in order to determine changes in relative proportions of characteristic size spectra (Weltje 1997). A detailed description of the method applied in this paper can be found in Stuut et al. (2004). The total variability accounted for by each of the end-member models is represented by r^2_{mean}, and this factor is used to determine the optimal number of end-members. A three end-member model was chosen for this study, where, r^2_{mean}= 0.70 (70% of variability is accounted for). EM1 represents the coarsest fraction and EM3 represents the finest fraction.

2.5 XRF-scanning:

XRF core scanning was performed on GeoB8323-2 in 2-cm increments using an Avaatech XRF Scanner at MARUM (University of Bremen). The counting time was 30 seconds, and the excitation potential and current were kept at 10kV and 250μA respectively. A more detailed description of XRF scanning methods can be found in Hahn et al. (2015). For this study we focus on the elemental ratio (Fe/K), which is minimally affected by variations in grain size and water content (Jansen et al. 1998; Kido et al. 2006; Bloemsma et al. 2012). Fe/K can be used as an indicator for chemical weathering as K is more easily leached from soils than less mobile elements such as Fe (Govin et al. 2012).

3 Results

3.1 Sea surface Temperatures

The SST record from GeoB8323-2 (32°S) off the west coast of South Africa reveals a clear decreasing trend over the last 2,250 years, with a rate of cooling of -0.1 ºC / 100 years (Figure 4a). This trend becomes more pronounced at around 700 CE, lasting until the present. Examination at shorter time scales reveals high amplitude variability overlaying the long-term cooling trend, with a temperature range of 5.6 ºC (Figure 4a).

The oldest part of the record reveals a steady decrease in SST from 250 BCE to 250 CE, followed by a sharp increase during the following 200 years. The period of largest variability is found between 950 and 1600 CE. During this phase, SSTs are shown to have changed by as much as 2 or 3 ºC in as little as 50 years, after which the record reveals the most recent 400 years to have been the coldest in the last 2,250 years. Despite the large range in SST variability, there are two periods of relative stability, from between 700 and 950 CE and between 1700 and 1850 CE. Peak SST was found to be 16.6 ºC, which occurred at around 900 CE, and minimum SST was recorded as 11.0 ºC (ca. 1600 CE).

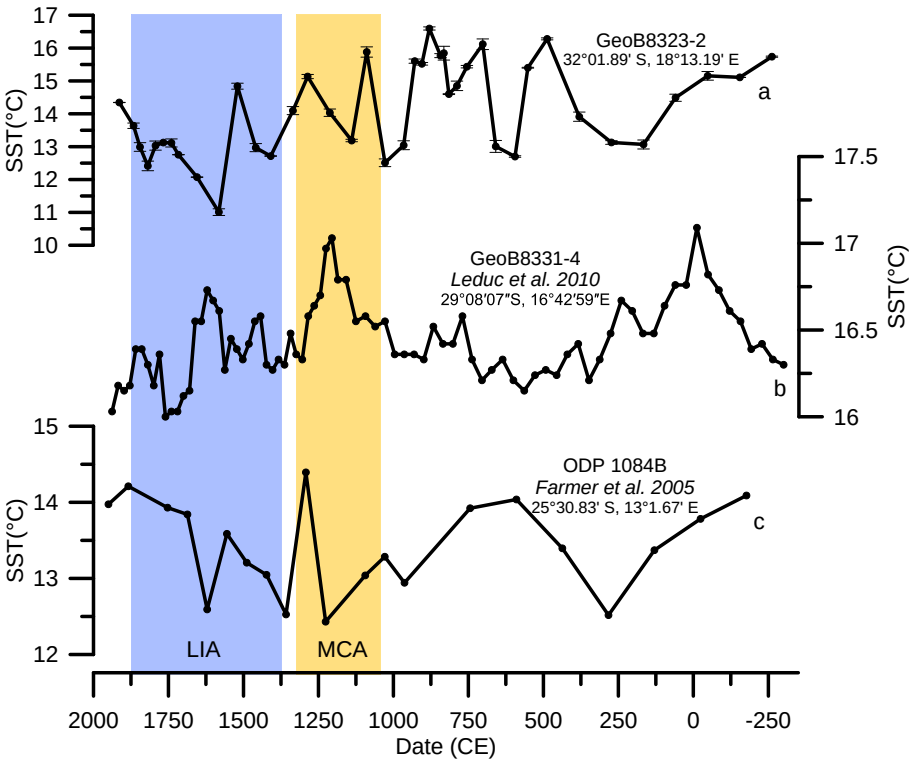

Figure 4: Benguela Current alkenone-derived sea surface temperature (SST) variations as reconstructed from (a) GeoB8323-2 (this study) and (b) GeoB8331-4 (Leduc et al. 2010), and Mg/Ca-derived SST reconstructed from (c) ODP 1084B (Farmer et al. 2005). Mean values of GeoB8323-2 obtained from duplicate runs are plotted, with error bars representing absolute deviations between the duplicate analyses. The intervals of the Little Ice Age (LIA) and Medieval Climate Anomaly (MCA) are indicated as blue and yellow shading respectively. The regression line of GeoB8323-2 (not shown) has an equation of $y = -0.00106x + 15.1990$, corresponding to a gradient of -0.1 °C per 100 years.

3.2 Grain size

Figure 5a shows the resulting ratios of the 3 end-member model, with Figure 5b displaying the eigenvalues and their corresponding end-member number. Grain size analysis of core GeoB8323-2 reveals a unimodal distribution in the particle size distributions (Figure 5c). The three members (referred to as EM1, EM2 and EM3) have modal sizes of 19μm, 12μm and 8μm respectively. Fine-grained sediment (EM3) contributes to the majority of

deposition prior to 800 CE, consisting of more than 43% at any given time. A particularly stable period with little change in proportions occurred from about 250 – 800 CE, during which the largest percentage of the material is EM3. The coarse fraction, EM1, is only present in very small volume prior to 800 CE, and not at all from ca. 400 to 800 CE.

At 800 CE a rapid shift to coarser material (EM1) occurred, perpetuating a series of peaks and minima between the coarse and fine fractions over the subsequent 800 years (Figure 5a). Interestingly, the beginning of this rapid shift coincides with the doubling of the deposition rate (which lasts for roughly 100 years). A second large increase in the coarse end-member occurred at 1600 CE, after which EM1 becomes the main fraction of the sediment, reaching up to 78%. This second shift is more marked than the first, with coarse grain size becoming increasingly dominant during the 200 years that follow. During this time, the portion of medium-sized grains decreases until it reaches zero at around 1850 CE. Figure 5a shows that a maximum in coarse grain size (EM1) is centred around 1800 CE, after which a decrease in EM1 and an increase in EM3, are observed.

3.2 Fe/K Elemental ratio

The lowest values for the Fe/K ratio are found prior to 600 CE, a period in which Fe/K is relatively stable (Figure 6a). After this, the ratio increases until about 1250 CE, at which point an interval of lower values is distinguishable, lasting for roughly 150 years. Fe/K increases again from around 1550 CE. The final 350 years witness the highest values observed in the record, with peak values occurring at around 1900 CE before a sharp drop occurs towards the end of the record at ca. 1900 CE.

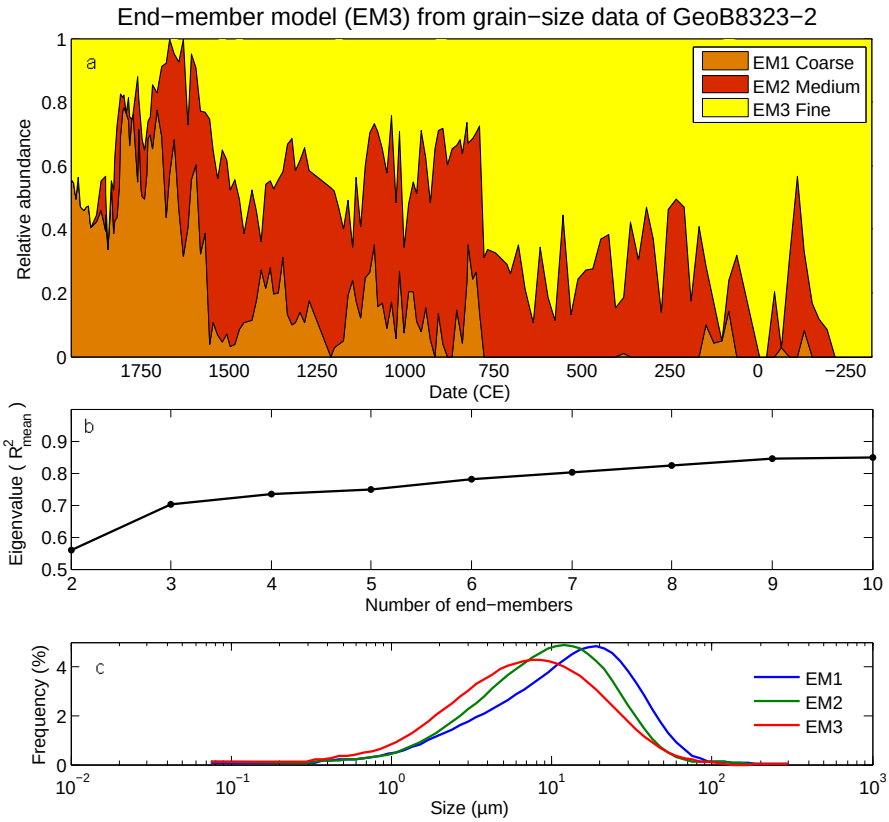

Figure 5: Results from end-member modeling. (a) Ratio proportions of EM1 (coarse) to EM3 (fine); (b) Fraction of variation explained by the amount of end-members; (c) Unimodal curves of grain size classes of the modelled end-members.

4 Discussion

4.1 Sea surface temperature forcing during the late Holocene

Comparison of core-top alkenone-derived SST from GeoB8323-2 with satellite-derived SSTs (Locarini et al. 2013) reveals similar temperatures, with our most recent data point (ca. 1900 CE) reflecting a temperature of 14.4°C. The discrepancy between the

two is within the $U^{K'}_{37}$ SST calibration error of 1°C (Müller et al. 1998). Therefore, reconstructed SST values may be assumed to reflect mean annual values.

4.1.1 Regional forcing factors

Our results indicate that low SSTs in St. Helena Bay occurred during the last several hundred years. During this period, relationships between local environmental variation at other Southern Hemispheric sites (marine, terrestrial and lacustrine) and large-scale forcings (sea ice and westerly winds) have previously been observed (Lamy et al. 2001, 2002; Stager et al. 2012; Chase & Meadows 2007). This elicited a comparison between the new Southern BUS SST data and the aforementioned drivers. Low SSTs coincided with the expansion of sea-ice and low latitude westerly winds (Etourneau et al. 2013; Lamy et al. 2001; Lamy et al. 2002). It is therefore necessary to look at regional forcing mechanisms - both oceanic and atmospheric - as well as large-scale processes.

The SST signal from GeoB8323-2 provides a unique record of oceanic changes during the late Holocene in southwest Africa. The millennial-scale cooling trend observed in Figure 6b is likely indicative of larger-scale atmospheric forcing mechanisms (similarly proposed by Lamy et al. 2001), while the shorter semi-centennial time-scale fluctuations are possibly a result of more regional oceanic variation (Jury & Courtney 1994; Dufois & Rouault 2012). In the modern southwest African region, large-scale seasonal changes, such as the variations in the extent of sea-ice around Antarctica, have been shown to have significant effects on climate (Sokolov & Rintoul 2007). For example, shifts in Antarctic sea-ice are a result of responses to seasonal changes in insolation, which leads to expansion during winter and contraction during summer (Moros et al. 2009; Blome et al. 2012). Cool winter conditions cause the oceanic fronts to migrate north, and create strong SST gradients that intensify the austral westerly winds and displace them northward (Renssen et al. 2005; Sokolov & Rintoul 2007). The westerly winds follow the seasonal latitudinal migration of the fronts. During cool periods with extensive sea-ice, the intensified onshore westerly winds bring more moisture to southwestern Africa and

suppress upwelling (Bard & Rickaby 2009). In contrast, southerly displaced fronts lead to a southward displacement of the South Atlantic anticyclone causing alongshore winds, increased upwelling, and lowered SST.

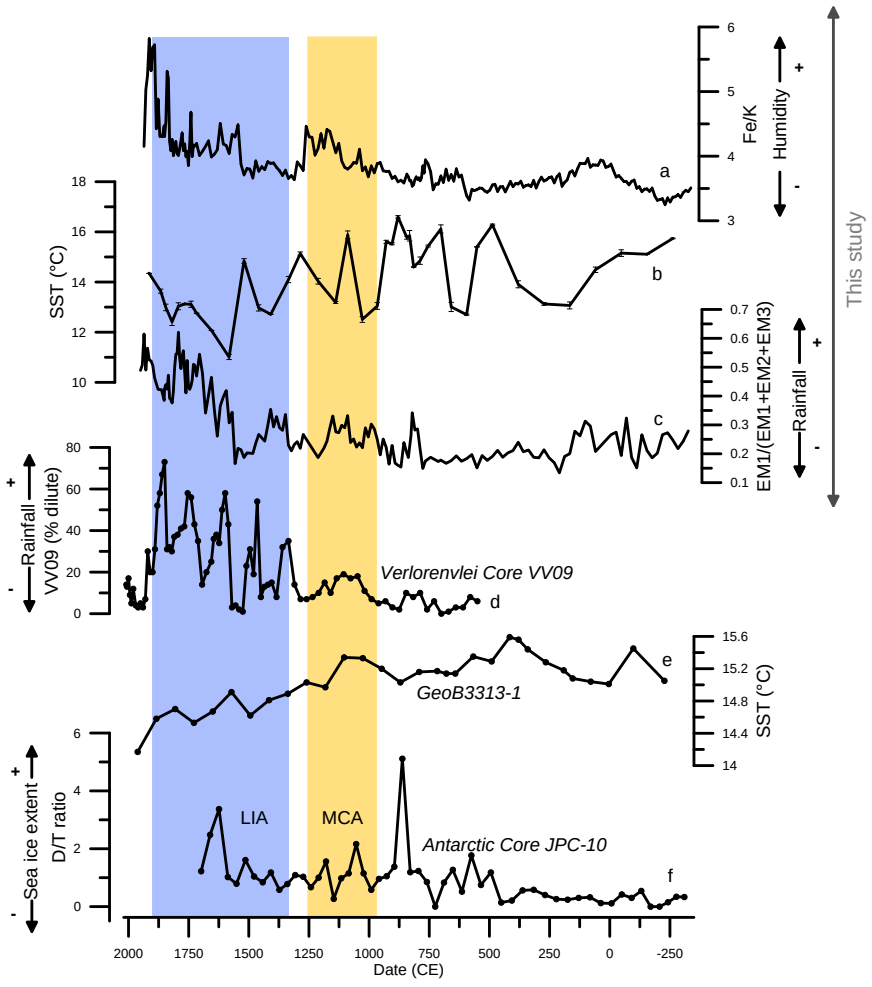

Figure 6: (a) GeoB8323-2 Fe/K ratio as a proxy for chemical weathering. (b) GeoB8323-2 Benguela Current SST in St. Helena Bay. (c) Ratio changes in GeoB8323-2 coarse grain size (1EM3) to fine and medium grain size. (d) Diatom concentration from Stager et al. (2012) showing the percentage of dilute-water diatoms, indicating freshwater input into Lake Verlorenvlei and serving as a proxy for precipitation in the lake catchment. (e) GeoB3313-1 Peru Current SSTs (Lamy et al. 2002). (f) Diene/Triene ratio from Antarctic core, from Etourneau et al. (2013), representing variation in Antarctic sea-ice extent.

This concept of upwelling-driven SST changes, however, is inconsistent with our data. The data show that changes in local south-easterly winds - responsible for driving coastal upwelling - were not significant for the majority of the record. This is demonstrated by the fact that SST in the greater region of St. Helena Bay appears to have no identifiable link to SST variation at locations further north in the Benguela system (Figure 4) (Farmer et al. 2005; Leduc et al. 2010). Therefore, we conclude that Holocene SST changes in this region were not primarily controlled by upwelling, but by other processes.

4.1.2 Controls on the southern Benguela Current

Our data fit with the hypothesis that processes involved in the long-term decrease in SST are rooted in the progressively northward migration of the austral westerly winds, which have acted to decrease the ocean temperature (Lamy et al. 2001; Weldeab et al. 2013). This occurred via one or both of two possible mechanisms: firstly, through a decrease in Benguela Current source water temperature and/or the movement of colder surface waters into the BUS from the South Atlantic gyre due to the expansion of sea-ice (Farmer et al. 2005), and secondly, through the pinching off of Agulhas through-flow, which would reduce warm water transport from the Agulhas Current westwards into the BUS (Bard & Rickaby 2009).

Further north in the Benguela Current, the mid-latitude westerlies and Agulhas leakage are geographically too far away to significantly impact the upwelling system, whose SSTs are primarily driven by changes in south-easterly winds (Nelson & Hutchings 1983), but at 32°S, where GeoB8323-2 is located, these two factors appear to be more influential. The latitudinal position, combined with the variable coastal topography of the region, produces a climatic and oceanic signal distinctive from the remainder of the BUS. The SST range (~5.6°C) for GeoB8323-2 is also larger than those recorded in the northern BUS (Leduc et al. 2010, Farmer et al. 2005), and is suggestive of a dynamic micro-system at this location, which results in an amplified signal.

Despite the fact that large-scale atmospheric forcing dominated SST variation for

much of the record, upwelling-inducing south-easterly winds seem to have impacted the signal from 250 BCE until about 250 CE, leading to a decline in SST. During this time there is no evidence for an increase in sea-ice (Etourneau et al. 2013), or a wetter WRZ (Stager et al. 2012) either of which might indicate a northward migration of the wind belt; instead, similarly decreasing SSTs are observed for locations further north in the Benguela during this time (Farmer et al. 2005; Leduc et al. 2010). Therefore, it would appear that local scale forcing became important in St Helena Bay when the westerly wind belt was far south and less proximal to the Agulhas and the Benguela systems. The remainder of the record documents a progressively northward movement of the wind belt, with the most northerly position occurring between 1600 and 1900 CE, a period roughly synchronous with the LIA.

4.2 Late Holocene terrestrial changes in hydrology

4.2.1 Source of material

Sharp changes in grain size distributions (Figure 5a) are most apparent for the coarse grain size end-member, EM1. Shifts towards a greater proportion of the coarse end-member occurred at 800 and 1600 CE. The elemental record compares well with the EM variations, with sharp changes occurring at similar times. The Fe/K ratio indicates an increase in chemical weathering associated with higher humidity as the fluvial transport increases (Govin et al. 2012). In effect, wetter conditions induce more chemical weathering, due to the increased moisture in the environment. Fe/K in this case supports our interpretation of changes in fluvial transport, due to Fe's ability to be retained in soil even under high degrees of chemical weathering (Govin et al. 2012). With regards to grain size, although traditionally coarse end-members have in the past been seen as representative of wind-derived sediment, dust particles here are an unlikely source of material, since studies have documented that there is little wind-transported material from southwest South Africa deposited in the Atlantic (Prospero et al. 2002; Eckardt et al. 2013; Vickery et al. 2013; Hahn et al. 2015).

Material transported to the location of GeoB8323-2 from the catchment region of the Orange River would only be present as fine-grained deposits. Coarse sediment from the Orange River reaching the coast cannot be transported southwards, due to the strength of the poleward undercurrent being sufficient only to keep fine mud in suspension (Shannon & Nelson 1996). The Orange River therefore cannot be the source of the increasing proportion of coarse grain size (EM1) exhibited in Figure 6c. Coarse material is thus most likely derived from the local Olifants catchment and deposited on the shelf through local river runoff.

Shifts in grain size are interpreted as changing local terrestrial hydrology, i.e., higher rainfall in the WRZ as EM1 increases. By itself, this proxy is not definitive as an indicator of precipitation, and changing EM ratios have also been documented as being affected by variation in bottom current strength and sea-level (Rogers & Rau 2006). Sea-level variations during the past 2,250 years, however, have an amplitude of $\pm$ 1 m (Compton 2001), are unlikely to have affected the record. In addition, several other proxy methods used here have in the past been demonstrated to be reliable indicators of moisture availability (Lamy et al. 2001; Weldeab et al. 2013; Hahn et al. 2015). Coupled to SST and XRF data, and taking previous research of the region into account, the timing of the shifts in the EM record provide a strong argument for its use as a proxy for hydrological variation in this location, an interpretation supported by Hahn et al. (2015) in their analysis of the WRZ. A long-term increase in Olifants River discharge due to wetter conditions is most likely the underlying cause for the observed changes in the EM and elemental ratios.

4.2.2 Climatic interpretation

Our results suggest that increasingly wet conditions at the study site, as shown in the increasing grain size and higher Fe/K ratios, coincided with decreasing SST. This trend indicates a movement towards a more northerly position of the westerly wind belt, which progressively caused lower SSTs and increased rainfall in southwestern Africa over much of the late Holocene. This model fits with those previously describing the WRZ (Stager

et al. 2012; Weldeab et al. 2012). Fluctuations in Fe/K and EM1 (coarse grain size) (Figures 6a and c) both register that from 250 BCE until about 750 CE, climate in the WRZ was stable and drier than the more recent Holocene with driest conditions occurring between 250 and 0 BCE. A dry WRZ during this time coincides with the findings of Carr et al. (2015), who document a relatively arid period from 550 BCE to 1000 CE. After this period, the wind belt started to shift to a more northerly position, and humidity and rainfall in the WRZ increased markedly within half a century. The grain size and elemental records, through the introduction of coarse fluvial material from the Olifants River, show that the period from 800 to 1600 CE was wetter but highly variable, fluctuating between wet and dry conditions. The doubling of the sedimentation rate at 800 CE could be a direct result of increasing transport from the Olifants due to intense precipitation. This high degree of variability is also seen in the SST record (Figure 6b); the late Holocene climate phase known as the MCA falls into this time of high variability (Mann et al. 2009).

A distinct shift towards more consistently wetter conditions occurred at about 1600 CE, forced by the northward migration of the westerly winds. The time of this sharp change is contemporaneous with an intensely cool spell within the LIA (McGregor et al. 2007; Tyson & Preston-Whyte 2000). These conditions lasted for the next 350 years. The Fe/K ratio reflects a sharp increase in humidity at the same time, and this increase in moisture availability in the WRZ during the last several hundred years is in accordance with several studies which have documented a rapid late Holocene shift towards wetter conditions in the WRZ (Chase & Meadows 2007; Stager et al. 2012; Carr et al. 2015), although GeoB8323-2 proxy records show this to have occurred roughly 200 years after the changes documented in the aforementioned studies. This discrepancy is most likely a result of differences in calibration of age models between terrestrial and marine archives, as there will be uncertainties in all stratigraphic core dating.

A noticeable decrease in WRZ rainfall is apparent from about 1800 to 1900 CE, as shown by the end-member analysis of grain size, while SST increases occurred from

about 1700 to 1900 CE, reaching modern-day Benguela Current temperatures at around 1850 CE. Studies from Verlorenvlei have also previously documented an intensification in aridity after wet conditions peaked at around 1850 CE (Figure 6d) (Stager et al. 2012; Carr et al. 2015). This most recent variation is interpreted here as a southwards shift in the austral westerly winds at the end of the LIA (1850 CE), a view supported by the aforementioned studies. This would allow for increased Agulhas leakage and a decrease in rainfall over land. However, caution is advised when interpreting the most recent 300 years, as account must be made for anthropogenic influence, as humans occupying southwest Africa began to significantly affect their environment from around this time (Stager et al. 2012; Hahn et al. 2015).

4.3 Intra- and inter-hemispheric linkages

The significant influence exerted by the austral westerlies on the St Helena Bay region makes it relevant for larger-scale studies. The long-term decrease in GeoB8323-2 SST is coeval with SST trends in two marine cores off the west coast of South America located between 30 and 40°S in the Peru Current (Kaiser et al. 2008; Lamy et al. 2002). The close relationship between oceanic and terrestrial climate changes in the realm of the westerly wind belt has been studied extensively in South America (Lamy et al. 1999, 2001, 2002, 2004, 2010). These studies link the increasing influence of westerly winds to an increase in moisture availability along the South American southwest coast (Lamy et al. 1999, 2001). The SST record of GeoB3313-1 (Figure 6e) in particular complements the SST record of GeoB8323-2 (Figure 6b), as does the Antarctic D/T ratio (Figure 6f) to a lesser extent. This supports the concept of large-scale intra-hemispheric changes significantly affecting Southern Hemisphere upwelling systems during the late Holocene.

Records from Australia and New Zealand have also been suggestive of close ties between westerlies and precipitation, although the last 4,000 years have indicated a departure from the zonal symmetry seen today (Fletcher & Moreno 2012). Climate changes in this region have therefore not fully mirrored those seen in Southern Africa or South

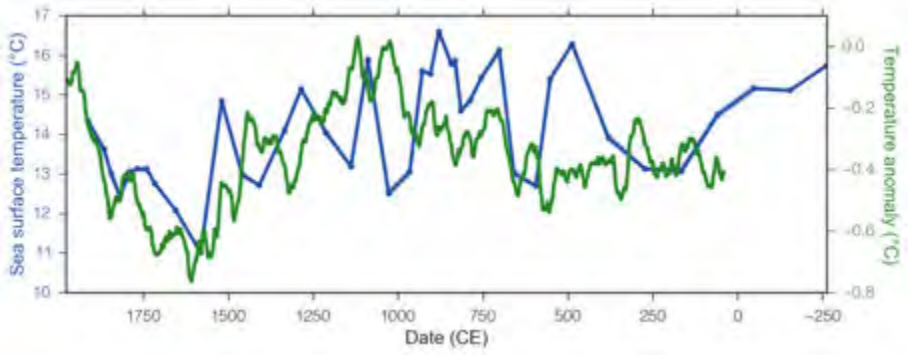

Figure 7: Comparison between Benguela Current SST (blue) and Northern Hemisphere mean annual temperature anomaly (green), from Moberg et al. (2005). The Moberg et al. (2005) dataset is a combination of several low-resolution proxy records with high-resolution tree-ring series. A running mean of 40 years is applied.

America, and are likely the result of dominance of other climate forcing mechanisms in this region (Fletcher & Moreno 2012). However, a record from the Murray Darling Basin, a semi-arid region in eastern Australia, has recognized a trend towards more variable, wetter conditions during the last 1,000 years, particularly around 1250 CE (Marx et al. 2011). This record indicates that, at least for this period, there was some Southern Hemisphere climate symmetry, reflecting austral westerly wind variation. The synchronous changes experienced by Southern Hemispheric continents are evidence of hemispheric-scale climate forcing significantly affecting local regions within the Southern Hemisphere.

To reveal inter-hemispheric connections the GeoB8323-2 SST record is compared to the high-resolution temperature reconstruction for the Northern Hemisphere by Moberg et al. (2005). Both records reveal a positive correlation (Figure 7) with decreasing trends during the last 1,000 years, minimum temperatures at around 1550 CE, followed by an increase towards the present. The observed positive correlation between northern Hemisphere temperatures and the SST record in St. Helena Bay suggests that the underlying process for this co-variation is different than the mechanism observed during the last Glacial and deglaciation, i.e. the asynchrony exhibited through Antarctic warming during a time of Arctic cooling, transmitted by changes in the Atlantic overturning circulation (Barbante et al. 2006; Barker et al. 2009). Potential forcing factors are thus global solar insolation

changes, variations in atmospheric aerosol content and/or other anthropogenic causes.

5 Conclusions

In this study, we present the first SST record for the St Helena Bay region in the southernmost Benguela Current for the last 2,250 years from a marine sediment record, and discuss the linkages between oceanic and terrestrial climate changes in the WRZ during the Late Holocene. Our findings reveal a long-term cooling trend, with high variability apparent at short, i.e. centennial, time scales. Results suggest that SST changes during the last 2,250 years in this area were not primarily driven by upwelling changes, but by a larger-scale forcing of latitudinal migrations in the austral westerly wind belt. Northerly-positioned westerly winds, such as were present during the LIA, acted to decrease Agulhas warm-water leakage, while re-directing cooler Antarctic waters into the Benguela Current. When westerly winds were located further to the south, large-scale atmospheric features became less important, and local SST was chiefly governed by local winds which drove upwelling variations. In conjunction, these processes led to an amplified SST signal for this region with a larger range as compared to other locations in the Benguela system.

The terrestrial records from this core indicate a long-term increase in precipitation and humidity in the WRZ overlain by rapid shifts (within a few decades), rather than gradual changes. Prior to 800 CE, arid conditions prevailed, whereas recent times have experienced wet conditions. The substantial increase in moisture observed at around 1600 CE (corresponding to the LIA), supports the results of several previous studies. Rainfall is concluded to be largely driven by migration of the westerly wind belts, with a more northerly position leading to higher rainfall in the WRZ.

Despite the lack of correlation between SST evolution in the southernmost Benguela system and that of existing records in more northerly Benguela locations, similarities were observed between southern Benguela and Peru Current SSTs, and a tentative link to Northern Hemisphere air temperatures was recognized. Such intra- and inter-hemispheric linkages mark this region as sensitive to large-scale atmospheric changes.

Acknowledgments:

The authors acknowledge the support of the Regional Archives for Integrated iNvestigations (RAiN) project, with special thanks to Xueqin Zhao, Luke Gregor and John Compton for their contributions. Samples were collected through the aid of the captain and crew of the RV *Meteor* M57/1 cruise, and were prepared with assistance from Ralph Kreutz at MARUM. This research was made possible through funds obtained from the National Research Foundation (NRF) and the Deutsche Akademie Austauschdienst (DAAD).

References

1. Barbante, C., Barnola, J.-M., Becagli, S., Beer, J., Bigler, M., Wolff, E., et al., 2006. One-to-one coupling of glacial climate variability in Greenland and Antarctica. Nature, 444, pp.195–198. Available at: http://www.nature.com/doifinder/10.1038/nature05301.

2. Bard, E. & Rickaby, R.E.M., 2009. Migration of the subtropical front as a modulator of glacial climate. Nature, 460, pp.380–383. Available at: http://dx.doi.org/10.1038/nature08189.

3. Barker, S., Diz, P., Vautravers, M.J., Pike, J., Knorr, G., Hall, I.R. & Broecker, W.S., 2009. Interhemispheric Atlantic seesaw response during the last deglaciation. Nature, 457, pp.1097–1102. Available at: http://www.nature.com/doifinder/10.1038/nature07770.

4. Bloemsma, M.R., Zabel, M., Stuut, J.-B.W., Tjallingii, R., Collins, J. A. & Weltje, G.J., 2012. Modelling the joint variability of grain size and chemical composition in sediments. Sedimentary Geology, 280, pp.135–148. Available at: http://dx.doi.org/10.1016/j.sedgeo.2012.04.009.

5. Blome, M.W., Cohen, A.S., Tryon, C.A., Brooks, A.S. & Russell, J., 2012. The environmental context for the origins of modern human diversity: A synthesis of regional variability in African climate 150,000-30,000 years ago. Journal of Human Evolution, 62, pp.563–592. Available at: http://dx.doi.org/10.1016/j.jhevol.2012.01.011.

6. Carr, A.S., Boom, A., Chase, B.M., Meadows, M.E. & Grimes, H.L., 2015. Holocene sea level and environmental change on the west coast of South Africa: evidence from plant biomarkers, stable isotopes and pollen. Journal of Paleolimnology, 53, pp.415–432.

7. Carr, A.S., Thomas, D.S.G., Bateman, M.D., Meadows, M.E. & Chase, B.M., 2006. Late Quaternary palaeoenvironments of the winter-rainfall zone of southern Africa:

Palynological and sedimentological evidence from the Agulhas Plain. Palaeogeography, Palaeoclimatology, Palaeoecology, 239, pp.147–165.

8. Chase, B.M., Boom, A., Carr, A.S., Meadows, M.E. & Reimer, P.J., 2013. Holocene climate change in southernmost South Africa: rock hyrax middens record shifts in the southern westerlies. Quaternary Science Reviews, 82, pp.199–205.

9. Chase, B.M. & Meadows, M.E., 2007. Late Quaternary dynamics of southern Africa's winter rainfall zone. Earth-Science Reviews, 84, pp.103–138.

10. Chase, B.M., Meadows, M.E., Scott, L., Thomas, D.S.G., Marais, E., Sealy, J. & Reimer, P.J., 2009. A record of rapid Holocene climate change preserved in hyrax middens from southwestern Africa. Geology, 37, pp.703–706. Available at: http://geology.gsapubs.org/cgi/doi/10.1130/G30053A.1.

11. Compton, J., 2001. Holocene sea-level fluctuations inferred from the evolution of depositional environments of the southern Langebaan Lagoon salt marsh, South Africa. The Holocene, 11, pp.395–405. Available at: http://hol.sagepub.com/cgi/doi/10.1191/095968301678302832.

12. Cowling, R.M., Cartwright, C.R., Parkington, J.E. & Allsopp, J.C., 1999. Fossil wood charcoal assemblages from Elands Bay Cave, South Africa: implications for Late Quaternary vegetation and climates in the winter-rainfall fynbos biome. Journal of Biogeography, 26, pp.367–378. Available at: http://doi.wiley.com/10.1046/j.1365-2699.1999.00275.x.

13. Demarcq, H., Barlow, R.G. & Shillington, F.A., 2003. Climatology and Variability of Sea Surface Temperature and Surface Chlorophyll in the Benguela and Agulhas Ecosystems As Observed by Satellite Imagery. African Journal of Marine Science, 25, pp.363–372. Available at: http://www.tandfonline.com/doi/abs/10.2989/18142320309504022.

14. Desmet, P.G. & Cowling, R.M., 1999. Biodiversity, habitat and range-size aspects of a flora from a winter-rainfall desert in north-western Namaqualand, South Africa. Plant Ecology, 142, pp.23–33. Available at: http://dx.doi.org/10.1023/A:1009814109891.

15. Dewar, G., Reimer, P.J., Sealy, J. & Woodborne, S., 2012. Late-Holocene marine radiocarbon reservoir correction (ΔR) for the west coast of South Africa. The Holocene, 22, pp.1481–1489. Available at: http://hol.sagepub.com/cgi/doi/10.1177/0959683612449755.

16. Dufois, F. & Rouault, M. 2012. Sea surface temperature in False Bay (South Africa): Towards a better understanding of its seasonal and inter-annual variability. Continental Shelf Research. 43, pp. 24-35.

17. Eckardt, F.D. & Kuring, N., 2005. SeaWiFS identifies dust sources in the Namib Desert. International Journal of Remote Sensing, 26, pp.4159–4167.

18. Eckardt, F.D., Livingstone, I., Seely, M. & Von Holdt, J., 2013. The surface geology and geomorphology around Gobabeb, Namib desert, Namibia. Geografiska Annaler, Series A: Physical Geography, 95, pp.271–284.

19. Etourneau, J., Collins, L.G., Willmott, V., Kim, J.H., Barbara, L., Leventer, A., Schouten, S., Sinninghe Damsté, J.., Bianchini, A., Klein, V., Crosta, X. & Massé, G., 2013. Holocene climate variations in the western Antarctic Peninsula: Evidence for sea ice extent predominantly controlled by changes in insolation and ENSO variability. Climate of the Past, 9, pp.1431–1446.

20. Fletcher, M.-S. & Moreno, P.I., 2012. Have the Southern Westerlies changed in a zonally symmetric manner over the last 14,000 years? A hemisphere-wide take on a controversial problem. Quaternary International, 253, pp.32–46.

21. Farmer, E.C., deMenocal, P.B. & Marchitto, T.M., 2005. Holocene and deglacial ocean temperature variability in the Benguela upwelling region: Implications for

low-latitude atmospheric circulation. Paleoceanography, 20, pp.1–16.

22. Garzanti, E., Vermeesch, P., Andò, S., Lustrino, M., Padoan, M. & Vezzoli, G., 2014. Ultra-long distance littoral transport of Orange sand and provenance of the Skeleton Coast Erg (Namibia). Marine Geology, 357, pp.25–36.

23. Garzoli, S.L., Richardson, P.L., Rae, C.M.D., Fratantoni, D.M., Gofii, G.J. & Roubicek, A.J., 1999. Three Agulhas Rings observed during the Benguela Current Experiment. Journal of Geophysical Research, 104, pp.20971–20985.

24. Gingele, F.X., 1996. Holocene climatic optimum in southwest Africa - Evidence from the marine clay mineral record. Palaeogeography Palaeoclimatology Palaeoecology, 122, pp.77–87.

25. Govin, A., Holzwarth, U., Heslop, D., Ford Keeling, L., Zabel, M., Mulitza, S., Collins, J.A. & Chiessi, C.M., 2012. Distribution of major elements in Atlantic surface sediments (36°N-49°S): Imprint of terrigenous input and continental weathering. Geochemistry, Geophysics, Geosystems, 13, pp.1–23.

26. Hahn, A., Compton, J., Meyer-Jacob, C., Kirsten, K., Lucassen, F., Mayo, M., Schefuß, E. & Zabel, M., Holocene paleoclimatic record from the South African Namaqualand mudbelt: A source to sink approach. Quaternary International, 2015, pp.1–15.

27. Hardman-Mountford, N.J., Richardson, A.J., Agenbag, J.J., Hagen, E., Nykjaer, L., Shillington, F.A. & Villacastin, C., 2003. Ocean climate of the South East Atlantic observed from satellite data and wind models. Progress in Oceanography, 59, pp.181–221.

28. Herbert, C.T. & Compton, J., 2007. Geochronology of Holocene sediments on the western margin of South Africa. South African Journal of Geology, 110, pp.327–338. Available at: http://sajg.geoscienceworld.org/cgi/doi/10.2113/gssajg.110.2-3.327.

29. Hutchings, L., van der Lingen, C.D., Shannon, L.J., Crawford, R.J.M., Verheye, H.M.S., Bartholomae, C.H., van der Plas, A.K., Louw, D., Kreiner, A., Ostrowski, M., Fidel, Q., Barlow, R.G., Lamont, T., Coetzee, J., Shillington, F.A., Veitch, J.A., Currie, J.C. & Monteiro, P.M.S., 2009. The Benguela Current: An ecosystem of four components. Progress in Oceanography, 83, pp.15–32. Available at: http://dx.doi.org/10.1016/j.pocean.2009.07.046.

30. Jansen, J.H.., Van Der Gaast, S.J., Koster, B. & Vaars, A.J., 1998. CORTEX, a shipboard XRF-scanner for element analyses in split sediment cores. Marine Geology, 151, pp.143–153.

31. Jury, M & Courtney, S. 1995. Climatic determinants of Benguela SST variability. Continental Shelf Research. 15, pp. 1339-1354.

32. Kaiser, J., Schefuß, E., Lamy, F., Mohtadi, M. & Hebbeln, D., 2008. Glacial to Holocene changes in sea surface temperature and coastal vegetation in north central Chile: high versus low latitude forcing. Quaternary Science Reviews, 27, pp.2064–2075.

33. Kido, Y., Koshikawa, T. & Tada, R., 2006. Rapid and quantitative major element analysis method for wet fine-grained sediments using an XRF microscanner. Marine Geology, 229, pp.209–225.

34. Lamont, T., Hutchings, L., van den Berg, M., Goschen, W.S. & Barlow, R.G., 2015. Hydrographic variability in the St. Helena Bay region of the southern Benguela ecosystem. Journal of Geophysical Research: Oceans.

35. Lamy, F., Hebbeln, D., Röhl, U. & Wefer, G., 2001. Holocene rainfall variability in southern Chile: a marine record of latitudinal shifts of the Southern Westerlies. Earth and Planetary Science Letters, 185, pp.369–382.

36. Lamy, F., Hebbeln, D. & Wefer, G., 1999. High-resolution marine record of climatic

change in mid-latitude Chile during the last 28,000 years based on terrigenous sediment parameters. Quaternary Research, 51, pp.83–93.

37. Lamy, F., Kaiser, J., Ninnemann, U., Hebbeln, D., Arz, H.W. & Stoner, J., 2004. Antarctic timing of surface water changes off Chile and Patagonian ice sheet response. Science, 304, pp.1959–1962.

38. Lamy, F., Kilian, R., Arz, H.W., Francois, J.-P., Kaiser, J., Prange, M. & Steinke, T., 2010. Holocene changes in the position and intensity of the southern westerly wind belt. Nature Geoscience, 3, pp.695–699. Available at: http://dx.doi.org/10.1038/ngeo959.

39. Lamy, F., Rühlemann, C., Hebbeln, D. & Wefer, G., 2002. High- and low-latitude climate control on the position of the southern Peru-Chile Current during the Holocene. Paleoceanography, 17, pp.16–1 – 16–10.

40. Leduc, G., Herbert, C.T., Blanz, T., Martinez, P. & Schneider, R., 2010. Contrasting evolution of sea surface temperature in the Benguela upwelling system under natural and anthropogenic climate forcings. Geophysical Research Letters, 37, pp.1–5. Available at: http://doi.wiley.com/10.1029/2010GL044353.

41. Locarini, R.A., Mishonov, A. V., Antonov, J.I., Boyer, T.P., Garcia, H.E., Baranova, O.K., Zweng, M.M., Paver, C.R., Reagan, J.R., Johnson, D.R., Hamilton, M. & Seidov, D., 2013. World Ocean Atlas 2013, Volume 1: Temperature S. Levitus & A. Mishanov, eds., NOAA Atlas NESDIS 73.

42. Marx, S.K., Kamber, B.S., McGowan, H.A. & Denholm, J., 2011. Holocene dust deposition rates in Australia's Murray-Darling Basin record the interplay between aridity and the position of the mid-latitude westerlies. Quaternary Science Reviews, 30, pp.3290–3305.

43. Mann, M., Zhang, Z., Rutherford, S., Bradley, R., Hughed, M., Shindell, D., Ammann, C., Faluvegi, G. & Ni, F., 2009. Global Signatures and Dynamical Origins

of the Little Ice Age and Medieval Climate Anomaly. Science, 326, pp.1256–1260.

44. McGregor, H. V, Dima, M., Fischer, H.W. & Mulitza, S., 2007. Rapid 20th-century increase in coastal upwelling off northwest Africa. Science, 315, pp.637–9.

45. Meadows, M.E. & Baxter, A.J., 2001. Holocene vegetation history and palaeoenvironments at Klaarfontein Springs, Western Cape, South Africa. The Holocene, 11, pp.699–706. Available at: http://hol.sagepub.com/cgi/doi/10.1191/09596830195726.

46. Meadows, M.E., Baxter, A.J. & Parkington, J., 1996. Late Holocene environments at Verlorenvlei, Western Cape Province, South Africa. Quaternary International, 33, pp.81–95.

47. Meadows, M.E., Chase, B.M. & Seliane, M., 2010. Holocene palaeoenvironments of the Cederberg and Swartruggens mountains, Western Cape, South Africa: Pollen and stable isotope evidence from hyrax dung middens. Journal of Arid Environments, 74, pp.786–793. Available at: http://dx.doi.org/10.1016/j.jaridenv.2009.04.020.

48. Meadows, M.E., Rogers, J., Lee-Thorp, J. A., Bateman, M.D. & Dingle, R. V., 2002. Holocene geochronology of a continental-shelf mudbelt off southwestern Africa. The Holocene, 12, pp.59–67.

49. Moberg, A., Sonechkin, D., Holmgren, K., Datsenko, N. & Karlén, W., 2005. Highly variable Northern Hemisphere temperatures reconstructed from low- and high-resolution proxy data. Letters to Nature, 433, pp.613–617.

50. Moros, M., De Deckker, P., Jansen, E., Perner, K. & Telford, R.J., 2009. Holocene climate variability in the Southern Ocean recorded in a deep-sea sediment core off South Australia. Quaternary Science Reviews, 28, pp.1932–1940. Available at: http://dx.doi.org/10.1016/j.quascirev.2009.04.007.

51. Müller, P.J., Kirst, G., Ruhland, G., Storch, I. Von & Rosell-Mele, A., 1998. Calibration of the alkenone paleotemperature index U K 37 based on core-tops from

the eastern South Atlantic and the global ocean (60°N-60°S). Geochemica et Cosmochimica Acta, 62 pp.1757–1772.

52. Nelson, G. & Hutchings, L., 1983. The Benguela upwelling area. Progress in Oceanography, 12, pp.333–356.

53. Pitcher, G.C., Figueiras, F.G., Hickeyd, B.M. & Moita, M.T., 2010. The physical oceanography of upwelling systems and the development of harmful algal blooms. Progress in Oceanography, 85, pp.5–32.

54. Pitcher, G.C. & Nelson, G., 2006. Characteristics of the surface boundary layer important to the development of red tide on the southern Namaqua shelf of the Benguela upwelling system. Limnology and Oceanography, 51, pp.2660–2674.

55. Prahl, F.G. & Wakeham, S.G., 1987. Calibration of unsaturation patterns in long-chain ketone compositions for palaeotemperature assessment. Nature, 330, pp.367–369.

56. Prospero, J.M., Ginoux, P., Torres, O., Nicholson, S.E.E. & Gill, T.E., 2002. Environmental characterization of global sources of atmospheric soil dust identified with the NIMBUS 7 Total Ozone Mapping Spectrometer (TOMS) absorbing aerosol product. Reviews of Geophysics, 40, pp.1–31.

57. Quick, L., Chase, B.M., Meadows, M.E., Scott, L. & Reimer, P.J., 2011. A 19.5kyr vegetation history from the central Cederberg Mountains, South Africa: Palynological evidence from rock hyrax middens. Palaeogeography, Palaeoclimatology, Palaeoecology, 309, pp.253–270. Available at: http://dx.doi.org/10.1016/j.palaeo.2011.06.008.

58. Reimer, P.J., 2013. IntCal13 and Marine13 Radiocarbon Age Calibration Curves 0–50,000 Years cal BP. Radiocarbon, 55, pp.1869–1887.

59. Renssen, H., Goosse, H., Fichefet, T., Masson-Delmotte, V. & Koç, N., 2005. Holocene climate evolution in the high-latitude Southern Hemisphere simulated by a

coupled atmosphere–sea ice–ocean–vegetation model. The Holocene, 15, pp.951–964.

60. Rogers, J. & Rau, A., 2006. Surficial sediments of the wave-dominated Orange River Delta and the adjacent continental margin off south-western Africa. African Journal of Marine Science, 28, pp.511–524.

61. Rommerskirchen, F., Eglinton, G., Dupont, L., Güntner, U., Wenzel, C. & Rullkötter, J., 2003. A north to south transect of Holocene southeast Atlantic continental margin sediments: Relationship between aerosol transport and compound-specific δ13C land plant biomarker and pollen records. Geochemistry, Geophysics, Geosystems, 4, pp.1–29. Available at: http://doi.wiley.com/10.1029/2003GC000541.

62. Rouault, M., Pohl, B. & Penven, P., 2010. Coastal oceanic climate change and variability from 1982 to 2009 around South Africa. African Journal of Marine Science, 32, pp.237–246.

63. de Ruijter, W.P.M., Biastoch, A., Drijfhout, S.S., Lutjeharms, J.R.E., Matano, R.P., Pichevin, T., van Leeuwen, P.J. & Weijer, W., 1999. Indian-Atlantic interocean exchange: Dynamics, estimation and impact. Journal of Geophysical Research, 104, pp.20885–20910.

64. Schouten, M., Ruijter, W., van Leeuwen, P.J. & Lutjeharms, J.R.E., 2000. Translation , decay and splitting of Agulhas rings in the southeastern Atlantic Ocean. Journal of Geophysical Research, 105, pp.21913–21925.

65. Shannon, L.V. & Nelson, G., 1996. The Benguela: large scale features and processes and system variability. In G. Wefer et al., eds. The South Atlantica: Present and Past Circulation. Berlin: Springer, pp. 163–210.

66. Shillington, F.A., 1998. The Benguela upwelling system off southwestern Africa. The Sea, 11, pp.583–604.

67. Shindell, D.T. & Schmidt, G.A., 2004. Southern Hemisphere climate response to ozone changes and greenhouse gas increases. Geophysical Research Letters, 31,

pp.1–4.

68. Smith, A.B., Sadr, K., Gribble, J. & Yates, R., 1991. Excavations in the south-western Cape, South Africa, and the archaeological identity of prehistoric hunter-gatherers within the last 2000 years.. The South African Archaeological Bulletin, 46, pp.71–91.

69. Sokolov, S. & Rintoul, S.R., 2007. On the relationship between fronts of the Antarctic Circumpolar Current and surface chlorophyll concentrations in the Southern Ocean. Journal of Geophysical Research: Oceans, 112, pp.1–17.

70. Stager, J.C., Mayewski, P.A., White, J., Chase, B.M., Neumann, F.H., Meadows, M.E., King, C.D. & Dixon, D.A., 2012. Precipitation variability in the winter rainfall zone of South Africa during the last 1400 yr linked to the austral westerlies. Climate of the Past, 8, pp.877–887.

71. Stewart, R.H., 2009. Introduction To Physical Oceanography, Texas A & M University.

72. Stuut, J.-B.W., Crosta, X., van der Borg, K. & Schneider, R., 2004. Relationship between Antarctic sea ice and southwest African climate during the late Quaternary. Geology, 32, pp. 909-912. Available at: http://geology.gsapubs.org/cgi/doi/10.1130/G20709.1.

73. Toggweiler, J.R., Russell, J.L. & Carson, S.R., 2006. Midlatitude westerlies, atmospheric CO2, and climate change during the ice ages. Paleoceanography, 21, pp.1–15.

74. Tyson, P.D., Garstang, M. & Swap, R., 1996. Large-Scale Recirculation of Air over Southern Africa. Journal of Applied Meteorology, 35, pp.2218–2236.

75. Tyson, P.D. & Preston-Whyte, R.A., 2000. The Weather and Climate of Southern Africa Second edi. A. Attwell, ed., South Africa: Oxford University Press.

76. Valsecchi, V., Chase, B.M., Slingsby, J.A., Carr, A.S., Quick, L., Meadows, M.E., Cheddadi, R. & Reimer, P.J., 2013. A high resolution 15,600-year pollen and microcharcoal record from the Cederberg Mountains, South Africa. Palaeogeography, Palaeoclimatology, Palaeoecology, 387, pp.6–16. Available at: http://dx.doi.org/10.1016/j.palaeo.2013.07.009.

77. Vickery, K.J., Eckardt, F.D. & Bryant, R.G., 2013. A sub-basin scale dust plume source frequency inventory for southern Africa, 2005-2008. Geophysical Research Letters, 40, pp.5274–5279.

78. Walker, N.D., 1990. Links Between South African Summer Rainfall and Temperature Variability of the Agulhas and Benguela Current Systems. Journal of Geophysical Research, 95, pp.3297–3319.

79. Weldeab, S., Stuut, J.-B.W., Schneider, R. & Siebel, W., 2013. Holocene climate variability in the winter rainfall zone of South Africa. Climate of the Past, 9, pp.2347–2364.

80. Weltje, G.J., 1997. End-Member Modeling of Compositional Data: Numerical-Statistical Algorithms for Solving the Explicit Mixing Problem. Mathematical Geology, 29, pp.503–549.

Part III

Controls on leaf-wax δ^{13}C and δD in South Africa's Winter Rainfall Zone during the late Holocene

Robyn Granger[a], Michael E. Meadows[a], Enno Schefuß[b]

[a] Department of Environmental and Geographical Science, University of Cape Town, South Africa

[b] MARUM – Center for Marine Environmental Sciences, University of Bremen, Bremen, Germany

Abstract

Compound-specific isotope analysis of plant lipids in sedimentary archives is a useful tool for the reconstruction of past vegetation and hydrological changes, but the specific mechanisms driving leaf-wax isotope variations in the Winter Rainfall Zone (WRZ) of South Africa have thus far not been established. Towards this end, stable carbon (δ^{13}C) and deuterium (δD) isotope compositions of leaf waxes were determined from sediment samples recovered from the southernmost mudbelt off the west coast of South Africa, which receives terrigenous contributions from the WRZ. Results were interpreted within the context of established palaeo-climatic changes from the same sedimentary archive as well as from the broader WRZ. The leaf wax δ^{13}C compositions, indicating mixed contributions by C_3, C_4 and CAM plants, revealed limited vegetation changes over the last 2,000 years, with variability being interpreted as due to changes in moisture availability and water use efficiency of plants. Water use efficiency was also established as a dominant influence on the leaf wax δD compositions in this region, in conjunction with topographic effects related to shifts in rainfall location (continental and altitude effect). Enriched values were inferred as reflecting more coastal and mountainous rainfall. Our results indicate an increase in moisture availability from ca. 1700 CE, as well as a trend towards more coastal rainfall beginning at ca. 1250 CE. This is in agreement with previous findings from the region. Isotope analysis was deemed to be a useful tool in palaeo-climatic reconstruction for the semi-arid WRZ with regards to both spatial and temporal hydrological variability, but the possibility of multiple drivers of variation in this complex setting necessitates additional independent proxies.

Keywords:

Leaf waxes, *n*-Alkanes, Stable carbon isotope, Deuterium, Winter Rainfall Zone, Organic geochemistry.

1 Introduction

Compound-specific carbon (δ^{13}C) and hydrogen (δD) isotope analyses of lipid biomarkers have become increasingly recognized as useful tools in regards to palaeo-environmental reconstruction. The ubiquity of leaf wax-derived *n*-alkanes in both marine and lacustrine sediments facilitates compound-specific ^{12}C/^{13}C and ^{1}H/^{2}H analysis. δ^{13}C has predominantly been employed as a gauge of variation between photosynthetic plant types (C_3, C_4, CAM), whilst δD changes are usually associated with changes in humidity and precipitation intensity (Sachse et al. 2012).

The potential significance of these proxies for palaeo-vegetation and -hydrological interpretations is evident, but the isotopic compositions of both δ^{13}C and δD are influenced by multiple factors, which may vary in relative strength over time and space. These factors - including changes in temperature, amount of precipitation, altitude and continentality of rainfall, plant type, rate of evapotranspiration, and water use efficiency of the plants - may lead to potentially complicating factors in robust interpretations. The difficulty in numerically quantifying these factors, compounded with the lack of available well-suited archives in semi-arid southern Africa, has so far impeded the use of these novel approaches in the Winter Rainfall Zone (WRZ) of South Africa.

This study aims to provide insights into the various potential influences on the molecular-isotopic signals reflected in leaf waxes from sedimentary archives in the Southern African WRZ. This is facilitated by building upon research into the climate dynamics of the region, as presented by Granger et al. (in review), Zhao et al. (2015) and Zhao et al. (in press) through their various analyses of the same archive as well as by comparison to earlier paleo-climatic studies from the WRZ. This study focuses on the following objectives:

1. Identifying the dominant drivers of leaf wax δ^{13}C and δD changes in South Africa's WRZ;

2. Inferring late Holocene changes in southwest African vegetation and hydrology;

3. Discussing the value of stable isotope analysis, and its contribution to palaeoen-

vironmental reconstructions within the context of the specific region of southwest Africa.

1.1 Regional setting

1.1.1 Climate and vegetation

The climate of the WRZ is influenced chiefly by the position of the South Atlantic High Pressure (SAHP) cell, and rainfall comes primarily from moisture-bearing systems within the eastward-moving westerly winds (Tyson & Preston-Whyte 2000). These migrate seasonally, with a low-latitude peak during austral winter. In contrast to this, the remainder of the country, including the Summer Rainfall Zone (SRZ) and Year-round Rainfall Zone (YRZ), generally relies on easterly wind systems that bring summer rainfall (Tyson & Preston-Whyte 2000).

A steep south-north decreasing rainfall gradient exists along the west coast of the country, contributing to the formation of several biomes in southwest Africa (Figures 8a and b). Each biome supports a wide variety of species, which can be classified according to their photosynthetic pathway. C_3 and C_4 plants "fix" molecules with 3 and 4 carbon atoms respectively; as a result, C_4 plants are more successful in warm, arid conditions, whereas C_3 plants thrive in cool, moist environments (Scott and Vogel 2000). CAM plants are further adapted to water-stressed environments via the mechanisms of water conservation and resistance of photorespiration (Mooney 1972). This group, which fixes carbon in a similar way to C_4 plants, is often associated with succulents (Mooney 1972; O'Leary 1988).

The semi-arid Succulent Karoo (SK) covers a large percentage of the WRZ, and within this biome alone, a wide range of mean annual precipitation averages exists, with the northern boundary receiving an annual average three times lower than its southern part. Plant species in the SK have adapted to water stress, resulting in a dominance of succulents with thick, waxy leaf cuticles designed for water retention (Cowling et al. 2004). The arid terrestrial environment, characteristic of this coastal biome, is strongly coupled

to the oceanic conditions in the adjacent Benguela Upwelling System (BUS), a highly productive cool eastern boundary current system (Shi et al. 1998). The WRZ is comprised of a mix of C_3, C_4 and CAM vegetation, with the Fynbos Biome (FB) being dominated exclusively by C_3 plants. The SK predominantly consists of CAM, the Nama Karoo of mostly C_4, and the Namib Desert of CAM and C_4 (Rutherford & Westfall 1994; Rommerskirchen et al. 2003; Cowling et al. 2004).

The offshore mudbelt (described in detail in Herbert & Compton 2007) runs parallel to the west coast of South Africa, within the BUS. Material drained from rivers along the country's west coast (including the Orange and Olifants Rivers, as well as several ephemeral Namaqualand rivers) is deposited on the continental shelf, thereby contributing to the formation of the mudbelt (Herbert & Compton 2007). The Olifants River (Figures 8a and b) originates within the SK, with a tributary also rising in the southern section of the WRZ, within the FB. The Orange River is the West Coast's largest river in terms of annual discharge, draining the Savanna, Nama-Karoo and Desert biomes, and is responsible for the bulk of sediments that comprise the mudbelt (Herbert & Compton 2007). Although several other west coast rivers drain into the mudbelt, these rivers are ephemeral and make only modest contributions to the mudbelt sediments (Herbert & Compton 2007).

The WRZ exhibits a high degree of topographical variability. The Cederberg Mountain Range (the peak of which lies at just over 2000m) runs north-south along the eastern margin of the WRZ, rising sharply from the flat coastal plains. North and south of the Cederberg, mountains continue to run in a meridional direction, forming a long strip of elevated terrain running parallel to the coast (Chapter 2: Figure 1). The headwaters of the Olifants River originate in this mountain range.

1.1.2 Late Holocene palaeoclimate in southwest Africa

Despite the paucity of favourable sites and the temporal hiatuses that often characterize the terrestrial records (eg. Baxter & Meadows 1999; Valsecchi et al. 2013; Weldeab et

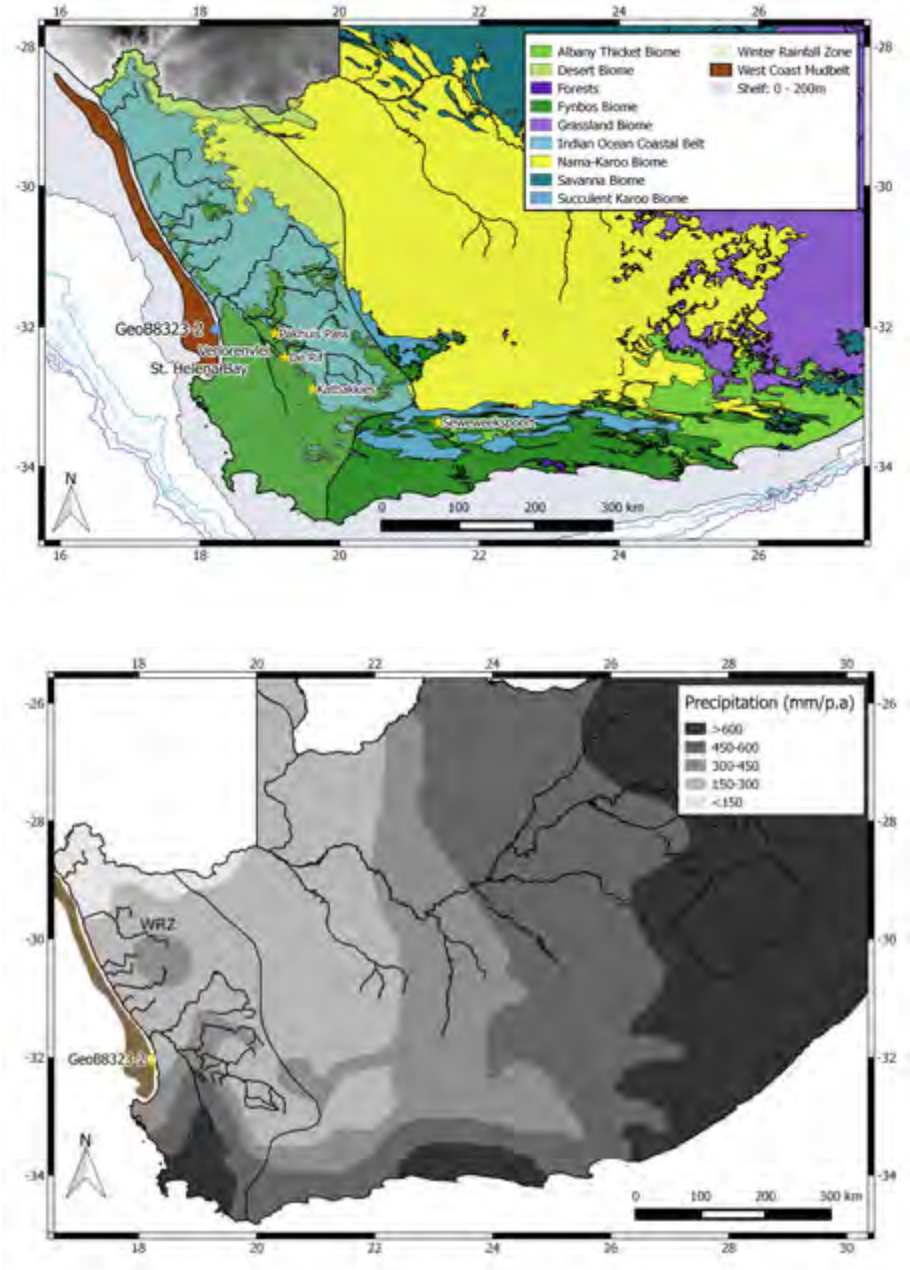

Figure 8: Maps of southern Africa presenting (a) modern vegetation biomes (*Mucina and Rutherford 2006*) and the Winter Rainfall Zone, showing the site of GeoB8323-2 (32°01.89'S and 18°13.19'E), West Coast rivers and the mudbelt into which they drain. Also marked are sites mentioned in text (Verlorenvlei, Pakhuis Pass, De Rif, Katbakkies, Seweweekspoort), and bathymetetric contours at intervals 500m; and (b) modern-day mean annual precipitation (data source: WorldClim1.4 variable bio12 (*Hijmans et al. 2004*)).

al. 2013), several sites have been identified that document Quaternary climate changes in southwest Africa. Over the past few decades, valuable lacustrine records have been extracted from Verlorenvlei (Meadows et al. 1996; Stager et al. 2012; Carr et al. 2015), and climatic conditions of mountainous regions have been inferred from isotopic variation of hyrax middens (Meadows & Sugden 1993; Scott & Vogel 2000; Scott et al. 2004; Quick et al. 2011; Valsecchi et al. 2013; Chase et al. 2015). A large percentage of these studies agree that the WRZ has experienced wetter conditions for much of the past millennium when compared with that of the mid-Holocene. This time period is coincident with the Little Ice Age (LIA) (ca. 1350 – 1800 CE) (Stager et al. 2012; Carr et al. 2015). A substantial increase in precipitation is considered to have begun during this time, around 1400 CE, lasting for several hundred years (Stager et al. 2012; Weldeab et al. 2013; Zhao et al. in press).

Arid conditions are evident in two records from the Katbakkies hyrax midden mountain site from ca. 250 – 1350 CE, at which point the records end (Meadows et al. 2010; Chase et al. 2015). A further mountain record (De Rif) displays an increasingly arid signal over the past thousand years (Chase et al. 2015). However, mountain sites are located near the edge of the WRZ, and this region may be influenced by both summer and winter rainfall. Thus, divergences that occur from WRZ trends are explained as predominantly due to the close proximity of the YRZ and influence of the tropical easterlies. The nebulousness of this WRZ/YRZ border is again visible in a record from Seweweekspoort (Chase et al. 2013). Situated within the YRZ, the isotope records extracted from hyrax middens at this site, give rise to the interpretation of a climate predominantly influenced by austral westerly winds and winter rains.

1.1.3 Controls on the fractionation of δ^{13}C and δD

The ratio between heavy and light carbon isotopes, δ^{13}C, in leaf lipids can be used to distinguish between contributions by plants using different photosynthetic pathways, namely, C_3, C_4, and crassulacean acid metabolism (CAM) (Cerling et al. 1993). The

three pathways produce different carbon isotope compositions of plant organic matter and leaf waxes (Collister et al. 1994). Leaf waxes from C_3 plants are more depleted in ^{13}C than those of C_4 plants (Meyers 1997; Kuechler et al. 2013) while those from CAM plants have intermediate $\delta^{13}C$ compositions. The main controls on leaf wax $\delta^{13}C$ in sediments include changes in vegetation and hydrological dynamics, as well as the isotopic signature of source CO_2 (Scott & Vogel 2000; Carr et al. 2006; Meadows et al. 2010). C_3 plants are generally found in cooler, wetter climates, whereas C_4 plants, being adapted to warmer and drier conditions, are associated with savanna, grassland and desert biomes (Pancost & Boot 2004; Schefuß et al. 2004). $\delta^{13}C$ values for C_3 plant leaf waxes range from -29 to -39 ‰ relative to the Vienna Pee Dee Belemnite standard (VPDB) (Vogts et al. 2009). A period displaying these values at a given time is therefore likely associated with colder and/or relatively more humid conditions. C_4 plant waxes are more enriched in ^{13}C and lie within the range of -14 to -26‰ VPDB. CAM plant values overlap with those of C_3 and C_4, falling at intervals between the two (Vogts et al. 2009; Dupont et al. 2013; Boom et al. 2014). Average values for the *n*-C_{29} alkane are -34.7‰ VPDB and -21.7‰ VPDB for C_3 and C_4 plants, respectively (Castañeda & Schouten 2011).

However, photosynthetic pathways are not the sole influence on the isotopic composition of leaf waxes. Variation in plant $\delta^{13}C$ can also occur due to variable water use efficiency by plants (Ehleringer & Dawson 1992; Hou et al. 2007; Seibt et al. 2008). Water use efficiency refers to the ability of plants to close their stomata to avoid water loss during drought conditions, and is a mechanism often associated with arid to semi-arid regions, including southwest Africa (Tieszen 1991). Stomatal closure results in ^{13}C-enrichment in lipids, whereas times of increased moisture, and thus lower water use efficiency, result in higher ^{13}C-fractionation during photosynthesis and thus depleted $\delta^{13}C$ values of plants (Mooney 1972; Leaney et al. 1985; Ehleringer & Cooper 1988).

Isotope fractionation of precipitation occurs via multiple steps. Moisture precipitates out of vapour form, much of which is sourced from the ocean before travelling some distance inland (Araguas-Araguas et al. 2000; Gonfiantini et al. 2001; Levin et al. 2009).

Fractionation of water (H_20) isotopes also takes place during rainout, but not during the transition from ground to leaf water; once water is taken up by plants, fractionation of leaf wax δD (δD_{leaf}) occurs from the plant-internal leaf water pool (Flanagan & Ehleringer 1991; Fogel & Cifuentes 1993; Sachse et al. 2012). There is a strong linear relationship between the δD_{leaf} and the δD_{precip} of higher plants (Sachse et al. 2012), and δD of leaf waxes is therefore a useful indicator of continental hydrology.

Much of the isotopic variation in δD_{precip} can be attributed to Rayleigh-type processes (Gat 1996). Enrichment and depletion of δD_{precip} can occur via four main processes, which are listed below (Dansgaard 1964; Gat 1996):

1. Changes in the rainfall amount of a region (the amount effect). Variation in available moisture leads to depleted (enriched) δD_{precip} being correlated with higher (lower) rainfall intensity;

2. Changes in the temperature of a region (the temperature effect). δD_{precip} is enriched at higher condensation temperatures;

3. Changes in the over-land distance travelled inland by water vapour before rainout. δD_{precip} becomes more depleted in heavy isotopes as distance travelled from the coast increases (the continental effect); and

4. Changes in the vertical height in the area of rainout. Depletion of δD_{precip} occurs via increasing rainout with increasing height (the altitude effect).

δD_{leaf} is influenced by the characteristics of the vegetation type as well as the environmental conditions experienced by the plant (Ziegler et al. 1976; Smith and Freeman 2006; Feakins and Sessions 2010; Sachse et al. 2012)[2].

i. Photosynthetic pathway (C_3, C_4 or CAM) and plant form/physiology. Different plant types fractionate against δD at different rates;

[2]Light intensity and growth rate, which are sometimes listed as influences on δD_{leaf}, are not included in this list as these factors are chiefly exclusive to algae, and not terrestrial plants.

ii. Water use efficiency. As water use efficiency increases, enriching $\delta^{13}C$, there is a higher fractionation against the heavier water isotope. The plant retains isotopically depleted water and builds waxes depleted in ^{2}H, or D, ie. a negative correlation exists between $\delta^{13}C$ and δD;

iii. Evapotranspiration, including transpiration from both soil and leaf water, with increasing evapotranspiration leading to isotopic enrichment.

2 Methods

2.1 Chronology

The material used in this study was taken from gravity core GeoB8323-2 retrieved from the long, shallow coastal mudbelt to the west of South Africa at 32°01.89'S and 18°13.19'E during RV *Meteor* cruise M57/1. The core's original age model was presented by Herbert & Compton (2007) but has since been revised by Hahn et al. (2015). A hiatus was detected at around 2.27 m core depth (Herbert and Compton 2007). The age just above this hiatus is ca. 2,290 years before present. For this study only the continuously deposited sediments above this hiatus will be considered.

2.2 Core sampling

GeoB8323-2 was stored at 4°C in the MARUM Core Repository at the University of Bremen. 37 samples in total were taken for $\delta^{13}C$ and δD analysis using 1cm-wide syringes to obtain a volume of between 3 and 5 ml per sample, corresponding to a mass of between 2.5 and 6.5 g dry sediment. The samples were obtained at 5 cm intervals between 0 to 150 cm; below this depth, samples were taken every 10 cm. Samples were freeze-dried and ground using a mortar and pestle before extraction.

2.3 Laboratory procedure

The preparation and measuring of samples was carried out using the same method as described by Collins et al. (2011). Samples were extracted by a DIONEX ASE200 at 100°C and 1000 psi using a solvent mixture of DCM:MeOH = 9:1. Squalene was added as an internal standard before extraction. Extraction was conducted at 1000 psi and 100°C for 3 cycles with 5 minutes per cycle, after which rotary evaporation was performed to remove solvents from total lipid extracts. Saponification with 0.1m KOH at 85°C for 2 hours removed wax esters, and neutral fractions were extracted via liquid-liquid extraction using hexane. Neutral fractions were further separated using column chromatography with 1%-deactivated silica and hexane, in order to obtain a hydrocarbon fraction. An $AgNO_3$ column was used to remove unsaturated hydrocarbons.

Gas chromatography/flame ionization detection of *n*-alkane concentrations was performed using a ThermoFischer Scientific Focus GC at MARUM at the University of Bremen. An external standard was assessed multiple times during analyses to evaluate the precision of the quantification. The precision of C_{18} to C_{35} *n*-alkanes, based on the standard deviation of repeated analyses of the standard measurements is 3.6%. The Average Chain Length (ACL) and Carbon Preference Index (CPI) were calculated using the alkane concentration measurements. $ACL_{25\text{-}33}$ was calculated via the following equation:

$$ACL = \frac{\sum(iX_i)}{\sum(X_i)}$$

where X_i is the abundance of the *n*-alkane (*n*-C_{25} to *n*-C_{33}) with i number of carbon atoms. The CPI ratio provides an indication of odd- to even-numbered *n*-alkanes in a sample, within the range C_{25} to C_{33}. Strong odd over even preference (where CPI > 1) is indicative of fresh, non-degraded plant organic matter (Kolattukudy 1976). CPI was determined using the following equation:

$$CPI_{(25-33)} = 0.5\frac{(C25 + C27 + C29 + C31 + C33)}{(C24 + C26 + C28 + C30 + C32)} + 0.5\frac{(C25 + C27 + C29 + C31 + C33)}{(C26 + C28 + C30 + C32 + C34)}$$

2.4 δ^{13}C and δD analysis

Compound specific δ^{13}C analyses were performed using a Thermo Trace GC Ultra, coupled via a combustion interface at 1000°C, to a Finnigan MAT 252 isotope ratio monitoring mass spectrometer (GC/IR-MS) against calibrated CO_2 reference gas. Stable hydrogen isotope analysis was performed at MARUM at the University of Bremen, using a Thermo Trace GC coupled, using a pyrolysis reactor at 1420°C, to a Thermo Fischer MAT 253 isotope ratio mass spectrometer against calibrated H_2 reference gas. δ^{13}C values are given in delta notation relative to the VPDB standard and δD results are given in delta notation relative to the Vienna Standard Mean Ocean Water (VSMOW) standard.

The squalane internal standards for δ^{13}C and δD (δ^{13}C = -18.9±0.2 ‰ and δD=-180±2‰) produced values of -19.0±0.2‰ and -176±2 ‰ (n=37) respectively. Average precision of repeated analyses for the C_{29} *n*-alkane (1σ) is 0.2‰ for δ^{13}C and 1‰ for δD. For the C_{31} *n*-alkane, precision is 0.1‰ for δ^{13}C and 1‰ for δD. The long-term accuracy and precision of the external *n*-alkane standard is 0 and 0.3‰, respectively, for δ^{13}C analyses and 0 and 3‰, respectively, for δD analyses.

3 Results

3.1 Isotopic composition of carbon and hydrogen

The strong odd-over-even dominance of the leaf wax *n*-alkanes is indicated by the high Carbon Preference Indices (CPI) ranging from 9.8 to 14.2 (n=37) with a mean of 11.8. Average Chain Length (ACL) values of the leaf wax *n*-alkanes vary only minimally between 30.9 and 31.1 with a mean of 31.0.

δ^{13}C values of the *n*-C_{29} and *n*-C_{31} alkanes exhibit similar patterns in variation, but fall into different isotopic ranges (-26.9 to -28.7‰ VPDB and -25.5 to -26.5‰ VPDB respectively) (Figure 9a). Deviation between the two homologues occurred only between 150 and 300 CE and 1000 and 800 CE. Maximum *n*-C_{29} ^{13}C-depletion occurred from between 1800 to 1900 CE and maximum ^{13}C-enrichment was found at ca. 800 CE and from

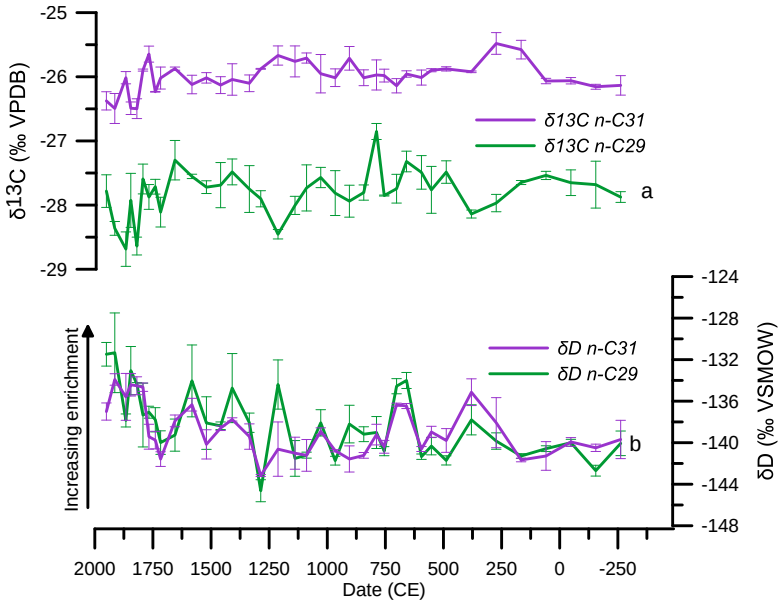

Figure 9: Comparison between *n*-alkanes C_{29} (green) and C_{31} (purple) for (a) stable compound carbon isotope analysis; and (b) stable compound hydrogen isotope analysis.

ca. 600 to 650 CE. Two periods of relative stability were observed to occur throughout the record, from 150 BCE to 150 CE and 1400 to 1600 CE (variation = 0.2‰). The largest and most rapid variability during the last 2,250 years occurred from ca. 1650 CE to the present. Although the variation during this recent period is proportionally large with respect to the remainder of the record, it is still within the relatively small 1.8‰ range.

Up until ca. 250 CE, both $\delta^{13}C$ and δD varied minimally, but thereafter the records diverged as more variability occurred (Figures 9a and 9b). Both δD homologues (*n*-C_{29} and *n*-C_{31}) display a similar range of values and similar variations with values ranging from -131 to -145‰ VSMOW and maximum depletion found around 1300 CE (Figure 9b). At 1750 CE, a shift towards enriched δD values began, a trend which continued until the present. This coincides with a period of $\delta^{13}C$ depletion. Stable periods are found prior to 300 CE, and from 750 to 1150 CE, varying by 3 and 4‰ VSMOW, respectively.

3.2 Vegetation-corrected δD ($\delta\mathbf{D_{vc}}$)

To account for isotope fractionation depending on vegetation type and reconstruct estimated precipitation isotope compositions, we calculated a mixed apparent fractionation factor (ϵ) based on the vegetation in the catchment area and pollen findings from this core (Zhao et al. 2015). We used the following percentages of plant photosynthetic types for these calculations: C_3= 50%; C_4= 20%; CAM= 30% (estimated using findings from Zhao et al. 2015). As end-member fractionation factors we use an apparent fractionation value of ϵ = -113±18‰ (n=183) for Fynbos C_3 plants (dicots and gymnosperms) (Sachse et al. 2012). For C_4 grasses we use the mean apparent fractionation value of ϵ = -139±25‰ (n=56) (monocots) (Sachse et al. 2012). These values are based on leaf wax *n*-alkane measurements from multiple sites across the world, and are biased towards mid-latitude regions (Sachse et al. 2012). Apparent fractionation values for CAM plants have not been extensively recorded, but we use the value estimated by Feakins & Sessions (2010) (ϵ = -114±22‰; n=17) to approximate the δD_{leaf} correction for the succulents in our sample. The estimated mixed apparent fractionation factor based on these assumptions is calculated to - 118±12‰.

The vegetation-corrected isotope composition representing estimates of rainfall isotope compositions are calculated using the following equation (Sachse et al. 2012; Collins et al. 2013):

$$\delta D_{vc} = \left[\frac{(\delta D_{wax} + 1000)}{\left(\frac{\varepsilon}{1000}\right) + 1} \right] - 1000$$

where δD_{vc} is the vegetation-corrected δD value; δD_{wax} represents the measured δD values and ϵ is the estimated mixed apparent fractionation factor.

4 Discussion

4.1 δ^{13}C

4.1.1 Spatial variation in West Coast vegetation

The total δ^{13}C range of 1.8‰ of leaf-wax *n*-alkanes in GeoB8323-2 within the last 2,250 years is small in comparison to the amplitude of changes associated with other effects on δ^{13}C. Shifts in photosynthetic pathways can cause changes in magnitude of the order of 10-15‰ while fluctuations in water-stress have been demonstrated to be the cause of to up to 5‰ change within a plant (Farquhar et al. 1989; Tieszen 1991). However, although small, the documented changes are still significant. A Cederberg hyrax midden study by Quick et al. (2011) also displayed minimal δ^{13}C change over a much longer period, revealing limited vegetation dynamics in this area.

Leaf-wax δ^{13}C values fall between those usually associated with C_3 and C_4 plants. Since the catchment areas of West Coast rivers draining into the mudbelt span several biomes, terrestrial organic matter in sediments from GeoB8323-2 is expected to consist of a mixture of C_3, C_4 and CAM plant organic material (Hahn et al. 2015; Zhao et al. 2015). The dominant source of C_3 material is most likely the FB biome, where C_3 shrubs proliferate. In their comparison between FB and SK vegetation, Carr et al. (2014) documented clear differences between the two biomes regarding their *n*-alkane distributions. The former was found to possess, on average, a shorter chain length than the latter, maximizing at *n*-C_{29}. This is true in the cases of both Montane and Lowland Fynbos. Confirmation of the strong Fynbos signal embedded in the GeoB8323-2 record was reported by Zhao et al. (2015), confirming that the Olifants River is a large contributor to deposition of terrestrial material to the west coast mudbelt. Combined, these studies suggest that carbon isotopic variations in the C_{29} *n*-alkane homologue can mainly be ascribed to changes in Fynbos vegetation.

Further north, the dwarf leaf-succulents (CAM) and grasses (C_4) indigenous to the SK produce leaf-wax *n*-alkanes with longer chains, with a maximum at *n*-C_{31} (Boom et

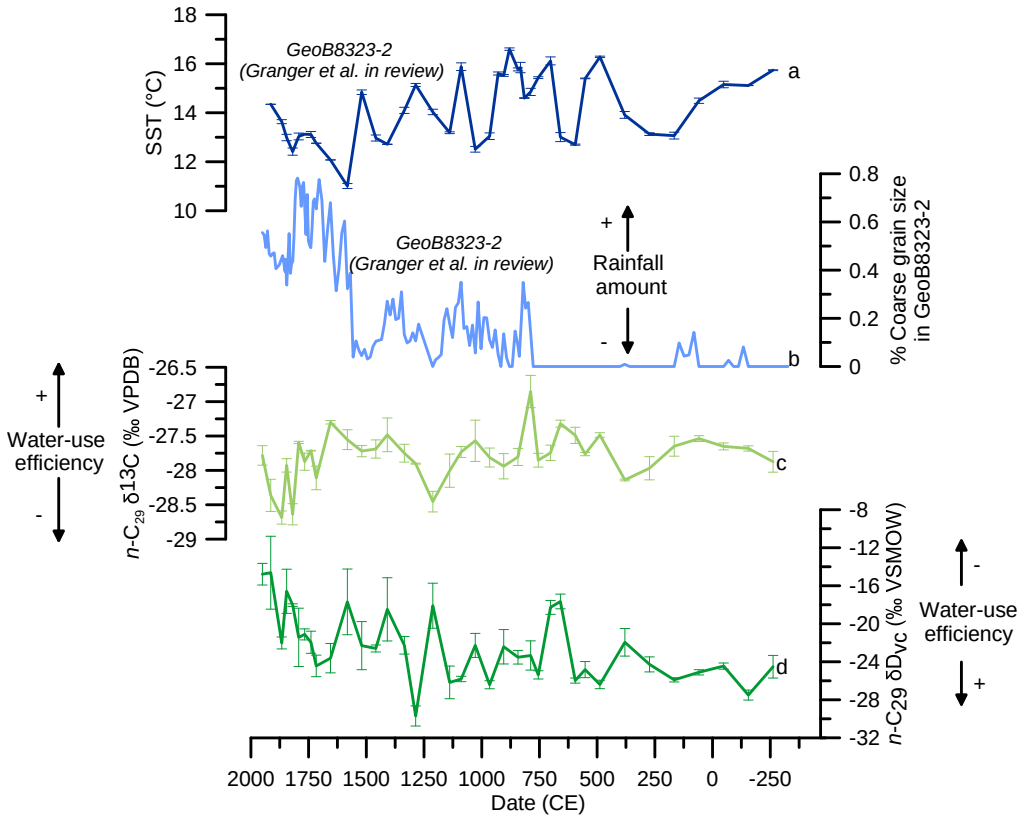

Figure 10: GeoB8323-2 results of (a) sea-surface temperature (Granger et al. in review); (b) coarse end-member (EM1) of grain size analysis (Granger et al. in review), indicative of changes in WRZ rainfall amount; (c) *n*-alkane C_{29} for $\delta^{13}C$; and (d) *n*-alkane C_{29} for δD_{precip} using calculated ϵ from mixed core-top vegetation estimate.

al. 2014; Carr et al. 2014). Consequently, the dominance of this chain-length throughout our record indicates that a large portion of plant organic material in this section of the mudbelt is derived from the SK. A comparison between changes in C_{29} and C_{31} revealed only subtle differences in Fynbos and succulent plant variation. Apart from two short periods (150 – 300 CE and 800 – 1000 CE), variation patterns within the two biomes during the late Holocene remain similar to one another.

4.1.2 Late Holocene δ^{13}C dynamics in the WRZ

The δ^{13}C results from the core suggest that vegetation in the source region has not changed significantly throughout the past 2,250 years. This is supported by palynological investigations (Zhao et al. in press) and is in accordance with several other vegetation studies in the WRZ which concluded that regional vegetation has remained relatively resistant to substantial climate shifts, particularly within the Fynbos biome (Meadows et al. 2010; Quick et al. 2011; Carr et al. 2015). Limited vegetative change is indicative of either a) minor hydrological change in the region, or b) high plant resilience to environmental changes. To determine which scenario is more likely, isotope results are compared to previous WRZ studies. Using grain size and inorganic geochemical data from the same archive, Granger et al. (in review) identified SST varibility and dynamic precipitation changes in the region during the late Holocene (Figures 10a and 10b). These findings, coupled with the knowledge of vegetation resilience in the region, favours the latter scenario, i.e. relatively resistant vegetation against environmental changes. The observed variations, which are most marked in the last 250 years of the record, may therefore be more indicative of changes in water stress / water use efficiency of a relatively stable vegetation cover. This effect would be reflected as an enrichment of δ^{13}C and limitation of transpiration during arid periods due to stomatal closure (Farquhar et al. 1989).

The driest period in southwest Africa, according to evidence collected through δ^{13}C analysis, occurred at around 800 CE (Figure 10c). After this time, the climate appears to have been relatively steady for the next three centuries, lasting until midway into the Medieval Climate Anomaly (MCA = ca. 950 to 1250 CE). The δ^{13}C results are also indicative of a relatively recent increase in humidity, revealing a noticeably wetter past 250 years in southwestern Africa than during the previous two millennia. A distinctive trend towards more humid conditions began from ca. 1650 CE. This recent shift towards wet conditions is in accordance with increased coeval grain size in GeoB8323-2 indicating increased fluvial discharge (Granger et al. in review) and other proxy data from studies in the Verlorenvlei region, although the signal lags that recorded by dilute-water atoms

by ca. 300 years (Meadows et al. 1996; Stager et al. 2012; Carr et al. 2015). GeoB8323-2 $\delta^{13}C$ data thus indicate that the peak period of moisture availability in the region coincided with the later stages of the LIA, ca. 1800 to 1900 CE. This observation supports the conclusions of Stager et al. (2012), who concluded that peak rainfall in this region occurred during the LIA, at around 1850 CE.

4.2 δD

4.2.1 Estimated precipitation δD compositions:

Figure 10d plots the results of the vegetation-corrected δD. Using the estimated mixed apparent fractionation factor based on the vegetation composition as previously described, we estimated the modern precipitation δD from the core-top values, resulting in a δD_{vc} of -14.2‰. Comparing this to the mean annual weighted isotopic composition of precipitation (δD_{map}) value for Cape Town (-13.1‰) (West et al. 2014), the close agreement of both values (see Figure 11) suggests that our assumptions of vegetation compositions and associated apparent fractionation factors are valid and that changes in plant physiology can be considered negligible in determining the observed δD_{vc} changes. In the following sections the potential effects of other processes on the temporal δD_{vc} changes are discussed.

Should the amount effect have been the dominant control of precipitation isotope compositions reflected in the leaf-wax δD, southwest Africa would have experienced increasingly arid conditions throughout the last millennium and wetter conditions would have existed prior to 300 CE and again from 750 to 1350 CE. In strong contrast to this, multiple previous palaeoclimatic studies from this region (including those using GeoB8323-2) have indicated that the late Holocene has been characterized by an increasingly moist WRZ (Meadows and Baxter 2001; Stager et al. 2012; Weldeab et al. 2013; Carr et al. 2015; Granger et al. in review). Although it is possible that the δD record could be reflecting an SRZ signal and suppressing that of the WRZ, there is little evidence for this, since other proxy data from the same core, including $\delta^{13}C$ (this study), show an

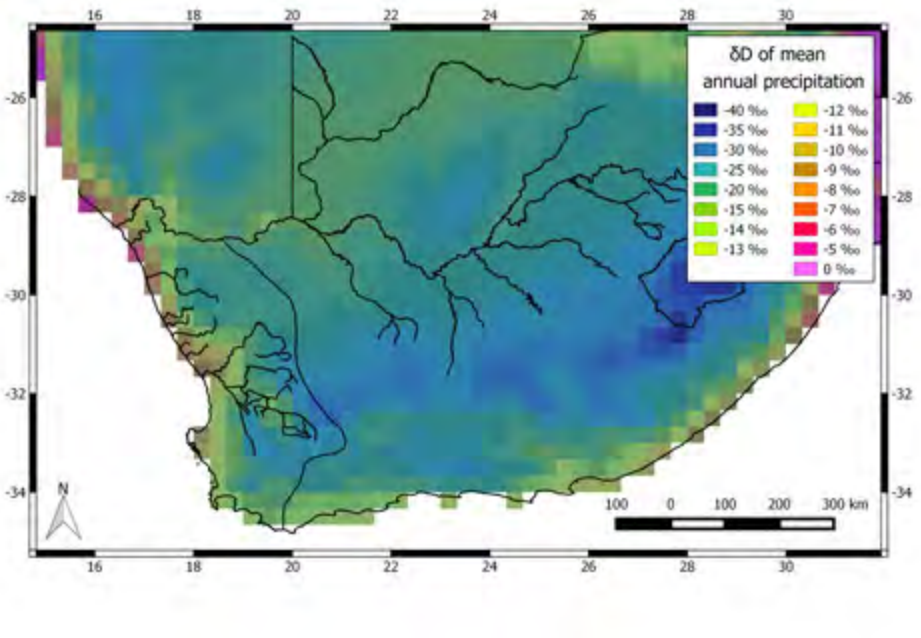

Figure 11: Measured δD of groundwater and tap water in South Africa overlaid on an isotopic landscape model (data sourced from www.waterisotopes.org), representative of modern-day isotopic composition of δD_{precip}.

increasingly humid signal. Zhao et al. (2015) were able to identify stark differences in pollen that corresponded to different rainfall regimes, and GeoB8323-2 showed a strong Fynbos signal (unique to the WRZ) throughout the past 2,250 years. For these reasons, the amount effect is not considered to be a governing factor of the observed δD changes during the late Holocene.

Temperature variation as a main driver of changes in the record also appears to be unlikely. δD_{precip} becomes depleted when condensation occurs at low temperatures (Dansgaard 1964). Using Benguela Current SST data from Granger et al. (in review) as a proxy for southwest African temperature variation, this relationship is found to be inconsistent with δD data from GeoB8323-2 (Figure 10d). The latter half of the records in particular presents a contradictory view, that of cool SSTs and accompanying δD enrichment. The temperature effect is therefore also rejected as a candidate for significant influence on

δD_{precip} variation. Similarly, evapotranspiration can be ruled out as a major control on leaf-wax δD. During wettest times, i.e. LIA, evapotranspiration effects should be minor but, instead, the most enriched leaf-wax δD is observed.

The factor of water use efficiency, however, is a prominent influence on the stable carbon isotope composition of plants in semi-arid regions (Tieszen 1991), and having identified it as the most significant cause of variation in the δ^{13}C record, its effects on δD must also be considered. Changes in water use efficiency display a negative linear relationship between δ^{13}C and δD of waxes (Hou et al. 2007). While over the entire record (Figure 12a) no correlation exists between δ^{13}C and δD of waxes (Fig. 12a) a negative correlation is evident in the record prior to 600 CE (Figure 12b) where R^2=0.59 and from ca. 1650 to 1850 CE (R^2=0.23) (Figure 12c). The lack of correlation between δD and δ^{13}C throughout the remainder of the record, however, suggests that changes in water use efficiency can only partly explain the observed temporal δD changes in the record.

In addition, the continental and altitude effects might further explain changes in the observed leaf-wax δD changes. The two effects of distance and altitude have been shown to dominate in areas where large changes in altitude occur over a relatively short distance, as is the case for the WRZ (Dansgaard 1964; Gat 1996). Parts of the Cederberg Mountain Range (within the Cape Fold Mountain region) rise within 40 km of the coast, to a mean elevation between 1,200 and 1,500 m (Quick et al. 2011). Unfortunately, although this effect has been shown to have significantly influenced δD in coastal regions, very little data exists on the magnitude of such changes. More commonly documented are gradients in δ^{18}O of precipitation. Well-correlated to δD, changes in δD composition can be up to eight times greater than those in δ^{18}O (Vimeux et al. 2001; Tierney et al. 2011). Altitudinal δ^{18}O gradients in the regions of Mt Kilimanjaro, Ecuador and Mexico have been recorded as ranging from ~ -3‰, -1.7‰ and -2‰ per km height respectively (Gonfiantini et al. 2001), whilst the gradient inland from the Gulf of Guinea to eastern Cameroon averaged -4‰ over 600km (Njitchoua et al. 1999).

Therefore, in addition, a 'selective continental effect' might further explain changes in the observed leaf-wax δD changes. For this study, a tentative model is proposed. If we assume that the bulk of terrigenous sediment originated from coastal areas within the catchment (as opposed to the further inland, mountainous regions), recorded δD would be most representative of regions situated close to the ocean. During times of aridity, moisture will not penetrate far inland, and thus the majority of it precipitates out over the coastal regions, leading to a relatively depleted δD signal due to full moisture rainout. In contrast, during times of increased humidity, isotopically-depleted moisture will be able to migrate further inland after initial coastal rainout, leaving precipitation over the coastal region relatively D-enriched. Using this model, an increasingly depleted δD signal such as is observed from ca. 400 to 1300 CE (Figure 9b), would indicate a decrease in coastal rainfall amount, whilst a trend towards more enriched δD values (observed in the latter stages of the record during the period from ca. 1300 to 1950 CE) may thus represent a shift towards increasing coastal rainfall, supplemented with an increase in mountainous rainfall. Although the difficulty in isolating driving forces, and the developmental nature of this preliminary model is stressed here, this explanation is consistent with the anti-correlation observed between δ^{13}C and δD. Overall, the high degree of variability between δD, δ^{13}C and other proxies suggests a complex combination of drivers of varying strength throughout the late Holocene.

4.2.2 Late Holocene δD dynamics

Interpreting hydrological changes via δD without knowledge from additional proxies would present a near-impossible task, due to the multitude of factors influencing isotopic composition. Using the records of δ^{13}C (this study), grain size and SST (Granger et al. in review), a coherent preliminary analysis of climatic variation begins to develop.

Prior to 600 CE, conditions were largely controlled by stomatal closure and moisture availability, with a slight increase in water use efficiency being suggestive of arid conditions

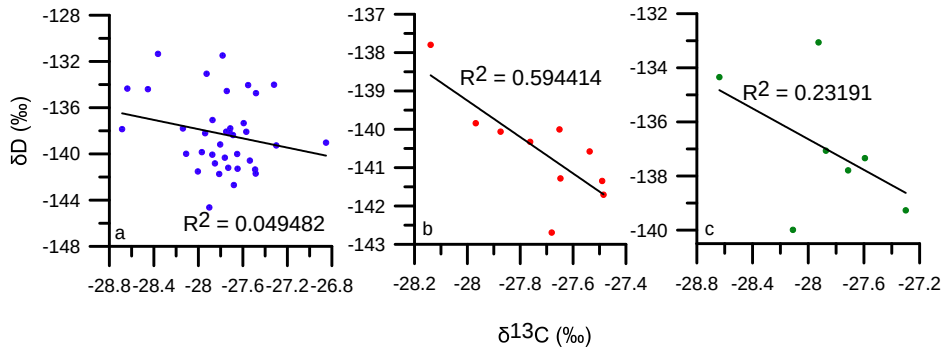

Figure 12: δD vs δ^{13}C correlation graphs, showing (a) full record (n=37); (b) 250 BCE – 600 CE (n=10); and (c) 1650 – 1850 CE (n=7), where R^2 represents the correlation coefficient.

throughout the catchment. This is roughly consistent with findings from Granger et al. (in review), as well as with hyrax midden data from the South Coast (Chase et al. 2015), where dry conditions were hypothesized to have existed until ca. 350 CE. The two centuries following 600 CE were more mesic, but a distinct rise in humidity began from ca. 800 CE, and increasingly wet conditions prevailed until relatively recently (ca. 1900 CE).

The visibly strong relationship between δD and δ^{13}C arising from the effect of water use efficiency on isotopic composition breaks down in the middle of the record, and it is likely that the altitude and continental effects become more influential during this period, which consists of highly variable hydrogen isotopic compositions. This could be a response to larger-scale forcing.

The LIA appears to have been climatologically variable. This sudden change in the δD/δ^{13}C relationship indicates that a complex mixture of driving forces were exerted on the records, with the possible inclusion of the amount effect. Should we infer δD changes here to be driven by a mixture of water use efficiency, altitude and continental rainout processes, the start of the LIA (~1350 CE) would have consisted of an increase in coastal precipitation, in addition to increasing mountainous rainfall. During the latter stages of the epoch, humidity increased to peak record levels at around 1850 CE.

Despite the concurrence of this research with several late Holocene studies within the WRZ, others have argued for climate changes that are not identifiable in this record, especially those positioned within the Cederberg. A synthesis of multiple studies has revealed clear disparities between various records within the mountains and it is apparent that neighbouring environments exert unique climate signals, even at short distances from one another (Valsecchi et al. 2013). Our record adds to this mosaic, concurring with some and diverging with others.

It is difficult to assess the degree to which changes in the amount of summer rainfall influenced the record of GeoB8323-2 via the Orange River; however, the end-member analysis by Granger et al. (in review) (Figure 10a), provenance studies (Hahn et al. 2015), and pollen analysis by Zhao et al. (2015) strongly indicate a regional response to WRZ climate conditions recorded at the site of GeoB8323-2. In addition, the complexity that CAM plants are known to exert on isotopic records, may play a role in the enrichment and depletion of the signals observed in GeoB8323-2.

5 Conclusions

This study presents two new isotope records from the WRZ of southwestern Africa, and evaluated the significance of compound-specific isotope variation in leaf-waxes in this specific area within the context of earlier palaeoenvironmental findings.

The leaf-wax $\delta^{13}C$ data suggest a mix of C_3, C_4 and CAM plants in accordance with pollen data from the same archive (Zhao et al. in press). The modest changes in the $\delta^{13}C$ record during the last 2,250 years are consistent with documented Fynbos resilience to environmental changes. Despite several significant hydrological shifts having been recorded in southwest Africa during the late Holocene, there apparently was a muted response from vegetation. Consequently, the small variations in $\delta^{13}C$ are interpreted as indicative of changes in water stress / water use efficiency in this semi-arid area. Leaf-wax δD composition is also affected by these changes; however, this is only apparent in certain periods of the record. At other times, the topographical effects of rainout

and the transport of isotopically depleted moisture away from coastal locations under wetter conditions seems to have a significant effect on the observed temporal leaf-wax δD variation in this setting. The leaf-wax δD composition in this record is therefore partly indicative of spatial changes of rainfall within the WRZ.

The addition of CAM plants to the record, combined with the multitude of possible effects on isotope composition necessitates analysis of further data in the reconstruction of Quaternary climates. This study therefore highlights the need for additional, independent proxy data to be used in conjunction with isotopes, in order to adequately interpret palaeo-climatic changes in compound-specific isotope compositions in the semi-arid WRZ of South Africa.

Acknowledgments

The authors would like to acknowledge the funding support received from the National Research Foundation (NRF), in respect of a grantholder bursary, and the Deutsche Akademie Austauschdienst (DAAD), who facilitated travel between the University of Cape Town and the University of Bremen. The authors also wish acknowledge the contributions made by the captain and crew of the RV *Meteor* M57/1 cruise, during which marine core GeoB8323-2 was collected. Further thanks go to Ralph Kreutz, who assisted in the preparation of samples, and to Matthias Zabel, Nicole Herrmann, and James Collins for their insightful commentaries on the text.

References

1. Araguas-Araguas, L., Froehlich, K. & Rozanski, K., 2000. Deuterium and oxygen-18 isotope composition of precipitation and atmospheric moisture. Hydrological Processes, 14, pp.1341–1355.

2. Boom, A., Carr, A.S., Chase, B.M., Grimes, H.L. & Meadows, M.E., 2014. Organic Geochemistry Leaf wax *n*-alkanes and d 13 C values of CAM plants from arid southwest Africa. Organic Geochemistry, 67, pp.99–102.

3. Carr, A.S., Boom, A., Chase, B.M., Meadows, M.E. & Grimes, H.L., 2015. Holocene sea level and environmental change on the west coast of South Africa: evidence from plant biomarkers, stable isotopes and pollen. Journal of Paleolimnology, 53, pp.415–432.

4. Carr, A.S., Boom, A., Grimes, H.L., Chase, B.M., Meadows, M.E. & Harris, A., 2014. Leaf wax *n*-alkane distributions in arid zone South African flora: Environmental controls, chemotaxonomy and palaeoecological implications. Organic Geochemistry, 67, pp.72–84.

5. Castañeda, I.S. & Schouten, S., 2011. A review of molecular organic proxies for examining modern and ancient lacustrine environments. Quaternary Science Reviews, 30, pp.2851–2891. Available at: http://dx.doi.org/10.1016/j.quascirev.2011.07.009.

6. Cerling, T., Wang, Y. & Quade, J., 1993. Expansion of C_4 ecosystems as an indicator of global ecological change in the late Miocene. Letters to Nature, 361, pp.344–345.

7. Chase, B.M., Boom, A., Carr, A.S., Carré, M., Chevalier, M., Meadows, M.E., Pedro, J.B., Stager, J.C. & Reimer, P.J., 2015. Evolving southwest African response to abrupt deglacial North Atlantic climate change events. Quaternary Science Reviews, 121, pp.132–136.

8. Chase, B.M., Boom, A., Carr, A.S., Meadows, M.E. & Reimer, P.J., 2013. Holocene climate change in southernmost South Africa: rock hyrax middens record shifts in the southern westerlies. Quaternary Science Reviews, 82, pp.199–205.

9. Chase, B.M., Lim, S., Chevalier, M., Boom, A., Carr, A.S., Meadows, M.E. & Reimer, P.J., 2015. Influence of tropical easterlies in southern Africa's winter rainfall zone during the Holocene. Quaternary Science Reviews, 107, pp.138–148.

10. Collins, J.A., Schefuß, E., Mulitza, S., Prange, M., Werner, M., Tharammal, T., Paul, A. & Wefer, G., 2013. Estimating the hydrogen isotopic composition of past precipitation using leaf-waxes from western Africa. Quaternary Science Reviews, 65, pp.88–101.

11. Collister, J.W., Rieley, G., Stern, B., Eglinton, G. & Fry, B., 1994. Compound-specific δ ^{13}C analyses of leaf lipids from plants with differing carbon dioxide metabolisms. Organic Geochemistry, 21, pp.619–627.

12. Cowling, R.M., Richardson, D.M. & Pierce, S.M., 2004. Vegetation of Southern Africa, Cambridge University Press.

13. Dansgaard, W., 1964. Stable isotopes in precipitation. Tellus 16, pp. 436-468.

14. Ehleringer, J.R. & Cooper, T.A., 1988. Correlations between Carbon Isotope Ratio and Microhabitat in Desert Plants. Oecologia, 76, pp.562–566.

15. Ehleringer, J.R. & Dawson, T.E., 1992. Water uptake by Plants: perspectives from stable isotope composition. Plant, Cell and Environment, 15, pp.1073–1082.

16. Farquhar, G.D., Ehleringer, J.R. & Hubick, K.T., 1989. Carbon isotope discrimination and photosynthesis. Annual Review of Plant Physiology and Plant Molecular Biology, 40, pp.503–537.

17. Feakins, S.J. & Sessions, A.L., 2010. Crassulacean acid metabolism influences D/H ratio of leaf wax in succulent plants. Organic Geochemistry, 41, pp.1269–1276. Available at: http://dx.doi.org/10.1016/j.orggeochem.2010.09.007.

18. Flanagan, L.B. & Ehleringer, J.R., 1991. Effects of Mild Water Stress and Diurnal Changes in Temperature and Humidity on the Stable Oxygen and Hydrogen Isotopic Composition of Leaf Water in *Cornus stolonifera* L. The Journal of Plant Physiology, 97, pp.298–305.

19. Fogel, M.L. & Cifuentes, L. A., 1993. Isotope Fractionation during Primary Production. Organic Geochemistry, pp.73–98.

20. Gat, J.R., 1996. Oxygen and Hydrogen Isotopes in the Hydrologic Cycle. Annual Review of Earth and Planetary Sciences, 24, pp.225–262. Available at: http://www.annualreviews.org/doi/abs/10.1146/annurev.earth.24.1.225.

21. Gonfiantini, R., Roche, M.A., Olivry, J.C., Fontes, J.C. & Zuppi, G.M., 2001. The altitude effect on the isotopic composition of tropical rains. Chemical Geology, 181, pp.147–167.

22. Granger, R., Meadows, M.E., Hahn, A., Stuut, J.-B.W., Hermann, N., Zabel, M. & Schefuß, E, 2016. Quaternary Science Reviews. In Review. Coupling between late Holocene sea-surface temperature and terrestrial hydrology in southwestern Africa.

23. Hahn, A., Compton, J., Meyer-Jacob, C., Kirsten, K., Lucassen, F., Mayo, M., Schefuß, E. & Zabel, M., Holocene paleoclimatic record from the South African Namaqualand mudbelt: A source to sink approach. Quaternary International, 2015, pp.1–15.

24. Herbert, C.T. & Compton, J., 2007. Geochronology of Holocene sediments on the western margin of South Africa. South African Journal of Geology, 110, pp.327–338. Available at: http://sajg.geoscienceworld.org/cgi/doi/10.2113/gssajg.110.2-3.327.

25. Hijmans, R.J., Cameron, S. & Parra, J., 2004. WorldClim, Version 1.4 (release 3). A square kilometer resolution of global terrestrial surface climate.

26. Hou, J., D'Andrea, W.J., MacDonald, D. & Huang, Y., 2007. Evidence for water use efficiency as an important factor in determining the δD values of tree leaf waxes.

Organic Geochemistry, 38, pp.1251–1255.

27. Kolattukudy, P.E., 1976. Chemistry and biochemistry of natural waxes. Elsevier Scientific Pub. Co.Amsterdam, New York.

28. Leaney, F.W., Osmond, C.B., Allison, G.B. & Ziegler, H., 1985. Hydrogen isotope composition of leaf water in C_3 and C_4 plants - its relationship to the hydrogen isotope composition of dry matter. Planta, 164, pp.215–220.

29. Levin, N.E., Zipser, E.J. & Cerling, T.E., 2009. Isotopic composition of waters from Ethiopia and Kenya: Insights into moisture sources for eastern Africa. Journal of Geophysical Research, 114, pp. 1-13. Available at: http://doi.wiley.com/10.1029/2009JD012166.

30. Meadows, M.E. & Sugden, J.M., 1993. The late quaternary palaeoecology of a floristic kingdom: the southwestern Cape South Africa. Palaeogeography, Palaeoclimatology, Palaeoecology, 101, pp.271–281.

31. Meadows, M.E. & Baxter, A.J., 2001. Holocene vegetation history and palaeoenvironments at Klaarfontein Springs, Western Cape, South Africa. The Holocene, 11, pp.699–706. Available at: http://hol.sagepub.com/cgi/doi/10.1191/09596830195726.

32. Mooney, H.A., 1972. The Carbon Balance of Plants. Annual Review of Ecology and Systematics, 3, pp.315–346.

33. Njitchoua, R., Sigha-Nkamdjou, L., Dever, L., Marlin, C., Sighomnou, D. & Nia, P., 1999. Variations of the stable isotopic compositions of rainfall events from the Cameroon rain forest, Central Africa. Journal of Hydrology, 223, pp.17–26.

34. O'Leary, M.H., 1988. Carbon Isotopes in Photosynthesis. BioScience, 38, pp.328–336.

35. Pancost, R.D. & Boot, C.S., 2004. The palaeoclimatic utility of terrestrial biomarkers in marine sediments. Marine Chemistry, 92, pp.239–261.

36. Quick, L., Chase, B.M., Meadows, M.E., Scott, L. & Reimer, P.J., 2011. A 19.5kyr vegetation history from the central Cederberg Mountains, South Africa: Palynological evidence from rock hyrax middens. Palaeogeography, Palaeoclimatology, Palaeoecology, 309, pp.253–270. Available at: http://dx.doi.org/10.1016/j.palaeo.2011.06.008.

37. Rommerskirchen, F., Eglinton, G., Dupont, L., Güntner, U., Wenzel, C. & Rullkötter, J., 2003. A north to south transect of Holocene southeast Atlantic continental margin sediments: Relationship between aerosol transport and compound-specific δ^{13}C land plant biomarker and pollen records. Geochemistry, Geophysics, Geosystems, 4, pp.1–29. Available at: http://doi.wiley.com/10.1029/2003GC000541.

38. Rutherford, M.C. & Westfall, R.H., 1994. Biomes of southern Africa: an objective categorization, ed 2. Memoirs of the Botanical Survey of South Africa, 63, pp.1-94.

39. Sachse, D., Billault, I., Bowen, G.J., Chikaraishi, Y., Dawson, T.E., Feakins, S.J., Freeman, K.H., Magill, C.R., McInerney, F. a., van der Meer, M.T.J., Polissar, P., Robins, R.J., Sachs, J.P., Schmidt, H.-L., Sessions, A.L., White, J.W.C., West, J.B. & Kahmen, A., 2012. Molecular paleohydrology: interpreting the hydrogen-isotopic composition of lipid biomarkers from photosynthesizing organisms. Annual Review of Earth and Planetary Sciences, 40, pp.221–249. Available at: http://www.annualreviews.org/doi/abs/10.1146/annurev-earth-042711-105535

40. Schefuß, E., Versteegh, G.J.., Jansen, J.H.. & Sinninghe Damsté, J.., 2004. Lipid biomarkers as major source and preservation indicators in SE Atlantic surface sediments. Deep Sea Research Part I: Oceanographic Research Papers, 51, pp.1199–1228.

41. Scott, L., Marais, E. & Brook, G.A., 2004. Fossil hyrax dung and evidence of Late Pleistocene and Holocene vegetation types in the Namib Desert. Journal of Quaternary Science, 19, pp.829–832. Available at: http://doi.wiley.com/10.1002/jqs.870.

42. Scott, L. & Vogel, J.C., 2000. Evidence for environmental conditions during the

last 20 000 years in Southern Africa from ^{13}C in fossil hyrax dung. Global and Planetary Change, 26, pp.363–365.

43. Seibt, U., Rajabi, A., Griffiths, H. & Berry, J. A., 2008. Carbon isotopes and water use efficiency: Sense and sensitivity. Oecologia, 155, pp.441–454.

44. Stager, J.C., Mayewski, P.A., White, J., Chase, B.M., Neumann, F.H., Meadows, M.E., King, C.D. & Dixon, D.A., 2012. Precipitation variability in the winter rainfall zone of South Africa during the last 1400 yr linked to the austral westerlies. Climate of the Past, 8, pp.877–887.

45. Tierney, J.E., Russell, J.M., Sinninghe Damsté, J.S., Huang, Y. & Verschuren, D., 2011. Late Quaternary behavior of the East African monsoon and the importance of the Congo Air Boundary. Quaternary Science Reviews, 30, pp.798–807.

46. Tieszen, L.L., 1991. Natural variations in the carbon isotope values of plants: Implications for archaeology, ecology, and paleoecology. Journal of Archaeological Science, 18, pp.227–248.

47. Tyson, P.D. & Preston-Whyte, R.A., 2000. The Weather and Climate of Southern Africa Second edi. A. Attwell, ed., South Africa: Oxford University Press.

48. Valsecchi, V., Chase, B.M., Slingsby, J.A., Carr, A.S., Quick, L., Meadows, M.E., Cheddadi, R. & Reimer, P.J., 2013. A high resolution 15,600-year pollen and microcharcoal record from the Cederberg Mountains, South Africa. Palaeogeography, Palaeoclimatology, Palaeoecology, 387, pp.6–16. Available at: http://dx.doi.org/10.1016/j.palaeo.2013.07.009.

49. Vimeux, F., Masson, V., Delaygue, G., Jouzel, J., Petit, J.R. & Stievenard, M., 2001. A 420,000 year deuterium excess record from East Antarctica: the origin of precipitation at Vostok. Journal of Geophysical Research, 106, pp.31863–31873.

50. Vogts, A., Moossen, H., Rommerskirchen, F. & Rullkötter, J., 2009. Distribution patterns and stable carbon isotopic composition of alkanes and alkan-1-ols from

plant waxes of African rain forest and savanna C_3 species. Organic Geochemistry, 40, pp.1037–1054.

51. Weldeab, S., Stuut, J.-B.W., Schneider, R. & Siebel, W., 2013. Holocene climate variability in the winter rainfall zone of South Africa. Climate of the Past, 9, pp.2347–2364.

52. West, A.G., February, E.C. & Bowen, G.J., 2014. Spatial analysis of hydrogen and oxygen stable isotopes ("isoscapes") in ground water and tap water across South Africa. Journal of Geochemical Exploration, 145, pp.213–222.

53. Zhao, X., Dupont, L., Meadows, M.E. & Wefer, G., 2015. Pollen distribution in the marine surface sediments of the mudbelt along the west coast of South Africa. Quaternary International, pp.1–13.

54. Zhao, X., Dupont, L.M., Schefuß, E., Meadows, M.E., Hahn, A. & Wefer, G. Holocene vegetation and climate variability between in the winter and summer rainfall zones of South Africa. The Holocene. In press.

Part IV

Glycerol dialkyl glycerol tetraethers (GDGTs)

Thus far, the previous two chapters have chosen to focus on two elements of palaeoclimatology: the reconstruction of climate through use of multiple proxies; and the identification of environmental controls on lipid biomarkers. In this chapter, a third aspect is addressed, namely, the comparison between two proxies that define a single variable.

This chapter outlines the use of glycerol dialkyl glycerol tetraethers (GDGT) as a proxy for SST, productivity and terrestrial input in the BUS. SSTs derived from GeoB8323-2 GDGT concentrations (SST_{TEX86}) are used here for comparative purposes in conjunction with alkenone-derived SST ($SST_{UK'37}$), and were not used in the reconstruction of south-west African palaeoclimate (ie. Chapters 1 and 2). However, they are included in this thesis to record data for possible future research, to consider what climatic variation can be inferred from their results, and to review the effectiveness of this relatively new proxy method within the BUS.

The chapter is made up of the following four sections. The introduction briefly summarizes the literature and outlines the objectives, after which the methodology is described. The results and discussion document and explore the data within the broader context of what has already been established through Chapters 1 and 2. The chapter concludes by highlighting the most significant points and evaluating the potential use of GDGTs in the region of St. Helena Bay.

1 Introduction

1.1 What are GDGTs?

GDGTs are membrane lipids that are synthesized by Archaea, which are ubiquitous in marine, lacustrine and soil environments (Hopmans et al. 2004; Smith et al. 2012). The structure of the tetraethers depends on the environment in which they are produced; the primary difference between those synthesized by terrestrial Archaea[3], and those produced in a marine setting, is the fact that land-based GDGTs (I-III) have a branched structure, whereas marine- and lacustrine-derived GDGTs are isoprenoid (0-4) (Figure 13) (Hopmans et al. 2004; Weijers et al. 2009)[4]. In addition, marine Crenarchaeota biosynthesize discernable amounts of a crenarchaeol regioisomer (4') (Weijers et al. 2006; Schouten et al. 2007).

The composition of membrane lipids varies according to the temperature of the environment in which they are produced (Schouten et al. 2007; Kim et al. 2008; Lee et al. 2008). The distribution of the isoprenoid GDGTs produced by Crenarchaea varies depending on growth temperature (Weijers et al. 2006). This variation is used to calculate SST using the TEX_{86} ratio, which can be calibrated to give exact values in degrees Celsius. The original index and calibration of TEX_{86} was established by Schouten et al. (2002). This thesis uses the modified versions presented in Kim et al. (2010), which better reflect sub-polar and polar ocean temperatures.

Branched GDGTs (I-III) and the isoprenoid crenarchaeol (4) can be used to establish a ratio in which the relative fluvial input of terrestrial organic matter (TOM) within a marine system is calculated (Weijers et al. 2006). This ratio is called the Branched vs Isoprenoid Tetraether (BIT) index (Hopmans et al. 2004).

The use of GDGTs in palaeoenvironmental reconstructions is a relatively new concept,

[3]Archaea: a taxonomical kingdom of microorganisms, found across diverse environments (DeLong & Pace 2001).

[4]Isoprenoid GDGTs are not exclusively marine: they do occur in terrestrial soils, but only in non-influential amounts. They can therefore be ignored in calculations (Hopmans et al. 2004; Weijers et al. 2006; Weijers et al. 2009)

which has emerged through the rapid advancement of high performance lipid chromatography (HPLC) (Schouten et al. 2002; Hopmans et al. 2004). The recognition of a new SST proxy is an important development, due to the pressing need to resolve palaeoceanic features in order to reconstruct climatic conditions during the late Quaternary. The $U^{K'}_{37}$ method is well-established, but may not be suitable in all environments, particularly where the abundance of haptophyte algae is low. Despite several limitations, TEX_{86} could fill these gaps, and serve to increase robustness of SST data. These limitations include:

1. The production of Crenarcaea below the mixed layer in the water column, and not just the surface layer. TEX_{86} may therefore not be an accurate representation of SST, but rather a reflection of an integrated temperature of the water column (Kim et al. 2008; Lee et al. 2008).

2. Possible seasonal bias of SST_{TEX86}, depending on when productivity is highest (Hollis et al. 2012; Lopes dos Sanches 2012).

3. Influence of terrestrially-derived GDGTs on the marine system (Lopes dos Sanches 2012).

The first two issues have been identified as relevant in the case of the BUS, where a cold bias has been recorded by SST_{TEX86} in comparison to satellite-measured mean annual SST (Lee et al. 2008). The third issue is not relevant in regions of high marine productivity (Lopes dos Sanches 2012).

The BIT index is unhindered by the above limitations due to branched GDGTs being terrestrially derived, and is a useful indicator of TOM (Hopmans et al. 2004). A low BIT has consistently been measured in areas with strong upwelling, because the ratio of terrestrial/oceanic productivity is low. On the other hand, regions comprising completely soil-derived organic matter have measured BIT values of >0.9 (Weijers et al. 2009).

1.2 Aims and objectives

GDGT analysis was conducted with the following research question in mind:

1. How do TEX_{86} SST results compare with those obtained via the $U^{K'}_{37}$ method? What accounts for differences between the records and what does this mean for further GDGT studies in the St. Helena Bay region?

To answer this question, three objectives were developed:

i. Compare Benguela Current SSTs via two different proxies ($SST_{UK'37}$ and SST_{TEX86}).

ii. Produce a record of terrestrial/oceanic productivity in southwest Africa during the late Holocene.

iii. Assess the viability of employing GDGTs in the BUS.

2 Methods

The preparation of samples for GDGT analysis followed the same standard procedure as described in Chapters 2 and 3. Neutral fractions of samples (n = 37) yielded polar extracts along with the alkane and ketone fractions (used in compound isotope and GC-FID analysis respectively). The polar extracts were dried, then redissolved in n-hexane: isopropanol (99:1) to bring them to a concentration of $2\mu g/\mu l$. Samples were analysed using high performance liquid chromatography/atmospheric pressure chemical ionization-mass spectrometry (HPLC/APCI-MS), which was carried out on an Agilent 1200 series HPLC system coupled with an Agilent 6120 MSD.

GDGTs were separated by a Prevail Cyano column and were identified using positive-ion APCI-MS. Single-ion monitoring (SIM) mode was used, which determines the concentration of specific (M+H)+ ions, with a dwell time of 67 ms per ion. The ten identified ions include m/z 1302 (GDGT 0), 1300 (GDGT 1), 1298 (GDGT 2), 1296 (GDGT 3), 1292 (GDGT 4), 1292 (GDGT 4' - crenarcheol regio-isomer), 1050 (GDGT III), 1036 (GDGT II), 1022 (GDGT I) and 744 (C_{46} standard). Concentrations of GDGTs were

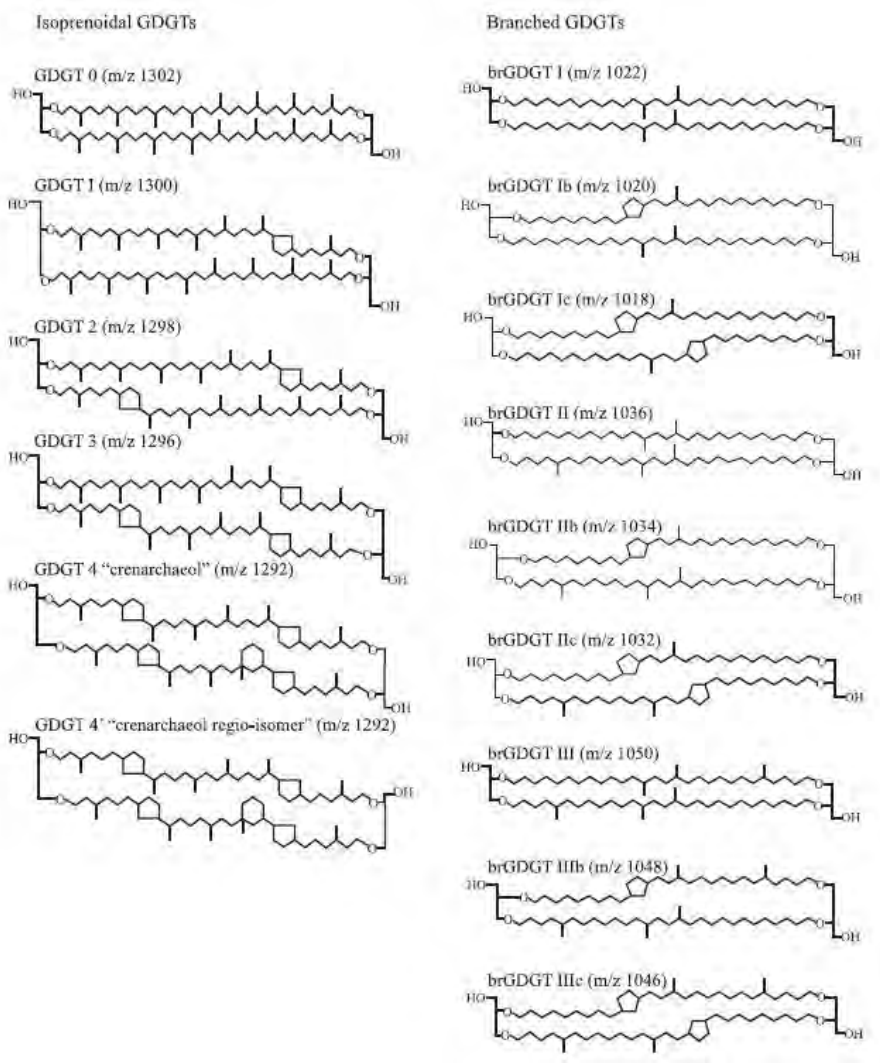

Figure 13: Structure of individual GDGTs (Castañeda & Schouten, 2011). m/z = mass to charge ratio.

quantified by integrating sample peak areas and comparing them to the C_{46} standard concentration that had been added prior to extraction via the ASE 200 (1μl/sample).[5]

The TEX_{86} index and SST calibration (°C) were calculated using the formulae established by Kim et al. (2010).

$$TEX_{86} = \frac{log[GDGT\,2 + GDGT\,3 + GDGT\,4]'}{GDGT\,1 + GDGT\,2 + GDGT\,3 + GDGT\,4'}$$

$$SST = (68.4 * [TEX_{86}] + 38.6\ (r^2 = 0.86)$$

The BIT index was calculated using the equation from Hopmans et al. (2004):

$$BIT = \frac{[I + II + III]}{[I + II + III + 4]}$$

For SST_{TEX86}, two samples were run in duplicate to establish a mean standard deviation. This deviation (equivalent to 0.19°C) was then applied to the sample set. For the BIT index, two samples were run in triplicate. This equated to a deviation of 0.018, which was used for the sample set.

A comparison of BIT values with $SST_{UK'37}$ was determined statistically using Pearson's Product-moment Correlation coefficient, run in R software. The coefficient measures the strength of the relationship between two variables. A correlation coefficient was determined for the full record, as well as for the 1050-year period where the graphs appeared most synchronized, from the earlier half of the record, ca. 50 BCE to 1000 CE.

[5]See Chapter 2.2 for details on ASE extraction.

3 Results and discussion

3.1 BIT

BIT values are consistently low (maximum 0.24) throughout the record (Figure 14). This is characteristic of upwelling areas, where production of Crenarcheota is high relative to fluvially transported terrestrial organic input. A steady decrease in BIT occurred from ca. 500 CE to 1050 CE, after which the low values (<0.17) persisted over the next 700 years, before increasing slightly during the last 2 centuries.

The index, as has been mentioned, is primarily used to gauge changes in the fluvial transport of terrestrial organic matter (Dupont et al. 2013). Following this logic, the mid-record decrease seen in Figure 14a indicates a reduction in terrestrial organic matter being supplied to the system, which contradicts the rainfall increase at ca. 750 CE described in Chapters 2 and 3. However, there are two possible explanations for this. Firstly, an increase in rainfall may not necessarily indicate an increase in organic matter being transported to the ocean, as heavy precipitation could lead to erosion of less organically-rich soils, with less plant material being transported to the ocean (Dupont et al. 2013).

The second factor is related to changes in the concentration of Crenarchaeota, and has not been extensively researched due to the novelty of the proxy. Although it is not yet clear to what extent changes in marine productivity affect the ratio, several studies attribute a significant proportion of variation to the changing production of Crenarchaeota (Fietz et al. 2011; Grauel et al. 2013; Dupont et al. 2013). The results of the Pearson test support this assessment, as it revealed a significant correlation between BIT and alkenone-derived SST at the 95% level both for the entire record and the abbreviated record (see Table 1). This indicates that marine productivity, with its strong inverse relationship to SST, may exert a larger influence on BIT than has been yet supposed, and requires further study. This relationship appears to break down somewhat after 1050 CE, possibly as a result of terrestrial input from the Olifants increasing due to higher

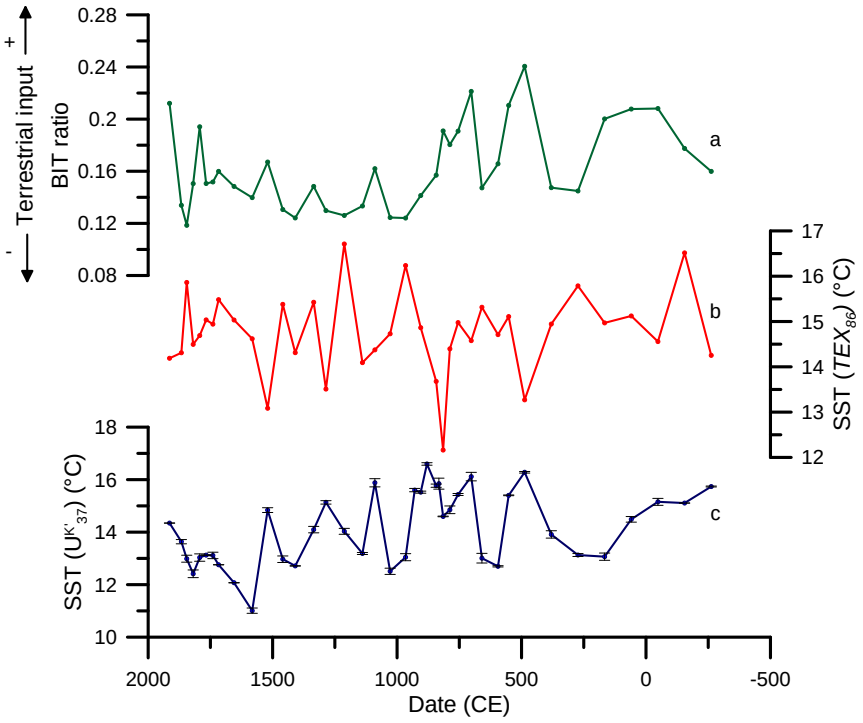

Figure 14: GeoB8323-2 variation in (a) Branched vs Isoprenoid Tetraether index; (b) Benguela Current SST_{TEX86}; and (c) Benguela Current $SST_{UK'37}$.

rainfall as suggested by the grain size, carbon isotope and Fe/K analyses.

3.2 Comparison between TEX_{86} and UK'37

Although the GDGT- and alkenone-derived records have similar mean values (14.9°C and 14.1°C respectively), the datasets reveal divergent trends in variation (Figures 14b and 14c). Whereas $SST_{UK'37}$ decreased markedly over time, there is no such clear trend in SST_{TEX86}. The temperature ranges of the two datasets are different (ca. 5°C and 6.5°C in $SST_{UK'37}$ and SST_{TEX86} respectively), and maximum SST_{TEX86} was recorded at ca. 1200 CE, when $SST_{UK'37}$ was in decline. Likewise, minimum SST_{TEX86} occurred at ca. 800 CE, when $SST_{UK'37}$ was relatively high.

There are several factors which may account for the differences between proxy results.

Table 1: Results from Pearson's product-moment test, showing linear correlation between BIT and $SST_{UK'37}$. N is the sample number of pairs; df is the degrees of freedom (N-2); $p<0.001$ and $p<0.01$; and r is the correlation coefficient (0 to 1). A correlation value between 0.4 and 0.59 is considered moderate, and a value between 0.6 and 0.79 is considered strong (Evans, 1996).

Pearson's Product Moment Test	
Full depth	
N	37
df	35
p	0.00066
r	0.53445
Abridged (50 BCE to 1050 CE)	
N	17
df	15
p	0.00992
r	0.60605

The predominant argument against the use of TEX_{86} is the tendency for Crenarchaeol to be produced below the surface in the thermocline layer (Kim et al. 2008; Lee et al. 2008; Ho et al. 2011). Consequently, environmental temperatures recorded by Archaea may not accurately represent SST, but rather an integrated temperature signal from the water column. This is particularly pertinent in the BUS, where nutrient-rich waters upwell from below the thermocline layer near the coast. A second factor possibly influencing SST_{TEX86} is the complex below-surface current movements and recirculation of water in the region of St. Helena Bay, near our study site.

3.3 TEX_{86} as a proxy for productivity

The large discrepancy between SST_{TEX86} and $SST_{UK'37}$ does not disqualify the use of TEX_{86} as a proxy in the BUS. A study by Shaari et al. (2013) has suggested that the issue of production at depth can be resolved by interpreting TEX_{86} as a potential indicator of upwelling intensity. The alkenone-derived SST signal is subtracted from the GDGT-derived SST record, calculating the difference between the TEX_{86} and $U^{K'}{}_{37}$ temperature values. Upwelling strength is then represented by the variable ΔT in the following equation:

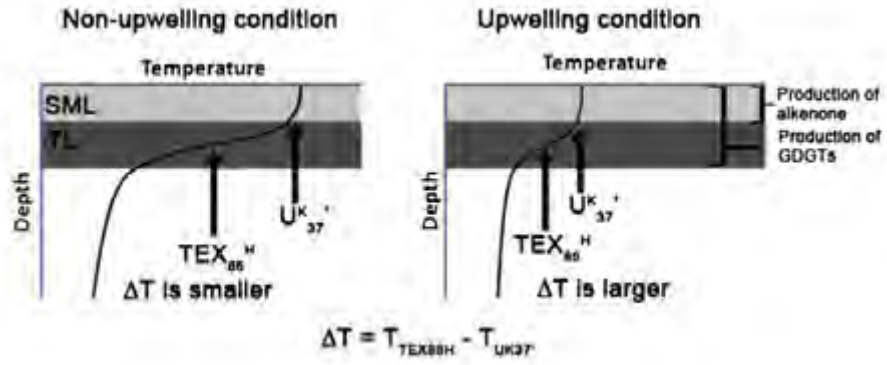

Figure 15: Conceptual model from *Shaari et al. (2013)* showing changes in ΔT during upwelling and non-upwelling conditions. SML = Surface Mixed Layer; TL = Thermocline Layer.

$$\triangle T = T_{TEX86} - T_{UK'37}$$

A large ΔT indicates stronger upwelling; a lower ΔT suggests weaker upwelling. Shaari et al. (2013) demonstrate this mechanism through a simple diagram (Figure 15). At times of intense upwelling, the temperature gradient between the surface layer (measured by TEX_{86} and $U^{K'}{}_{37}$) and thermocline layer (measured by TEX_{86} only) is smaller than during times of weak upwelling, resulting in a more positive ΔT value. The reverse is true during times of relaxation/weak upwelling (Shaari et al. 2013).

Applying this index to GeoB8323-2 data, variations in BUS upwelling strength (ΔT) were determined (Figure 16). Results showed periods of weak upwelling at 500 CE and 700 – 900 CE, and periods of strong upwelling at 150 – 400 CE, 950 – 1050 CE and 1600 – 1850 CE. When considered alongside the conclusions drawn in Chapter 2, ΔT augments the palaeoclimatic record of the BUS region. Periods of stronger upwelling occurred during the latter part of the record (ca. 950 CE - present), which complements the decreasing SST trend previously observed with $SST_{UK'37}$. Between 1600 and 1900 CE, cool surface temperatures appear to have been synchronous with very intense upwelling, whereas the

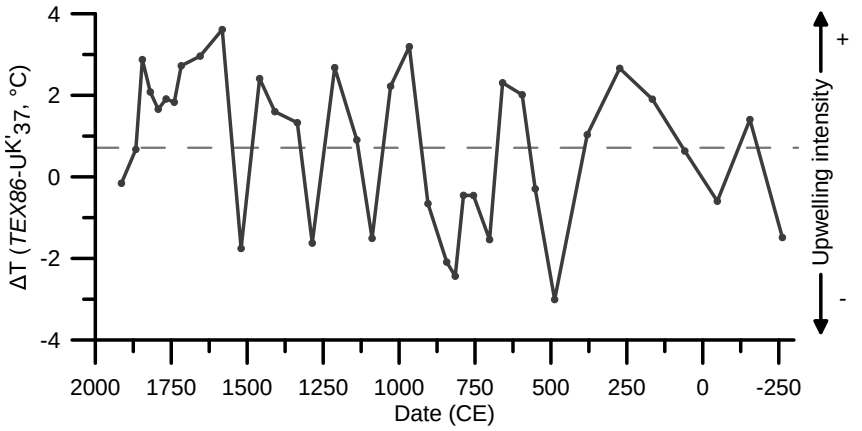

Figure 16: Variation in upwelling intensity (ΔT) over time. The dashed line represents ΔTmean. Values above this are characteristic of stronger-than-average upwelling; values below this are characteristic of weaker-than-average upwelling.

period between 700 and 900 CE consisted of weak upwelling and higher SSTs. During this warm period, the westerly flow appears to have been in a more southerly position (Granger et al. in review), allowing for increased Agulhas leakage to enter the BUS, which significantly warmed the waters and prevented intense upwelling (see Chapter 2).

However, it remains unclear to what degree the local south-easterly winds that drive upwelling influenced the system during the late Holocene, since a more southerly position in the austral westerly winds would also allow for an increased transport of ocean water away from the continent. Evidence exhibited in Chapter 2, however, advocates that variation in Atlantic water temperatures feeding into the BUS, and the varying amount of Agulhas leakage entering the system, were strong enough to overlay the local signal of south-easterly winds for much of the record.

4 Conclusions

This study determines TEX_{86} to be an unreliable indicator of SST within the region of St. Helena Bay, due to large production of Archaea below the surface mixed layer, which

results in a depth-integrated signal. A comparison between $SST_{UK'37}$ and SST_{TEX86} yielded no identifiable similarities. However, despite the challenges of using TEX_{86} in the BUS, the record, when used in conjunction with $U^{K'}{}_{37}$, produces an index that is a possible indicator of Benguela productivity. The recognition of this relatively new palaeoceanographic index will hopefully be more fully explored in the future.

With regards to the BIT ratio, variation demonstrates a meaningful correlation to alkenone-derived SSTs, particularly during the earlier half of the record. This study therefore supports the hypothesis that BIT can be significantly affected both by the supply of marine Crenarchaeota and branched GDGTs (Fietz et al. 2011; Dupont et al. 2013; Grauel et al. 2013). However, this also leads to the conclusion that in the region of St. Helena Bay, BIT does not reliably estimate variation in terrestrial organic matter.

The combination of results from $SST_{UK'37}$, SST_{TEX86} and BIT depict a trend towards cooler, more productive waters in the BUS during the last few hundred years. Apart from yielding new information about the regional oceanic conditions during the late Holocene, this chapter has clearly demonstrated the advantages of using multi-proxy records, and illustrated the need to identify and develop new proxies to increase our understanding of palaeoclimatic conditions. It thereby significantly adds to this thesis, through the raising of topical questions within the broader framework of palaeoenvironmental methodology. This chapter serves as a reminder of the importance of both observing proxy limitations as well as choosing suitable methods of analysis within a specific environment.

Part V

Conclusion

1 Introduction

Through the application of multiple inorganic and organic proxies, this study revealed new information surrounding palaeoenvironmental conditions in southwest Africa, thus contributing to the late Holocene climate history of the region. Datasets generated from marine core GeoB8323-2 are useful not only in identifying past relationships between climate variables, but may also provide valuable insight into present and future climate interconnections. This chapter summarizes the most important findings of this study; reviews and answers the initial research questions outlined in Chapter 1; and concludes by evaluating the success of the study and commenting upon future research opportunities.

2 Summary of proxies

GeoB8323-2 was used to reconstruct climate in southwest Africa over the last 2,250 years, using the following proxy methods: $U^{K'}{}_{37}$, grain size, elemental ratio Fe/K, compound specific carbon ($\delta^{13}C$) and deuterium (δD) isotope ratios, and glycerol dialkyl glycerol tetraethers (GDGTs) (which includes TEX_{86} and the BIT index). Reconstructions of palaeoclimatic conditions are thought to reflect climate variation in the Olifants catchment region (ie. the WRZ).

Provided in this section are tables summarizing proxy methods and their interpretations (Tables 2 and 3). These tables act as general references; they are added here to supplement the conclusions drawn in this chapter and are greatly simplified.

Production of a high-resolution sea surface temperature (SST) record via the $U^{K'}{}_{37}$ proxy was a vital component of this thesis, since SST is known to be coupled to low-level atmospheric conditions. In addition to the SST dataset, end-member (grain size) mod-

Table 2: Simplified summary of methods used in this study and their proxy interpretations.

Symbol	Proxy	Unit	Interpretation (simplified)	
EM1	coarse grain size	*unit ratio*	+	increase in WRZ rainfall
			-	decrease in WRZ rainfall
Fe/K	weathering intensity	*unit ratio*	+	increase in WRZ rainfall
			-	decrease in WRZ rainfall
δ**D**	hydrogen isotope	*‰*	+	increase in (coastal) rainfall
			-	increase in aridity; increase in mountain/ high-altitude rainfall
δ^{13}**C**	carbon isotope	*‰*	+	increase in aridity
			-	increase in rainfall
$\mathbf{U^{K'}_{37}}$	sea surface temperature	ºC	+	warm
			-	cool
BIT	Terrestrial organic matter (TOM)	*unit ratio*	+	increase in TOM
			-	increase in marine productivity
$\boldsymbol{TEX_{86}}$	sea surface temperature	ºC	+	warm
			-	cool
Δ**T**	Upwelling intensity	*ºC*	+	increase in upwelling strength
			-	decrease in upwelling strength

Table 3: Simplified summary of findings by individual proxies.

Proxy	**50 BCE - 250 CE**	**50 - 700 CE**	**700 - 1300 CE**	**1300 - 1900 CE**
EM1	dry with moderate variability	dry	variable (wet and dry events)	wet
Fe/K	dry	dry	increasingly wet	wet
δ**D**	dry	increasingly dry	variable (wet and dry events)	increasingly wet *esp.*1800 - 1900 CE
δ^{13}**C**	dry	dry	increasingly wet	increasingly wet
WUE[6]	dominant	dominant	weak	moderate
$\mathbf{U^{K'}_{37}}$	warm	increasingly warm	increasingly cool	cool
BIT	increasing TOM	variable	decreasing TOM; increasing marine productivity	high marine productivity; increasing TOM
$\boldsymbol{TEX_{86}}$	warm	increasingly cool	high variability	high variability
Δ**T**	low productivity	low productivity	increasing productivity	high productivity

elling and compound-specific carbon isotope analyses were performed to assess temporal changes in rainfall, with $\delta^{13}C$ also providing insight into changing vegetation patterns in the region. Furthermore, this study concluded that compound-specific hydrogen isotope analysis in this case is primarily forced through spatial changes in precipitation - a process known as the continental or altitude effect - rather than reflecting changes in the actual amount of rainfall. Finally, the elemental ratio of Fe/K is used to highlight changes in chemical weathering intensity, which is strongly associated with shifts in humidity. The known climate epochs, the MCA and LIA, overlap the temporal scale of this thesis, and the regional response of southwest Africa to these climate shifts, traditionally associated with Northern Hemispheric changes, was assessed.

Because of issues regarding temperature-integration of the water column and high marine productivity, proxies deriving from marine and terrestrial GDGT concentration ratios (TEX_{86} and BIT) were not suited to identifying trends in palaeoenvironmental conditions, but were instead used:

i. As a comparative index to $U^{K'}_{37}$, where the resulting differences in SST values were discussed with reference to external forcing mechanisms;

ii. To demonstrate the importance of new proxy development;

iii. To assess the viability of these novel proxy methods within the BUS.

3 Review of aims and objectives

The following section summarizes the results of this thesis in the context of the initial research questions outlined in Chapter 1.

What trends and variability have been observed in SST over the past 2,250 years?

A steady long-term decreasing trend in SST (-0.1°C / 100 years) was identified to have occurred in this region during the late Holocene. Temperatures during the last 500 years

have been cool relative to the remainder of the record, with the lowest SSTs occurring at ca. 1550 CE, coinciding with the middle of the LIA. After this period of relatively cool temperatures during the LIA, SST reached a satellite-acquired modern-day equivalent at ca. 1900 CE, which increases confidence in the palaeothermometer.

The variability in SST during the period under review (250 BCE to 1900 CE) was surprisingly high, with a larger SST range (~6°) than has been previously identified in the BUS (~2°C, Farmer et al. 2005), leading to the conclusion that the core's southerly position, combined with the complex topography of the embayment and the resulting recirculation of waters, produces an amplified signal. Site specificity within the BUS is also a likely cause for the lack of cohesion seen between these results and those of Leduc et al. (2010) and Farmer et al. (2005).

What are the drivers of change in isotopic composition in the WRZ, and what inferences can be made regarding terrestrial changes in hydrology and vegetation type during this time?

Grain size data combined with pollen data (Zhao et al. 2015) revealed a strong WRZ signal in GeoB8323-2, as opposed to sediment being largely derived and transported from the larger Orange River to the north. Hydrological changes are therefore taken as a reflection of vegetative and hydrological changes within the Olifants catchment area (situated in the WRZ). The increasing ratio of Olifants to Orange River sediment over time suggests an increasingly wet WRZ, with peak rainfall at ca. 1800 CE, an implication reinforced by the Fe/K and δ^{13}C records. The inorganic ratio reflected a late Holocene movement towards more humid conditions, and δ^{13}C, rather than reflecting shifts in vegetation type, was dominated by the effect of moisture changes within a region of minimal vegetative change (Ehleringer & Cooper 1988; Scott & Vogel 2000). The strong resilience of South African West Coast vegetation, with a particular emphasis on the multitude of species endemic to the Fynbos biome, has been previously acknowledged, and the results of this study concur with the view of high Fynbos resistance to external changes. A recent shift

towards depleted δ^{13}C values are manifested as a result of increased moisture availability, or a decrease in water use efficiency.

Core-top, vegetation-corrected δD values removed possible effects of plant physiology and evapotranspiration. Variation in leaf wax δD was found to be representative of changes in water use efficiency, rainout distance and altitude, rather than precipitation amount (Gat 1996; Sachse et al. 2012; Collins et al. 2013). Water use efficiency as a mechanism of change was most evident in the period between 250 BCE and 600 CE, whereas the relative strengths of the altitude and distance gradients were more prominent in more recent times. A preliminary model of δD change assumes the signal recorded by GeoB8323-2 to be mainly representative of coastal regions within the catchment area. During times of aridity, full rainout occurred over the coastal plains of southwest Africa, resulting in a more depleted isotopic signal, whereas during more mesic periods, rainfall was present over the neighbouring Cederberg Mountains, producing a coastal-recorded signal enriched in δD. The last 600 years (ca. 1350 – 1950 CE) have exhibited a trend towards increasing moisture availability (the observed enrichment trend in δD being interpreted as a consequence decreasing water use efficiency), and rainout over a larger region within the WRZ. This study's interpretation of the fluctuations between arid and humid climate conditions in the Cederberg accords well with several previous records while contrasting with others. This serves to highlight the importance of accounting for site specificity and the need for higher resolution data when interpreting mountain records.

However, although δ^{13}C and δD produced records of spatial and temporal hydrological variability, it is important to recognize the need for multiproxy studies when making use of isotope analysis in this region. Without the supplementary GeoB8323-2 records of SST, grain size and Fe/K, as well as the data provided by previous palaeoclimatic studies of the WRZ, it would have been extremely difficult to identify the root causes of δ^{13}C and δD variation. Additionally, southwest Africa contains an abundance of CAM succulents, whose effects on palaeoenvironmental records are not yet fully understood (Boom et al. 2014). Caution is therefore advocated when interpreting isolated isotope signals recovered

from this region, and suggests further research is necessary before a more robust estimate can be made.

How do the marine and terrestrial proxy records compare with one another, and how do they compare with what is known about regional and global climate dynamics during this time? Are the conclusions drawn from this study of southwest Africa applicable at a wider geographical scale?

I: The driving mechanism of southwest African climate dynamics

Cooling SSTs appear to be in general associated with increasingly wet WRZ conditions. This contradicts the modern-day seasonal ocean-atmosphere system, where cold SSTs are correlated to arid climates. The relationship observed in the GeoB8323-2 record is likely the result of long-term, large-scale forcing and is not primarily induced by local winds. Dominance of climate-drivers vary through time, with large-scale forcing mechanisms oscillating between periods of relative strength and weakness. Although the primary cause of long-term change in the Northern Hemisphere is variation in orbital forcing/insolation, Southern Hemisphere dynamics are heavily influenced by the westerlies (Chevalier and Chase 2015). Even within the relatively short time-scale recorded in this study, alternating dominance of drivers is apparent. Shifts in Benguela SST in particular demonstrate how a decreasing westerly wind presence could have a noticeable effect on the local region of southwest Africa, as it allows for more local upwelling-driving winds to substantially influence the system.

Variation in both insolation and the austral westerlies is closely tied to the amount of moisture entering a system, upon which environmental changes are dependent. This is consistent with conclusions drawn from several WRZ studies, which postulate that aridity is a major driving factor in palaeoclimatological records (Chase and Thomas 2006; Chase et al. 2015, 2013). Changes in the intensity and latitudinal position of the austral westerly winds can affect both oceanic and terrestrial environments. This study supports the argument that a northward migration, or intensification of westerly winds, is linked to an

increase in sea-ice (Lamy et al. 2004; Bard and Rickaby 2009), which would act to decrease the temperatures of source waters moving into the BUS, decreasing its SST. Compounding this, a diminishing influx of warm Agulhas leakage into the system (precipitated through the wind-induced constriction of the ocean corridor south of South Africa that allows transport between the eastern and western boundary currents), further cools BUS surface waters. With regards to terrestrial hydrology, the same change in the austral westerly wind belt would bring storm systems into closer proximity to South Africa. This would increase the amount of rainfall falling over the country and accelerate chemical weathering. An inverse relationship is thus established between SST and humidity.

The last 100 – 200 years experienced more pronounced variability than occurred during the remainder of the period. The effects of human impact, as has been mentioned, cannot be ruled out, since inhabitants started to heavily impact the environment at around this time (Stager et al. 2012). However, the recent shift towards a warmer, drier climate during this time (as shown by increasing SST and decreasing Olifants River transport) is also suggestive of a southwards retreat of the austral westerlies. Consequently, the results documented here likely reflect a combination of climatic and human changes.

II: Large-scale climate dynamics

A contributing factor to the hypothesis of hemispheric-scale forcing is the fact that similar climate changes have been identified in other Southern Hemispheric palaeoenvironmental records during the past millennium. Benguela SST variation, as revealed by GeoB8323-2, and mid-latitude Peru Current SSTs both display a decreasing trend over the last 1000 years. In addition, the south-west coasts of South Africa and Chile both reveal an increase in chemical weathering and humidity that is roughly synchronous with this cooling of surface waters, as well as with glacial advancement (Kaiser et al. 2008; Lamy et al. 2002).

East of South Africa, a record from the south-central coast of Australia has also documented a shift towards wetter conditions in a region sensitive to frontal systems

borne on the westerlies, during the last 1000 years (Marx et al. 2011). However, the zonal symmetry that appears throughout these Southern Hemisphere records may not necessarily be a permanent feature. This study proposes that, at least in the region of St. Helena Bay, local-scale forcing was dominant prior to 250 CE. This was perhaps due in part to the position of the westerlies being too far south to exert significant force on environmental conditions in the BUS and WRZ.

In addition to zonal symmetry, the records from GeoB8323-2 are suggestive of a possible relationship between Benguela SST in St. Helena Bay and Northern Hemisphere air temperatures (Moberg et al. 2005). The intriguing correlation between these two variables (shown in Chapter 2: Figure 7) is not explored in detail here, but may be of interest in future research, as it demonstrates the pressing need to develop and improve palaeoclimatic records of the Southern Hemisphere. Increasing the robustness of data from southwest Africa - a key region where local variation within the WRZ has been shown to reflect, to some extent, large-scale climatic changes - would assist in this development.

How do TEX_{86} SST results compare with those obtained via the $U^{K'}_{37}$ method? What accounts for differences in the records and what does this mean for further GDGT studies in the St. Helena Bay region?

In addition to the three initial research questions surrounding the BUS and southwest Africa, a further research question was addressed. The TEX_{86} proxy index was, in this case, not interpreted within the context of reconstructing southwest African palaeoclimate, but instead focused on posing questions with regards to the development of new proxy methods, and the reliability of these proxies in different locations.

No identifiable relationship was found between the two SST proxies. Issues regarding the reliability of TEX_{86} are most likely related to the tendency of Archaea to live within the mixed layer of the water column and not only the surface (Kim et al. 2008; Lee et al. 2008). TEX_{86} has also been documented as recording a seasonal, not mean annual, temperature depending on when growth was most abundant (Hollis et al. 2012). On the

grounds of these issues, TEX_{86} is not considered to be a reliable sea surface palaeothermometer in this southerly section of the BUS. This study does not advocate the use of TEX_{86} within the St. Helena Bay region as an SST proxy until a clear distinction can be made between sub-surface and surface oceanic production, as well as between seasonal and annual mean ocean temperatures. However, TEX_{86} has proven to be advantageous when used in conjunction with $U^{K'}_{37}$, and may be able to determine changes in ocean productivity below the surface mixed layer.

The Branched vs Isoprenoid Tetraether (BIT) index, also derived from GDGT concentrations, varies similarly to the alkenone-derived SST record, particularly from ca. 50 BCE - 1050 CE. The strong positive relationship between the two during this time indicates that marine productivity may strongly affect the index, more so than has been previously recognized. As GDGTs become more widely-used in palaeoclimatic research, the linkages between SST and BIT will become more firmly established.

4 Challenges and constraints

The challenges of core hiatuses and age model discrepancies that were encountered in this study are common to the majority of palaeoenvironmental research, namely the differences in the input data and model software used to generate model ages. To account for some of this difference, dates were rounded to the nearest half century, and despite the hiatus in GeoB8323-2 limiting the period available for analysis, above this, sediment is near-continuous. Furthermore, interpretations of GeoB8323-2 are constrained by their limited ability to infer climatic conditions and variation in the WRZ at a catchment-level, upon which account significant changes at individual locations within this region cannot be separated from the integrated signal.

Unanticipated systemic challenges developed as a result of high productivity in the BUS. The presence of Archaea within the mixed layer water column had a significant effect on the SST value derived from GDGTs, to such a degree that there was no visible correlation between the two SST proxies. In addition, the productivity at depth also

prevented reliable measurement of GDGT-derived terrestrial organic matter. However, these limitations served to emphasize the importance of multiproxy records, as well as the ingenuity of developing alternative uses within a single proxy. Indeed, the comparison between the two SST proxy methods highlighted both the need for continual development of new proxies, and the value of method consideration with regards to site specificity.

5 Final remarks

The multiproxy study presented here has illustrated the ways in which southern African palaeoenvironmental research is increasingly overcoming the stigma associated with the negative impacts of aridity on palaeo-records. Terrestrial, lacustrine and marine datasets are being used to significant effect within the region. The paucity of late Holocene studies, however, remains an issue that has yet to be fully addressed.

The benefits of late Holocene reconstructions are unique within the palaeoclimate record in that, in comparison to Quaternary timescales, they document relatively recent conditions, which can be used in near-future prediction models. This rationale, combined with the complex ocean-atmosphere dynamics observed between southwest Africa and the greater Southern Hemisphere, demonstrates the need for further high-resolution palaeoenvironmental studies of the WRZ. For this purpose, the recovery and analysis of additional west coast mudbelt sediment could be facilitated, although more detailed examination of existing, underutilized, core material may also reveal significant results, as has been proven here.

This study has achieved its aims and has contributed to a deeper understanding of the palaeoenvironmental record of the late Holocene in southwest Africa. Critical analysis and interpretation of the new high-resolution record of variation in the BUS and, by extension, the WRZ, contributes materially to the literature on late Holocene South African climate dynamics.

Part VI

References

1. Araguas-Araguas, L., Froehlich, K. & Rozanski, K., 2000. Deuterium and oxygen-18 isotope composition of precipitation and atmospheric moisture. Hydrological Processes, 14, pp.1341–1355.

2. Barbante, C., Barnola, J.-M., Becagli, S., Beer, J., Bigler, M., Boutron, C., Blunier, T., Castellano, E., Cattani, O., Dahl-Jensen, D., 2006. One-to-one coupling of glacial climate variability in Greenland and Antarctica. Nature, 444, pp.195–198. Available at: http://www.nature.com/doifinder/10.1038/nature05301.

3. Bard, E. & Rickaby, R.E.M., 2009. Migration of the subtropical front as a modulator of glacial climate. Nature, 460, pp.380–383. Available at: http://dx.doi.org/10.1038/nature08189.

4. Barker, S., Diz, P., Vautravers, M.J., Pike, J., Knorr, G., Hall, I.R. & Broecker, W.S., 2009. Interhemispheric Atlantic seesaw response during the last deglaciation. Nature, 457, pp.1097–1102. Available at: http://www.nature.com/doifinder/10.1038/nature07770.

5. Bloemsma, M.R., Zabel, M., Stuut, J.-B.W., Tjallingii, R., Collins, J.A. & Weltje, G.J., 2012. Modelling the joint variability of grain size and chemical composition in sediments. Sedimentary Geology, 280, pp.135–148. Available at: http://dx.doi.org/10.1016/j.sedgeo.2012.04.009.

6. Blome, M.W., Cohen, A.S., Tryon, C.A., Brooks, A.S. & Russell, J., 2012. The environmental context for the origins of modern human diversity: A synthesis of regional variability in African climate 150,000-30,000 years ago. Journal of Human Evolution, 62, pp.563–592. Available at: http://dx.doi.org/10.1016/j.jhevol.2012.01.011.

7. Boom, A., Carr, A.S., Chase, B.M., Grimes, H.L. & Meadows, M.E., 2014. Organic Geochemistry Leaf wax n -alkanes and δ^{13}C values of CAM plants from arid southwest Africa. Organic Geochemistry, 67, pp.99–102.

8. Carr, A.S., Thomas, D.S.G., Bateman, M.D., Meadows, M.E. & Chase, B.M., 2006. Late Quaternary palaeoenvironments of the winter-rainfall zone of southern Africa: Palynological and sedimentological evidence from the Agulhas Plain. Palaeogeography, Palaeoclimatology, Palaeoecology, 239, pp.147–165.

9. Carr, A.S., Boom, A., Grimes, H.L., Chase, B.M., Meadows, M.E. & Harris, A., 2014. Leaf wax n-alkane distributions in arid zone South African flora: Environmental controls, chemotaxonomy and palaeoecological implications. Organic Geochemistry, 67, pp.72–84.

10. Carr, A.S., Boom, A., Chase, B.M., Meadows, M.E. & Grimes, H.L., 2015. Holocene sea level and environmental change on the west coast of South Africa: evidence from plant biomarkers, stable isotopes and pollen. Journal of Paleolimnology, 53, pp.415–432.

11. Castañeda, I.S. & Schouten, S., 2011. A review of molecular organic proxies for examining modern and ancient lacustrine environments. Quaternary Science Reviews, 30, pp.2851–2891. Available at: http://dx.doi.org/10.1016/j.quascirev.2011.07.009.

12. Cerling, T., Wang, Y. & Quade, J., 1993. Expansion of C_4 ecosystems as an indicator of global ecological change in the late Miocene. Letters to Nature, 361, pp.344–345.

13. Chase, B.M. & Thomas, D.S.G., 2006. Late Quaternary dune accumulation along the western margin of South Africa: distinguishing forcing mechanisms through the analysis of migratory dune forms. Earth and Planetary Science Letters, 251, pp.318–333.

14. Chase, B.M. & Meadows, M.E., 2007. Late Quaternary dynamics of southern Africa's winter rainfall zone. Earth-Science Reviews, 84, pp.103–138.

15. Chase, B.M., Meadows, M.E., Scott, L., Thomas, D.S.G., Marais, E., Sealy, J. & Reimer, P.J., 2009. A record of rapid Holocene climate change preserved in hyrax middens from southwestern Africa. Geology, 37, pp.703–706. Available at: http://geology.gsapubs.org/cgi/doi/10.1130/G30053A.1.

16. Chase, B.M., Boom, A., Carr, A.S., Meadows, M.E. & Reimer, P.J., 2013. Holocene climate change in southernmost South Africa: rock hyrax middens record shifts in the southern westerlies. Quaternary Science Reviews, 82, pp.199–205.

17. Chase, B.M., Boom, A., Carr, A.S., Carré, M., Chevalier, M., Meadows, M.E., Pedro, J.B., Stager, J.C. & Reimer, P.J., 2015. Evolving southwest African response to abrupt deglacial North Atlantic climate change events. Quaternary Science Reviews, 121, pp.132–136.

18. Chase, B.M., Lim, S., Chevalier, M., Boom, A., Carr, A.S., Meadows, M.E. & Reimer, P.J., 2015. Influence of tropical easterlies in southern Africa's winter rainfall zone during the Holocene. Quaternary Science Reviews, 107, pp.138–148.

19. Chevalier, M. & Chase, B.M., 2015. Southeast African records reveal a coherent shift from high- to low-latitude forcing mechanisms along the east African margin across last glacial–interglacial transition. Quaternary Science Reviews, 125, pp.117–130.

20. Collins, J.A., Schefuß, E., Mulitza, S., Prange, M., Werner, M., Tharammal, T., Paul, A. & Wefer, G., 2013. Estimating the hydrogen isotopic composition of past precipitation using leaf-waxes from western Africa. Quaternary Science Reviews, 65, pp.88–101.

21. Collins, J.A., Schefuß, E., Govin, A., Mulitza, S. & Tiedemann, R., 2014. Insolation and glacial–interglacial control on southwestern African hydroclimate over the past

140 000 years. Earth and Planetary Science Letters, 398, pp.1–10. Available at: http://dx.doi.org/10.1016/j.epsl.2014.04.034.

22. Collister, J.W., Rieley, G., Stern, B., Eglinton, G. & Fry, B., 1994. Compound - specific δ^{13}C analyses of leaf lipids from plants with differing carbon dioxide metabolisms. Organic Geochemistry, 21, pp.619–627.

23. Compton, J., 2001. Holocene sea-level fluctuations inferred from the evolution of depositional environments of the southern Langebaan Lagoon salt marsh, South Africa. The Holocene, 11, pp.395–405. Available at: http://hol.sagepub.com/cgi/doi/10.1191/095968301678302832.

24. Cowling, R.M., Cartwright, C.R., Parkington, J.E. & Allsopp, J.C., 1999. Fossil wood charcoal assemblages from Elands Bay Cave, South Africa: implications for Late Quaternary vegetation and climates in the winter-rainfall fynbos biome. Journal of Biogeography, 26, pp.367–378. Available at: http://doi.wiley.com/10.1046/j.1365-2699.1999.00275.x.

25. Cowling, R.M., Richardson, D.M. & Pierce, S.M., 2004. Vegetation of Southern Africa, Cambridge University Press.

26. Dansgaard, W., 1964. Stable isotopes in precipitation. Tellus 16, pp. 436-468.

27. DeLong, E.F. & Pace, N.R., 2001. Environmental diversity of bacteria and archaea. Systematic biology, 50, pp.470–478.

28. Demarcq, H., Barlow, R.G. & Shillington, F.A., 2003. Climatology and Variability of Sea Surface Temperature and Surface Chlorophyll in the Benguela and Agulhas Ecosystems As Observed by Satellite Imagery. African Journal of Marine Science, 25, pp.363–372. Available at: http://www.tandfonline.com/doi/abs/10.2989/18142320309504022.

29. Desmet, P.G. & Cowling, R.M., 1999. Biodiversity, habitat and range-size aspects of a flora from a winter-rainfall desert in north-western Namaqualand, South Africa.

Plant Ecology, 142, pp.23–33. Available at: http://dx.doi.org/10.1023/A:1009814109891.

30. Dewar, G., Reimer, P.J., Sealy, J. & Woodborne, S., 2012. Late-Holocene marine radiocarbon reservoir correction (ΔR) for the west coast of South Africa. The Holocene, 22, pp.1481–1489. Available at: http://hol.sagepub.com/cgi/doi/10.1177/0959683612449755.

31. Dufois, F. & Rouault, M. 2012. Sea surface temperature in False Bay (South Africa): Towards a better understanding of its seasonal and inter-annual variability. Continental Shelf Research. 43, pp. 24-35.

32. Dupont, L.M., Rommerskirchen, F., Mollenhauer, G. & Schefuß, E., 2013. Miocene to Pliocene changes in South African hydrology and vegetation in relation to the expansion of C_4 plants. Earth and Planetary Science Letters, 375, pp.408–417.

33. Eckardt, F.D. & Kuring, N., 2005. SeaWiFS identifies dust sources in the Namib Desert. International Journal of Remote Sensing, 26, pp.4159–4167.

34. Eckardt, F.D., Livingstone, I., Seely, M. & Von Holdt, J., 2013. The surface geology and geomorphology around Gobabeb, Namib desert, Namibia. Geografiska Annaler, Series A: Physical Geography, 95, pp.271–284.

35. Ehleringer, J.R. & Cooper, T.A., 1988. Correlations between carbon isotope ratio and microhabitat in desert plants, Oecologia, 76, pp.562–566.

36. Ehleringer, J.R. & Dawson, T.E., 1992. Water uptake by plants: perspectives from stable isotope composition. Plant, Cell and Environment, 15, pp.1073–1082.

37. Etourneau, J., Collins, L.G., Willmott, V., Kim, J.H., Barbara, L., Leventer, A., Schouten, S., Sinninghe Damsté, J.., Bianchini, A., Klein, V., Crosta, X. & Massé, G., 2013. Holocene climate variations in the western Antarctic Peninsula: Evidence for sea ice extent predominantly controlled by changes in insolation and ENSO variability. Climate of the Past, 9, pp.1431–1446.

38. Evans, J.D., 1996. Straightforward statistics for the behavioral sciences. Pacific Grove, CA: Brooks/Cole Publishing.

39. Farmer, E.C., deMenocal, P.B. & Marchitto, T.M., 2005. Holocene and deglacial ocean temperature variability in the Benguela upwelling region: Implications for low-latitude atmospheric circulation. Paleoceanography, 20, pp.1–16.

40. Farquhar, G.D., Ehleringer, J.R. & Hubick, K.T., 1989. Carbon isotope discrimination and photosynthesis. Annual Review of Plant Physiology and Plant Molecular Biology, 40, pp.503–537.

41. Feakins, S.J. & Sessions, A.L., 2010. Controls on the D/H ratios of plant leaf waxes in an arid ecosystem. Geochimica et Cosmochimica Acta, 74, pp.2128–2141.

42. Fietz, S., Martínez-Garcia, A., Huguet, C., Rueda, G. & Rosell-Melé, A., 2011. Constraints in the application of the Branched and Isoprenoid Tetraether index as a terrestrial input proxy. Journal of Geophysical Research: Oceans, 116, pp.1–9.

43. Flanagan, L.B. & Ehleringer, J.R., 1991. Effects of Mild Water Stress and Diurnal Changes in Temperature and Humidity on the Stable Oxygen and Hydrogen Isotopic Composition of Leaf Water in *Cornus stolonifera* L. The Journal of Plant Physiology, 97, pp.298–305.

44. Fletcher, M.-S. & Moreno, P.I., 2012. Have the Southern Westerlies changed in a zonally symmetric manner over the last 14,000 years? A hemisphere-wide take on a controversial problem. Quaternary International, 253, pp.32–46.

45. Fogel, M.L. & Cifuentes, L. A., 1993. Isotope Fractionation during Primary Production. Organic Geochemistry, 1993, pp.73–98.

46. Garzanti, E., Vermeesch, P., Andò, S., Lustrino, M., Padoan, M. & Vezzoli, G., 2014. Ultra-long distance littoral transport of Orange sand and provenance of the Skeleton Coast Erg (Namibia). Marine Geology, 357, pp.25–36.

47. Garzoli, S.L., Richardson, P.L., Rae, C.M.D., Fratantoni, D.M., Gofii, G.J. & Roubicek, A.J., 1999. Three Agulhas Rings observed during the Benguela Current Experiment. Journal of Geophysical Research, 104, pp.20971–20985.

48. Gat, J.R., 1996. Oxygen and Hydrogen Isotopes in the Hydrologic Cycle. Annual Review of Earth and Planetary Sciences, 24, pp.225–262. Available at: http://www.annualreviews.org/doi/abs/10.1146/a
nnurev.earth.24.1.225.

49. Gersonde, R., Crosta, X., Abelmann, A. & Armand, L., 2005. Sea-surface temperature and sea ice distribution of the Southern Ocean at the EPILOG Last Glacial Maximum - a circum-Antarctic view based on siliceous microfossil records. Quaternary Science Reviews, 24, pp.869–896.

50. Gingele, F.X., 1996. Holocene climatic optimum in southwest Africa - Evidence from the marine clay mineral record. Palaeogeography Palaeoclimatology Palaeoecology, 122, pp.77–87.

51. Gonfiantini, R., Roche, M.A., Olivry, J.C., Fontes, J.C. & Zuppi, G.M., 2001. The altitude effect on the isotopic composition of tropical rains. Chemical Geology, 181, pp.147–167.

52. Govin, A., Holzwarth, U., Heslop, D., Ford Keeling, L., Zabel, M., Mulitza, S., Collins, J.A. & Chiessi, C.M., 2012. Distribution of major elements in Atlantic surface sediments (36°N-49°S): Imprint of terrigenous input and continental weathering. Geochemistry, Geophysics, Geosystems, 13, pp.1–23.

53. Granger, R., Meadows, M.E., Hahn, A., Stuut, J.-B.W., Hermann, N., Zabel, M. & Schefuß, E., 2016. Coupling between late Holocene sea-surface temperature and terrestrial hydrology in southwestern Africa. Quaternary Science Reviews. In review.

54. Grauel, A.-L., Leider, A., Goudeau, M.-L.S., Müller, I.A., Bernasconi, S.M., Hinrichs, K.-U., de Lange, G.J., Zonneveld, K.A.F. & Versteegh, G.J.M., 2013. What do SST proxies really tell us? A high-resolution multiproxy (U^{K}_{37}, TEX^{H}_{86} and foraminifera $\delta^{18}O$) study in the Gulf of Taranto, central Mediterranean Sea. Quaternary Science Reviews, 73, pp.115–131.

55. Gray, C.E.D., Meadows, M.E., Lee-Thorp, J.A. & Rogers, J., 2000. Characterising the Namaqualand Mudbelt of Southern Africa: Chronology, Palynology and Palaeoenvironments. South African Geographical Journal, 82, pp.137–142. Available at: http://www.tandfonline.com/doi/abs/10.1080/03736245.2000.9713705.

56. Haberzettl, T., Corbella, H., Fey, M., Janssen, S., Lucke, A., Mayr, C., Ohlendorf, C., Schabitz, F., Schleser, G.H., Wille, M., Wulf, S. & Zolitschka, B., 2007. Lateglacial and Holocene wet-dry cycles in southern Patagonia: chronology, sedimentology and geochemistry of a lacustrine record from Laguna Potrok Aike, Argentina. The Holocene, 17, pp.297–310.

57. Hahn, A., Compton, J., Meyer-Jacob, C., Kirsten, K., Lucassen, F., Mayo, M., Schefuß, E. & Zabel, M., Holocene paleoclimatic record from the South African Namaqualand mudbelt: A source to sink approach. Quaternary International, 2015, pp.1–15.

58. Hardman-Mountford, N.J., Richardson, A.J., Agenbag, J.J., Hagen, E., Nykjaer, L., Shillington, F.A. & Villacastin, C., 2003. Ocean climate of the South East Atlantic observed from satellite data and wind models. Progress in Oceanography, 59, pp.181–221.

59. Herbert, C.T. & Compton, J., 2007. Geochronology of Holocene sediments on the western margin of South Africa. South African Journal of Geology, 110, pp.327–338. Available at: http://sajg.geoscienceworld.org/cgi/doi/10.2113/gssajg.110.2-3.327.

60. Hijmans, R.J., Cameron, S. & Parra, J., 2004. WorldClim, Version 1.4 (release 3). A square kilometer resolution of global terrestrial surface climate.

61. Ho, S.L., Yamamoto, M., Mollenhauer, G. & Minagawa, M., 2011. Core top TEX_{86} values in the south and equatorial Pacific. Organic Geochemistry, 42, pp.94–99.

62. Hollis, C.J., Taylor, K.W.R., Handley, L., Pancost, R.D., Huber, M., Creech, J.B., Hines, B.R., Crouch, E.M., Morgans, H.E.G., Crampton, J.S., Gibbs, S., Pearson, P.N. & Zachos, J.C., 2012. Early Paleogene temperature history of the Southwest Pacific Ocean: Reconciling proxies and models. Earth and Planetary Science Letters, 349-350, pp.53–66.

63. Hopmans, E.C., Weijers, J.W.H., Schefuß, E., Herfort, L., Sinninghe Damsté, J.. & Schouten, S., 2004. A novel proxy for terrestrial organic matter in sediments based on branched and isoprenoid tetraether lipids. Earth and Planetary Science Letters, 224, pp.107–116.

64. Hutchings, L., van der Lingen, C.D., Shannon, L.J., Crawford, R.J.M., Verheye, H.M.S., Bartholomae, C.H., van der Plas, A.K., Louw, D., Kreiner, A., Ostrowski, M., Fidel, Q., Barlow, R.G., Lamont, T., Coetzee, J., Shillington, F.A., Veitch, J.A., Currie, J.C. & Monteiro, P.M.S., 2009. The Benguela Current: An ecosystem of four components. Progress in Oceanography, 83, pp.15–32. Available at: http://dx.doi.org/10.1016/j.pocean.2009.07.046.

65. Hutchings, L., Jarre, A., Lamont, T., van den Berg, M. & Kirkman, S.P., 2012. St Helena Bay (Southern Benguela) then and now: muted climate signals, large human impact. African Journal of Marine Science, 34, pp.559–583. Available at: http://www.tandfonline.com/doi/abs/10.2989/1814232X.2012.689672.

66. Jansen, J.H.., Van Der Gaast, S.J., Koster, B. & Vaars, A.J., 1998. CORTEX, a shipboard XRF-scanner for element analyses in split sediment cores. Marine Geology, 151, pp.143–153.

67. Jury, M & Courtney, S. 1995. Climatic determinants of Benguela SST variability. Continental Shelf Research. 15, pp. 1339-1354.

68. Kaiser, J., Schefuß, E., Lamy, F., Mohtadi, M. & Hebbeln, D., 2008. Glacial to Holocene changes in sea surface temperature and coastal vegetation in north central Chile: high versus low latitude forcing. Quaternary Science Reviews, 27, pp.2064–2075.

69. Kido, Y., Koshikawa, T. & Tada, R., 2006. Rapid and quantitative major element analysis method for wet fine-grained sediments using an XRF microscanner. Marine Geology, 229, pp.209–225.

70. Kim, J.H., Schouten, S., Hopmans, E.C., Donner, B. & Sinninghe Damsté, J.., 2008. Global sediment core-top calibration of the TEX_{86} paleothermometer in the ocean. Geochimica et Cosmochimica Acta, 72, pp.1154–1173.

71. Kim, J.H., van der Meer, J., Schouten, S., Helmke, P., Willmott, V., Sangiorgi, F., Koç, N., Hopmans, E.C. & Damsté, J.S.S., 2010. New indices and calibrations derived from the distribution of crenarchaeal isoprenoid tetraether lipids: Implications for past sea surface temperature reconstructions. Geochimica et Cosmochimica Acta, 74, pp.4639–4654.

72. Kolattukudy, P.E., 1976. Chemistry and biochemistry of natural waxes. Elsevier Scientific Pub. Co.Amsterdam, New York.

73. Lamont, T., Hutchings, L., van den Berg, M., Goschen, W.S. & Barlow, R.G., 2015. Hydrographic variability in the St. Helena Bay region of the southern Benguela ecosystem. Journal of Geophysical Research: Oceans, 120, pp.2920-2944.

74. Lamy, F., Hebbeln, D. & Wefer, G., 1999. High-resolution marine record of climatic change in mid-latitude Chile during the last 28,000 years based on terrigenous sediment parameters. Quaternary Research, 51, pp.83–93.

75. Lamy, F., Hebbeln, D., Röhl, U. & Wefer, G., 2001. Holocene rainfall variability in southern Chile: a marine record of latitudinal shifts of the Southern Westerlies. Earth and Planetary Science Letters, 185, pp.369–382.

76. Lamy, F., Rühlemann, C., Hebbeln, D. & Wefer, G., 2002. High- and low-latitude climate control on the position of the southern Peru-Chile Current during the Holocene. Paleoceanography, 17, pp.16–1 – 16–10.

77. Lamy, F., Kaiser, J., Ninnemann, U., Hebbeln, D., Arz, H.W. & Stoner, J., 2004. Antarctic timing of surface water changes off Chile and Patagonian ice sheet response. Science, 304, pp.1959–1962.

78. Lamy, F., Kilian, R., Arz, H.W., Francois, J.-P., Kaiser, J., Prange, M. & Steinke, T., 2010. Holocene changes in the position and intensity of the southern westerly wind belt. Nature Geoscience, 3, pp.695–699. Available at: http://dx.doi.org/10.1038/ngeo959.

79. Leaney, F.W., Osmond, C.B., Allison, G.B. & Ziegler, H., 1985. Hydrogen-isotope composition of leaf water in C_3 and C_4 plants - its relationship to the hydrogen isotope composition of dry matter. Planta, 164, pp.215–220.

80. Leduc, G., Herbert, C.T., Blanz, T., Martinez, P. & Schneider, R., 2010. Contrasting evolution of sea surface temperature in the Benguela upwelling system under natural and anthropogenic climate forcings. Geophysical Research Letters, 37, pp.1–5. Available at: http://doi.wiley.com/10.1029/2010GL044353.

81. Lee, K.E., Kim, J.H., Wilke, I., Helmke, P. & Schouten, S., 2008. A study of the alkenone, TEX_{86} , and planktonic foraminifera in the Benguela Upwelling System: Implications for past sea surface temperature estimates. Geochemistry, Geophysics, Geosystems, 9, 1-19.

82. Levin, N.E., Zipser, E.J. & Cerling, T.E., 2009. Isotopic composition of waters from Ethiopia and Kenya: Insights into moisture sources for eastern Africa. Journal of Geophysical Research, 114, pp. 1-13. Available at: http://doi.wiley.com/10.1029/2009JD012166.

83. Locarini, R.A., Mishonov, A. V., Antonov, J.I., Boyer, T.P., Garcia, H.E., Baranova, O.K., Zweng, M.M., Paver, C.R., Reagan, J.R., Johnson, D.R., Hamilton, M. & Seidov, D., 2013. World Ocean Atlas 2013, Volume 1: Temperature S. Levitus & A. Mishanov, eds., NOAA Atlas NESDIS 73.

84. Lopes dos Sanches, R.A., 2012. Reconstruction of late Quaternary marine and terrestrial environmental conditions of Northwest Africa and Southeast Australia: A multiple organic proxy study using marine sediments. Dissertation. Universität Utrecht. pp.1-146.

85. Mann, M., Zhang, Z., Rutherford, S., Bradley, R., Hughed, M., Shindell, D., Ammann, C., Faluvegi, G. & Ni, F., 2009. Global Signatures and Dynamical Origins of the Little Ice Age and Medieval Climate Anomaly. Science, 326, pp.1256–1260.

86. Marx, S.K., Kamber, B.S., McGowan, H.A. & Denholm, J., 2011. Holocene dust deposition rates in Australia's Murray-Darling Basin record the interplay between aridity and the position of the mid-latitude westerlies. Quaternary Science Reviews, 30, pp.3290–3305.

87. Mayewski, P.A., Rohling, E.E., Curt Stager, J., Karlén, W., Maasch, K.A., David Meeker, L., Meyerson, E.A., Gasse, F., van Kreveld, S., Holmgren, K., Lee-Thorp, J., Rosqvist, G., Rack, F., Staubwasser, M., Schneider, R. & Steig, E.J., 2004. Holocene climate variability. Quaternary Research, 62, pp.243–255.

88. McGregor, H. V, Dima, M., Fischer, H.W. & Mulitza, S., 2007. Rapid 20th-century increase in coastal upwelling off northwest Africa. Science, 315, pp.637–9.

89. Meadows, M.E. & Sugden, J.M., 1993. The late quaternary palaeoecology of a floristic kingdom: the southwestern Cape South Africa. Palaeogeography, Palaeoclimatology, Palaeoecology, 101, pp.271–281.

90. Meadows, M.E., Baxter, A.J. & Parkington, J., 1996. Late Holocene environments at Verlorenvlei, Western Cape Province, South Africa. Quaternary International,

33, pp.81–95.

91. Meadows, M.E. & Baxter, A.J., 2001. Holocene vegetation history and palaeoenvironments at Klaarfontein Springs, Western Cape, South Africa. The Holocene, 11, pp.699–706. Available at: http://hol.sagepub.com/cgi/doi/10.1191/09596830195726.

92. Meadows, M.E., Rogers, J., Lee-Thorp, J. A., Bateman, M.D. & Dingle, R. V., 2002. Holocene geochronology of a continental-shelf mudbelt off southwestern Africa. The Holocene, 12, pp.59–67.

93. Meadows, M.E., Chase, B.M. & Seliane, M., 2010. Holocene palaeoenvironments of the Cederberg and Swartruggens mountains, Western Cape, South Africa: Pollen and stable isotope evidence from hyrax dung middens. Journal of Arid Environments, 74, pp.786–793. Available at: http://dx.doi.org/10.1016/j.jaridenv.2009.04.020.

94. Moberg, A., Sonechkin, D., Holmgren, K., Datsenko, N. & Karlén, W., 2005. Highly variable Northern Hemisphere temperatures reconstructed from low- and high-resolution proxy data. Letters to Nature, 433, pp.613–617.

95. Mooney, H.A., 1972. The Carbon Balance of Plants. Annual Review of Ecology and Systematics, 3, pp.315–346.

96. Moros, M., De Deckker, P., Jansen, E., Perner, K. & Telford, R.J., 2009. Holocene climate variability in the Southern Ocean recorded in a deep-sea sediment core off South Australia. Quaternary Science Reviews, 28, pp.1932–1940. Available at: http://dx.doi.org/10.1016/j.quascirev.2009.04.007.

97. Mucina, L. & Rutherford, M.C., 2006. Nama-Karoo biome. The vegetation of South Africa, Lesotho and Swaziland., (JANUARY), pp.326–330.

98. Mucina, L. & Rutherford, M.C., 2006. The Vegetation of South Africa, Lesotho and Swaziland. Strelitzia, South African National Biodiversity Institute, Pretoria.

99. Müller, P.J., Kirst, G., Ruhland, G., Storch, I. Von & Rosell-Mele, A., 1998. Calibration of the alkenone paleotemperature index $U^{K'}_{37}$ based on core-tops from the eastern South Atlantic and the global ocean (60° N-60°S). Geochemica et Cosmochimica Acta, 62, pp.1757–1772.

100. Nelson, G. & Hutchings, L., 1983. The Benguela upwelling area. Progress in Oceanography, 12, pp.333–356.

101. Nicholson, S.E.E., Nash, D.J.J., Chase, B.M., Grab, S.W., Shanahan, T.M.M., Verschuren, D., Asrat, A., Lezine, A.-M. & Umer, M., 2013. Temperature variability over Africa during the last 2000 years. The Holocene, 23, pp.1085–1094. Available at: http://hol.sagepub.com/cgi/doi/10.1177/0959683613483618.

102. Njitchoua, R., Sigha-Nkamdjou, L., Dever, L., Marlin, C., Sighomnou, D. & Nia, P., 1999. Variations of the stable isotopic compositions of rainfall events from the Cameroon rain forest, Central Africa. Journal of Hydrology, 223, pp.17–26.

103. O'Leary, M.H., 1988. Carbon Isotopes in Photosynthesis. BioScience, 38, pp.328–336.

104. Pancost, R.D. & Boot, C.S., 2004. The palaeoclimatic utility of terrestrial biomarkers in marine sediments. Marine Chemistry, 92, pp.239–261.

105. Pillans, B. & Naish, T., 2004. Defining the Quaternary. Quaternary Science Reviews, 23, pp.2271–2282.

106. Pitcher, G.C. & Nelson, G., 2006. Characteristics of the surface boundary layer important to the development of red tide on the southern Namaqua shelf of the Benguela upwelling system. Limnology and Oceanography, 51, pp.2660–2674.

107. Pitcher, G.C., Figueiras, F.G., Hickeyd, B.M. & Moita, M.T., 2010. The physical oceanography of upwelling systems and the development of harmful algal blooms. Progress in Oceanography, 85, pp.5–32.

108. Prahl, F.G. & Wakeham, S.G., 1987. Calibration of unsaturation patterns in long-chain ketone compositions for palaeotemperature assessment. Nature, 330, pp.367–369.

109. Prospero, J.M., Ginoux, P., Torres, O., Nicholson, S.E.E. & Gill, T.E., 2002. Environmental characterization of global sources of atmospheric soil dust identified with the NIMBUS 7 Total Ozone Mapping Spectrometer (TOMS) absorbing aerosol product. Reviews of Geophysics, 40, pp.1–31.

110. Quick, L., Chase, B.M., Meadows, M.E., Scott, L. & Reimer, P.J., 2011. A 19.5kyr vegetation history from the central Cederberg Mountains, South Africa: Palynological evidence from rock hyrax middens. Palaeogeography, Palaeoclimatology, Palaeoecology, 309, pp.253–270. Available at: http://dx.doi.org/10.1016/j.palaeo.2011.06.008.

111. Reimer, P.J., 2013. IntCal13 and Marine13 Radiocarbon Age Calibration Curves 0–50,000 Years cal BP. Radiocarbon, 55, pp.1869–1887.

112. Renssen, H., Goosse, H., Fichefet, T., Masson-Delmotte, V. & Koç, N., 2005. Holocene climate evolution in the high-latitude Southern Hemisphere simulated by a coupled atmosphere–sea ice–ocean–vegetation model. The Holocene, 15, pp.951–964.

113. Rogers, J. & Rau, A., 2006. Surficial sediments of the wave-dominated Orange River Delta and the adjacent continental margin off south-western Africa. African Journal of Marine Science, 28, pp.511–524.

114. Rommerskirchen, F., Eglinton, G., Dupont, L., Güntner, U., Wenzel, C. & Rullkötter, J., 2003. A north to south transect of Holocene southeast Atlantic continental margin sediments: Relationship between aerosol transport and compound-specific δ^{13}C land plant biomarker and pollen records. Geochemistry, Geophysics, Geosystems, 4, pp.1–29. Available at: http://doi.wiley.com/10.1029/2003GC000541.

115. Rouault, M., Pohl, B. & Penven, P., 2010. Coastal oceanic climate change and variability from 1982 to 2009 around South Africa. African Journal of Marine Science, 32, pp.237–246.

116. de Ruijter, W.P.M., Biastoch, A., Drijfhout, S.S., Lutjeharms, J.R.E., Matano, R.P., Pichevin, T., van Leeuwen, P.J. & Weijer, W., 1999. Indian-Atlantic interocean exchange: Dynamics, estimation and impact. Journal of Geophysical Research, 104, pp.20885–20910.

117. Rutherford, M.C. & Westfall, R.H., 1994. Biomes of southern Africa: an objective categorization, ed 2. Memoirs of the Botanical Survey of South Africa, 63, pp.1-94.

118. Sachse, D., Billault, I., Bowen, G.J., Chikaraishi, Y., Dawson, T.E., Feakins, S.J., Freeman, K.H., Magill, C.R., McInerney, F. A., van der Meer, M.T.J., Polissar, P., Robins, R.J., Sachs, J.P., Schmidt, H.-L., Sessions, A.L., White, J.W.C., West, J.B. & Kahmen, A., 2012. Molecular paleohydrology: interpreting the hydrogen-isotopic composition of lipid biomarkers from photosynthesizing organisms. Annual Review of Earth and Planetary Sciences, 40, pp.221–249. Available at: http://www.annualreviews.org/doi/abs/10.1146/annurev-earth-042711-105535.

119. Schefuß, E., Versteegh, G.J.., Jansen, J.H.. & Sinninghe Damsté, J.., 2004. Lipid biomarkers as major source and preservation indicators in SE Atlantic surface sediments. Deep Sea Research Part I: Oceanographic Research Papers, 51, pp.1199–1228.

120. Schouten, M., Ruijter, W., van Leeuwen, P.J. & Lutjeharms, J.R.E., 2000. Translation , decay and splitting of Agulhas rings in the southeastern Atlantic Ocean. Journal of Geophysical Research, 105, pp.21913–21925.

121. Schouten, S., Hopmans, E.C. & M, E.S., 2002. Distributional variations in marine crenarchaeotal membrane lipids: a new tool for reconstructing ancient sea water temperatures? Earth and Planetary Science Letters, 204, pp.265–274.

122. Schouten, S., Huguet, C., Hopmans, E.C., Kienhuis, M.V.M. & Damsté, J.S.S., 2007. Analytical Methodology for TEX_{86} Paleothermometry by High-Performance Liquid Chromatography/Atmospheric Pressure Chemical Ionization-Mass Spectrometry. The Journal of Analytical Chemistry, 79, pp.2940–2944.

123. Scott, L. & Vogel, J.C., 2000. Evidence for environmental conditions during the last 20 000 years in Southern Africa from ^{13}C in fossil hyrax dung. Global and Planetary Change, 26, pp.363–365.

124. Scott, L., Marais, E. & Brook, G.A., 2004. Fossil hyrax dung and evidence of Late Pleistocene and Holocene vegetation types in the Namib Desert. Journal of Quaternary Science, 19, pp.829–832. Available at: http://doi.wiley.com/10.1002/jqs.870.

125. Scott, L. & Woodborne, S., 2007. Vegetation history inferred from pollen in Late Quaternary faecal deposits (hyraceum) in the Cape winter-rain region and its bearing on past climates in South Africa. Quaternary Science Reviews, 26, pp.941–953.

126. Seibt, U., Rajabi, A., Griffiths, H. & Berry, J. A., 2008. Carbon isotopes and water use efficiency: Sense and sensitivity. Oecologia, 155, pp.441–454.

127. Shaari, H. Bin, Yamamoto, M. & Irino, T., 2013. Enhanced upwelling in the eastern equatorial Pacific at the last five glacial terminations. Palaeogeography, Palaeoclimatology, Palaeoecology, 386, pp.8–15.

128. Shannon, L.V. & Nelson, G., 1996. The Benguela: large scale features and processes and system variability. In G. Wefer et al., eds. The South Atlantica: Present and Past Circulation. Berlin: Springer, pp. 163–210.

129. Shillington, F.A., 1998. The Benguela upwelling system off southwestern Africa. The Sea, 11, pp.583–604.

130. Shindell, D.T. & Schmidt, G.A., 2004. Southern Hemisphere climate response to ozone changes and greenhouse gas increases. Geophysical Research Letters, 31, pp.1–4.

131. Smith, A.B., Sadr, K., Gribble, J. & Yates, R., 1991. Excavations in the south-western Cape, South Africa, and the archaeological identity of prehistoric hunter-gatherers within the last 2000 years. The South African Archaeological Bulletin, 46, pp.71–91.

132. Smith, F.A. & Freeman, K.H., 2006. Influence of physiology and climate on δD of leaf wax n-alkanes from C_3 and C_4 grasses. Geochimica et Cosmochimica Acta, 70, pp.1172–1187.

133. Smith, R.W., Bianchi, T.S. & Li, X., 2012. A re-evaluation of the use of branched GDGTs as terrestrial biomarkers: Implications for the BIT Index. Geochimica et Cosmochimica Acta, 80, pp.14–29.

134. Sokolov, S. & Rintoul, S.R., 2007. On the relationship between fronts of the Antarctic Circumpolar Current and surface chlorophyll concentrations in the Southern Ocean. Journal of Geophysical Research: Oceans, 112, pp.1–17.

135. Stager, J.C., Ryves, D.B., Chase, B.M. & Pausata, F.S.R., 2011. Catastrophic drought in the Afro-Asian monsoon region during Heinrich event 1. Science, 331, pp.1299–302.

136. Stager, J.C., Mayewski, P.A., White, J., Chase, B.M., Neumann, F.H., Meadows, M.E., King, C.D. & Dixon, D.A., 2012. Precipitation variability in the winter rainfall zone of South Africa during the last 1400 yr linked to the austral westerlies. Climate of the Past, 8, pp.877–887.

137. Stewart, R.H., 2009. Introduction To Physical Oceanography, Texas A & M University.

138. Stuut, J.-B.W., Crosta, X., van der Borg, K. & Schneider, R., 2004. Relationship between Antarctic sea ice and southwest African climate during the late Quaternary. Geology, 32, pp. 909-912. Available at: http://geology.gsapubs.org/cgi/doi/10.1130/G20709.1.

139. Tierney, J.E., Russell, J.M., Sinninghe Damsté, J.S., Huang, Y. & Verschuren, D., 2011. Late Quaternary behavior of the East African monsoon and the importance of the Congo Air Boundary. Quaternary Science Reviews, 30, pp.798–807.

140. Tieszen, L.L., 1991. Natural variations in the carbon isotope values of plants: Implications for archaeology, ecology, and paleoecology. Journal of Archaeological Science, 18, pp.227–248.

141. Toggweiler, J.R., Russell, J.L. & Carson, S.R., 2006. Midlatitude westerlies, atmospheric CO_2, and climate change during the ice ages. Paleoceanography, 21, pp.1–15.

142. Tyson, P.D., Garstang, M. & Swap, R., 1996. Large-Scale Recirculation of Air over Southern Africa. Journal of Applied Meteorology, 35, pp.2218–2236.

143. Tyson, P.D., Karlen, W., Holmgren, K. & Heiss, G.A., 2000. The Liitle Ice Age and medieval warming in South Africa. South African Journal of Science, 96, pp. 121-126.

144. Tyson, P.D. & Preston-Whyte, R.A., 2000. The Weather and Climate of Southern Africa Second edi. A. Attwell, ed., South Africa: Oxford University Press.

145. Valsecchi, V., Chase, B.M., Slingsby, J.A., Carr, A.S., Quick, L., Meadows, M.E., Cheddadi, R. & Reimer, P.J., 2013. A high resolution 15,600-year pollen and microcharcoal record from the Cederberg Mountains, South Africa. Palaeogeography, Palaeoclimatology, Palaeoecology, 387, pp.6–16. Available at: http://dx.doi.org/10.1016/j.palaeo.2013.07.009.

146. Vickery, K.J., Eckardt, F.D. & Bryant, R.G., 2013. A sub-basin scale dust plume source frequency inventory for southern Africa, 2005-2008. Geophysical Research Letters, 40, pp.5274–5279.

147. Vimeux, F., Masson, V., Delaygue, G., Jouzel, J., Petit, J.R. & Stievenard, M., 2001. A 420,000 year deuterium excess record from East Antarctica: the origin of

precipitation at Vostok. Journal of Geophysical Research, 106, pp.31863–31873.

148. Vogts, A., Moossen, H., Rommerskirchen, F. & Rullkötter, J., 2009. Distribution patterns and stable carbon isotopic composition of alkanes and alkan-1-ols from plant waxes of African rain forest and savanna C_3 species. Organic Geochemistry, 40, pp.1037–1054.

149. Walker, N.D., 1990. Links Between South African Summer Rainfall and Temperature Variability of the Agulhas and Benguela Current Systems. Journal of Geophysical Research, 95, pp.3297–3319.

150. Wang, Y. V., Larsen, T., Leduc, G., Andersen, N., Blanz, T. & Schneider, R., 2013. What does leaf wax δD from a mixed C_3/C_4 vegetation region tell us? Geochimica et Cosmochimica Acta, 111, pp.128–139.

151. Weeks, S., Barlow, R., Roy, C. & Shillington, F.A., 2006. Remotely sensed variability of temperature and chlorophyll in the southern Benguela: upwelling frequency and phytoplankton response. African Journal of Marine Science, 28, pp.493–509.

152. Weijers, J.W.H., Schouten, S., Spaargaren, O.C. & Sinninghe Damsté, J., 2006. Occurrence and distribution of tetraether membrane lipids in soils: Implications for the use of the TEX_{86} proxy and the BIT index. Organic Geochemistry, 37, pp.1680–1693.

153. Weijers, J.W.H., Schouten, S., Schefuß, E., Schneider, R. & Sinninghe Damsté, J., 2009. Disentangling marine, soil and plant organic carbon contributions to continental margin sediments: A multi-proxy approach in a 20,000 year sediment record from the Congo deep-sea fan. Geochimica et Cosmochimica Acta, 73, pp.119–132.

154. Weldeab, S., Stuut, J.-B.W., Schneider, R. & Siebel, W., 2013. Holocene climate variability in the winter rainfall zone of South Africa. Climate of the Past, 9, pp.2347–2364.

155. Weltje, G.J., 1997. End-Member Modeling of Compositional Data: Numerical-Statistical Algorithms for Solving the Explicit Mixing Problem. Mathematical Geology, 29, pp.503–549.

156. Zalasiewicz, J., Williams, M., Haywood, A. & Ellis, M., 2011. The Anthropocene: a new epoch of geological time? Philosophical transactions of the Royal Society. 369, pp.835–41.

157. Zhao, X., Dupont, L., Meadows, M.E. & Wefer, G., 2015. Pollen distribution in the marine surface sediments of the mudbelt along the west coast of South Africa. Quaternary International, pp.1–13.

158. Zhao, X., Dupont, L.M., Schefuß, E., Meadows, M.E., Hahn, A. & Wefer, G., Holocene vegetation and climate variability between in the winter and summer rainfall zones of South Africa. The Holocene. In press.

159. Ziegler, H., Osmond, C.B., Stichler, W. & Trimborn, P., 1976. Hydrogen Isotope Discrimination in Higher Plants: Correlations with Photosynthetic Pathway and Environment. Planta, 128, pp.85–92.

Part VII

Appendices:

A Age Model

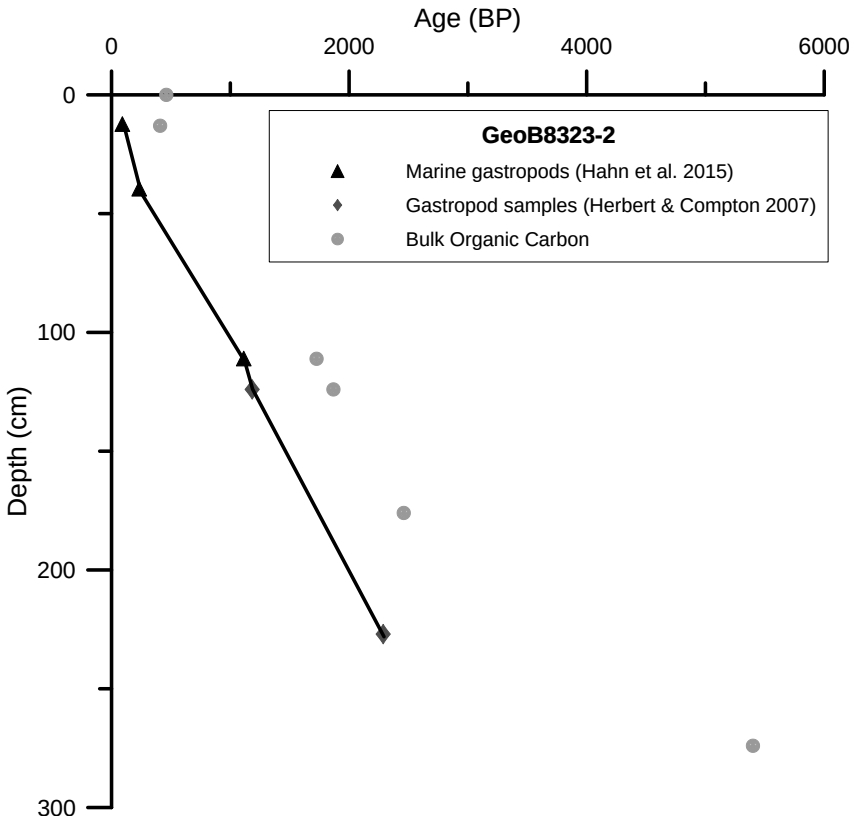

Figure 17: Age model of GeoB8323 using Marine13 calibration curve. ΔR = 146 $\pm$ 85 ^{14}C years (Dewar et al. 2012). The different symbols represent different sample batches and the black line depicts sedimentation rate (based on gastropods). Ages here are in BP (before present), where 0 BP = 1950 CE.

Table 4: Age model for Core GeoB8323-2

Depth (cm)	Date (CE)	Error (years)	*Material*	Source
0	1950			
1	1943			
2	1935			
3	1928			
4	1921			
5	1914			
6	1906			
7	1899			
8	1892			
9	1884			
10	1877			
11	1870			
12	1863			
12.5	1859	**1**	*gastropod*	Hahn et al. (2015)
13	1852			
14	1850			
15	1845			
16	1840			
17	1834			
18	1829			
19	1824			
20	1819			
21	1813			
22	1808			
23	1803			
24	1798			

Table 4: Age model for Core GeoB8323-2

Depth (cm)	Date (CE)	Error (years)	*Material*	Source
25	1793			
26	1787			
27	1782			
28	1777			
29	1772			
30	1767			
31	1761			
32	1756			
33	1751			
34	1746			
35	1740			
36	1735			
37	1730			
38	1725			
39	1720			
39.5	1717	**70**	*gastropod*	Hahn et al. (2015)
40	1705			
41	1692			
42	1680			
43	1668			
44	1655			
45	1643			
46	1631			
47	1619			
48	1606			
49	1594			

Table 4: Age model for Core GeoB8323-2

Depth (cm)	Date (CE)	Error (years)	*Material*	Source
50	1582			
51	1569			
52	1557			
53	1545			
54	1532			
55	1520			
56	1508			
57	1495			
58	1483			
59	1471			
60	1459			
61	1446			
62	1434			
63	1422			
64	1409			
65	1397			
66	1385			
67	1372			
68	1360			
69	1348			
70	1335			
71	1323			
72	1311			
73	1299			
74	1286			
75	1274			

Table 4: Age model for Core GeoB8323-2

Depth (cm)	Date (CE)	Error (years)	*Material*	Source
76	1262			
77	1249			
78	1237			
79	1225			
80	1212			
81	1200			
82	1188			
83	1175			
84	1163			
85	1151			
86	1139			
87	1126			
88	1114			
89	1102			
90	1089			
91	1077			
92	1065			
93	1052			
94	1040			
95	1028			
96	1015			
97	1003			
98	991			
99	979			
100	966			
101	954			

Table 4: Age model for Core GeoB8323-2

Depth (cm)	Date (CE)	Error (years)	*Material*	Source
102	942			
103	929			
104	917			
105	905			
106	892			
107	880			
108	868			
109	855			
110	843			
111	837	**30**	*gastropod*	Hahn et al. (2015)
112	832			
113	826			
114	821			
115	815			
116	810			
117	804			
118	799			
119	793			
120	788			
121	782			
122	777			
123	771			
124	766	**35**	*gastropod*	Herbert and Compton (2007)
125	755			
126	745			
127	734			

Table 4: Age model for Core GeoB8323-2

Depth (cm)	Date (CE)	Error (years)	*Material*	Source
128	723			
129	712			
130	702			
131	691			
132	680			
133	670			
134	659			
135	648			
136	637			
137	627			
138	616			
139	605			
140	595			
141	584			
142	573			
143	563			
144	552			
145	541			
146	530			
147	520			
148	509			
149	498			
150	488			
151	477			
152	466			
153	455			

Table 4: Age model for Core GeoB8323-2

Depth (cm)	Date (CE)	Error (years)	*Material*	Source
154	445			
155	434			
156	423			
157	413			
158	402			
159	391			
160	380			
161	370			
162	359			
163	348			
164	338			
165	327			
166	316			
167	306			
168	295			
169	284			
170	273			
171	263			
172	252			
173	241			
174	231			
175	220			
176	209			
177	198			
178	188			
179	177			

Table 4: Age model for Core GeoB8323-2

Depth (cm)	Date (CE)	Error (years)	*Material*	Source
180	166			
181	156			
182	145			
183	134			
184	123			
185	113			
186	102			
187	91			
188	81			
189	70			
190	59			
191	49			
192	38			
193	27			
194	16			
195	6			
196	-5			
197	-16			
198	-26			
199	-37			
200	-48			
201	-59			
202	-69			
203	-80			
204	-91			
205	-101			

Table 4: Age model for Core GeoB8323-2

Depth (cm)	Date (CE)	Error (years)	*Material*	Source
206	-112			
207	-123			
208	-134			
209	-144			
210	-155			
211	-166			
212	-176			
213	-187			
214	-198			
215	-208			
216	-219			
217	-230			
218	-241			
219	-251			
220	-262			
221	-273			
222	-283			
223	-294			
224	-305			
225	-316			
226	-326			
227	-337	**35**	*gastropod*	Herbert and Compton (2007)

B Inorganic analysis

Table 5: Eigenvalues for end-member model numbers, from grain size analysis of GeoB8323-2

Number of EMs	R^2mean
2	0.560
3	0.704
4	0.734
5	0.750
6	0.782
7	0.803
8	0.823
9	0.843
10	0.849

Table 6: End-member model results from grain size analysis of GeoB8323-2

Depth (cm)	Date (CE)	1EM3	2EM3	3EM3
0	1950	0.556	0.000	0.444
1	1943	0.546	0.000	0.454
2	1935	0.494	0.000	0.506
3	1928	0.563	0.000	0.437
4	1921	0.468	0.000	0.532
5	1914	0.458	0.000	0.542
6	1906	0.468	0.000	0.532
7	1899	0.472	0.000	0.528
8	1892	0.406	0.000	0.594
10	1877	0.422	0.024	0.554
12	1863	0.460	0.092	0.447
13	1852	0.394	0.171	0.435
14	1850	0.445	0.070	0.484
15	1845	0.338	0.000	0.662
16	1840	0.444	0.032	0.524
17	1834	0.552	0.001	0.447
18	1829	0.387	0.135	0.478
19	1824	0.426	0.200	0.374
20	1819	0.436	0.294	0.270
21	1813	0.534	0.256	0.210
22	1808	0.694	0.132	0.174
23	1803	0.772	0.042	0.185
24	1798	0.782	0.041	0.177
25	1793	0.763	0.000	0.237
26	1787	0.743	0.070	0.187
27	1782	0.665	0.090	0.245

Table 6: End-member model results from grain size analysis of GeoB8323-2

Depth (cm)	Date (CE)	1EM3	2EM3	3EM3
28	1777	0.747	0.000	0.253
29	1772	0.764	0.000	0.236
31	1761	0.548	0.331	0.121
32	1756	0.714	0.097	0.188
33	1751	0.522	0.203	0.275
34	1746	0.503	0.178	0.319
35	1740	0.493	0.158	0.349
36	1735	0.571	0.135	0.294
37	1730	0.684	0.056	0.260
38	1725	0.696	0.056	0.248
39	1717	0.654	0.199	0.147
40	1705	0.776	0.053	0.171
41	1692	0.691	0.222	0.087
42	1680	0.436	0.487	0.077
43	1668	0.572	0.426	0.001
44	1655	0.680	0.270	0.051
45	1643	0.464	0.464	0.072
46	1631	0.314	0.686	0.000
47	1619	0.404	0.325	0.271
48	1606	0.555	0.395	0.050
49	1594	0.604	0.306	0.090
50	1582	0.323	0.450	0.227
51	1569	0.388	0.379	0.233
52	1557	0.039	0.706	0.255
53	1545	0.106	0.542	0.352
54	1532	0.068	0.490	0.442

Table 6: End-member model results from grain size analysis of GeoB8323-2

Depth (cm)	Date (CE)	1EM3	2EM3	3EM3
55	1520	0.045	0.605	0.351
56	1508	0.071	0.546	0.383
57	1495	0.031	0.492	0.476
58	1483	0.039	0.517	0.444
59	1471	0.084	0.411	0.506
60	1459	0.105	0.282	0.613
62	1434	0.112	0.412	0.475
63	1422	0.179	0.277	0.544
64	1409	0.271	0.089	0.640
65	1397	0.214	0.326	0.460
66	1385	0.280	0.273	0.447
67	1372	0.195	0.333	0.472
68	1360	0.200	0.356	0.443
69	1348	0.310	0.271	0.419
70	1335	0.133	0.535	0.332
71	1323	0.098	0.589	0.313
72	1311	0.106	0.479	0.415
73	1299	0.140	0.476	0.384
74	1286	0.106	0.550	0.344
75	1274	0.176	0.407	0.416
80	1212	0.000	0.529	0.471
81	1200	0.028	0.490	0.482
82	1188	0.037	0.429	0.535
83	1175	0.050	0.352	0.598
84	1163	0.192	0.300	0.508
85	1151	0.240	0.102	0.658

Table 6: End-member model results from grain size analysis of GeoB8323-2

Depth (cm)	Date (CE)	1EM3	2EM3	3EM3
86	1139	0.176	0.387	0.437
87	1126	0.120	0.288	0.592
88	1114	0.245	0.354	0.401
89	1102	0.264	0.440	0.296
90	1089	0.350	0.383	0.267
91	1077	0.158	0.549	0.293
92	1065	0.166	0.487	0.347
93	1052	0.087	0.489	0.424
94	1040	0.172	0.585	0.242
95	1028	0.056	0.429	0.515
96	1015	0.268	0.439	0.293
97	1003	0.074	0.269	0.656
98	991	0.203	0.276	0.520
99	979	0.202	0.347	0.451
100	966	0.111	0.401	0.488
101	954	0.079	0.630	0.290
102	942	0.152	0.471	0.377
103	929	0.052	0.432	0.516
104	917	0.000	0.654	0.346
105	905	0.136	0.575	0.290
106	892	0.036	0.683	0.282
107	880	0.000	0.601	0.399
108	868	0.000	0.653	0.347
109	855	0.147	0.516	0.337
110	843	0.085	0.597	0.318
111	837	0.042	0.598	0.360

Table 6: End-member model results from grain size analysis of GeoB8323-2

Depth (cm)	Date (CE)	1EM3	2EM3	3EM3
113	826	0.237	0.500	0.263
114	821	0.349	0.322	0.328
116	810	0.242	0.442	0.316
118	799	0.266	0.439	0.295
120	788	0.137	0.587	0.276
122	777	0.000	0.311	0.689
124	766	0.000	0.337	0.663
126	745	0.000	0.327	0.673
129	712	0.000	0.288	0.712
130	702	0.000	0.260	0.740
132	680	0.000	0.349	0.651
134	659	0.000	0.212	0.788
136	637	0.000	0.107	0.893
138	616	0.000	0.343	0.657
140	595	0.000	0.184	0.816
142	573	0.000	0.115	0.885
144	552	0.000	0.445	0.555
146	530	0.000	0.131	0.869
148	509	0.000	0.242	0.758
150	488	0.000	0.273	0.727
152	466	0.000	0.276	0.724
154	445	0.000	0.369	0.631
156	423	0.000	0.383	0.617
158	402	0.000	0.152	0.848
160	380	0.009	0.175	0.816
162	359	0.000	0.421	0.579

Table 6: End-member model results from grain size analysis of GeoB8323-2

Depth (cm)	Date (CE)	1EM3	2EM3	3EM3
164	338	0.000	0.305	0.695
166	316	0.000	0.470	0.530
168	295	0.000	0.367	0.633
170	273	0.000	0.137	0.863
172	252	0.000	0.462	0.538
174	231	0.000	0.493	0.507
176	209	0.000	0.469	0.531
178	188	0.000	0.173	0.827
180	166	0.000	0.407	0.593
182	145	0.098	0.187	0.715
184	123	0.043	0.124	0.833
186	102	0.048	0.000	0.952
188	81	0.142	0.097	0.762
190	59	0.000	0.319	0.681
196	-5	0.000	0.000	1.000
198	-26	0.000	0.000	1.000
200	-48	0.000	0.202	0.798
202	-69	0.026	0.000	0.974
204	-91	0.000	0.307	0.693
206	-112	0.000	0.567	0.433
208	-134	0.081	0.249	0.670
210	-155	0.000	0.167	0.833
212	-176	0.000	0.116	0.884
214	-198	0.000	0.086	0.914
216	-219	0.000	0.000	1.000
218	-241	0.000	0.000	1.000

Table 6: End-member model results from grain size analysis of GeoB8323-2

Depth (cm)	Date (CE)	1EM3	2EM3	3EM3
220	-262	0.000	0.000	1.000
222	-283	0.000	0.000	1.000
224	-305	0.000	0.000	1.000
226	-326	0.000	0.000	1.000

Table 7: End-member model classes from grain size analysis of GeoB8323-2

Class	Size (µm)	1EM3	2EM3	3EM3
F01	0.08	0.09	0.1	0.1
F02	0.30	0.09	0.07	0.13
F03	0.34	0.09	0.11	0.22
F04	0.38	0.16	0.18	0.22
F05	0.42	0.18	0.15	0.27
F06	0.47	0.19	0.15	0.33
F07	0.53	0.19	0.23	0.36
F08	0.60	0.23	0.23	0.41
F09	0.67	0.28	0.25	0.47
F10	0.75	0.29	0.29	0.56
F11	0.84	0.37	0.37	0.64
F12	0.95	0.43	0.42	0.77
F13	1.06	0.5	0.51	0.91
F14	1.19	0.6	0.62	1.09
F15	1.34	0.72	0.75	1.29
F16	1.50	0.83	0.9	1.52
F17	1.68	0.99	1.08	1.75
F18	1.89	1.13	1.28	2.01
F19	2.12	1.27	1.5	2.26
F20	2.38	1.43	1.73	2.52
F21	2.67	1.59	2	2.79
F22	2.99	1.76	2.25	3.03
F23	3.36	1.92	2.52	3.28
F24	3.77	2.09	2.79	3.49
F25	4.23	2.28	3.09	3.69
F26	4.74	2.46	3.37	3.88

Table 7: End-member model classes from grain size analysis of GeoB8323-2

Class	Size (µm)	1EM3	2EM3	3EM3
F27	5.32	2.66	3.65	4.03
F28	5.97	2.86	3.91	4.14
F29	6.70	3.08	4.15	4.23
F30	*7.52*	3.29	4.37	**4.26**
F31	*8.43*	3.53	4.56	**4.26**
F32	9.46	3.77	4.72	4.21
F33	10.62	4.02	4.83	4.12
F34	*11.91*	4.26	**4.87**	3.98
F35	13.37	4.5	4.85	3.82
F36	15.00	4.68	4.73	3.61
F37	16.83	4.78	4.53	3.36
F38	*18.88*	**4.82**	4.23	3.07
F39	21.19	4.74	3.88	2.74
F40	23.77	4.55	3.42	2.42
F41	26.67	4.24	2.93	2.08
F42	29.92	3.82	2.42	1.75
F43	33.58	3.35	1.92	1.43
F44	37.67	2.82	1.46	1.15
F45	42.27	2.28	1.07	0.91
F46	47.43	1.76	0.74	0.69
F47	53.21	1.3	0.5	0.5
F48	59.71	0.9	0.31	0.37
F49	66.99	0.61	0.19	0.27
F50	75.17	0.36	0.14	0.21
F51	84.34	0.24	0.12	0.14
F52	94.63	0.13	0.11	0.1

Table 7: End-member model classes from grain size analysis of GeoB8323-2

Class	Size (µm)	1EM3	2EM3	3EM3
F53	106.18	0.1	0.1	0.09
F54	119.13	0.1	0.13	0.03
F55	133.67	0.09	0.09	0
F56	149.98	0.08	0.06	0
F57	168.28	0.06	0.02	0
F58	188.81	0.03	0.01	0.01
F59	211.85	0.01	0.01	0.01
F60	237.70	0.01	0.01	0.01
F61	266.70	0.01	0.01	0.01
F62	299.25	0.01	0.01	0.01

Table 8: Elemental ratio values from GeoB8323-2

Depth (cm)	Date (CE)	K (cps)	Fe (cps)	**Fe/K**
1	1943	19764	74583	**3.77**
2	1935	16920	70310	**4.16**
3	1928	13534	68035	**5.03**
4	1921	13861	72808	**5.25**
5	1914	14408	83848	**5.82**
6	1906	14726	78388	**5.32**
7	1899	12461	70806	**5.68**
8	1892	12113	69302	**5.72**
9	1884	18903	83660	**4.43**
10	1877	15589	76111	**4.88**
11	1870	17805	76722	**4.31**
12	1859	17596	75707	**4.30**
13	1852	16115	71998	**4.47**
14	1850	17190	73998	**4.30**
15	1845	16309	74017	**4.54**
16	1840	13485	71615	**5.31**
17	1834	12561	65394	**5.21**
18	1829	15882	67202	**4.23**
19	1824	15519	63396	**4.09**
20	1819	15093	64246	**4.26**
21	1813	15371	61631	**4.01**
22	1808	15214	62496	**4.11**
23	1803	14240	60176	**4.23**
24	1798	15515	62631	**4.04**
25	1793	16014	64262	**4.01**
26	1787	15541	64017	**4.12**

Table 8: Elemental ratio values from GeoB8323-2

Depth (cm)	Date (CE)	K (cps)	Fe (cps)	**Fe/K**
27	1782	14379	60850	**4.23**
28	1777	14550	63427	**4.36**
29	1772	15373	62856	**4.09**
30	1767	14795	61944	**4.19**
31	1761	16077	64169	**3.99**
32	1756	15321	62378	**4.07**
33	1751	17020	65644	**3.86**
34	1746	14814	61846	**4.17**
35	1740	12747	59641	**4.68**
36	1735	15923	63625	**4.00**
37	1730	14340	59789	**4.17**
38	1725	15871	65959	**4.16**
39	1717	15389	64571	**4.20**
40	1705	16491	66137	**4.01**
41	1692	16193	66000	**4.08**
42	1680	15363	63779	**4.15**
43	1668	15055	63773	**4.24**
44	1655	16708	66651	**3.99**
45	1643	17210	69349	**4.03**
46	1631	16423	67341	**4.10**
47	1619	14746	66422	**4.50**
48	1606	16254	68095	**4.19**
49	1594	16185	67398	**4.16**
50	1582	16306	65894	**4.04**
51	1569	14250	61793	**4.34**
52	1557	15588	66993	**4.30**

Table 8: Elemental ratio values from GeoB8323-2

Depth (cm)	Date (CE)	K (cps)	Fe (cps)	**Fe/K**
53	1545	14783	66284	**4.48**
54	1532	18391	71264	**3.87**
55	1520	18726	69490	**3.71**
56	1508	18195	69302	**3.81**
57	1495	18710	71066	**3.80**
58	1483	19122	70027	**3.66**
59	1471	17745	69643	**3.92**
60	1459	18608	70081	**3.77**
61	1446	18038	69203	**3.84**
62	1434	18690	70871	**3.79**
63	1422	17432	68233	**3.91**
64	1409	18122	70469	**3.89**
65	1397	18346	71457	**3.89**
66	1385	18744	71718	**3.83**
67	1372	19058	71932	**3.77**
68	1360	19847	73470	**3.70**
69	1348	19278	72916	**3.78**
70	1335	19879	72673	**3.66**
71	1323	19321	71470	**3.70**
72	1311	19645	71430	**3.64**
73	1299	18118	70818	**3.91**
74	1286	17695	68145	**3.85**
75	1274	18810	71064	**3.78**
76	1262	14553	64914	**4.46**
77	1249	15460	66497	**4.30**
78	1237	15842	67973	**4.29**

Table 8: Elemental ratio values from GeoB8323-2

Depth (cm)	Date (CE)	K (cps)	Fe (cps)	**Fe/K**
79	1225	16920	67954	**4.02**
80	1212	16209	66732	**4.12**
81	1200	15078	65537	**4.35**
82	1188	16365	67494	**4.12**
83	1175	14414	63626	**4.41**
84	1163	13796	60468	**4.38**
86	1139	16368	66339	**4.05**
87	1126	17483	73355	**4.20**
88	1114	18769	73668	**3.92**
89	1102	19461	74515	**3.83**
90	1089	19066	72447	**3.80**
91	1077	19368	74315	**3.84**
92	1065	19463	75926	**3.90**
93	1052	19336	75283	**3.89**
94	1040	18117	74367	**4.10**
95	1028	19422	73311	**3.77**
96	1015	18916	72461	**3.83**
97	1003	19320	71133	**3.68**
98	991	18743	72147	**3.85**
99	979	19313	72274	**3.74**
100	966	18472	71763	**3.88**
101	954	17939	69985	**3.90**
102	942	19250	72659	**3.77**
103	929	19586	73720	**3.76**
104	917	19101	71901	**3.76**
105	905	19670	71907	**3.66**

Table 8: Elemental ratio values from GeoB8323-2

Depth (cm)	Date (CE)	K (cps)	Fe (cps)	**Fe/K**
106	892	19250	70966	**3.69**
107	880	19808	71377	**3.60**
108	868	18654	67657	**3.63**
109	855	19103	68487	**3.59**
110	843	18370	68363	**3.72**
111	837	18593	68474	**3.68**
112	832	18797	68026	**3.62**
113	826	19961	72231	**3.62**
114	821	20185	71364	**3.54**
115	815	20632	73391	**3.56**
116	810	20579	74885	**3.64**
117	804	20233	74416	**3.68**
118	799	20584	74966	**3.64**
119	793	20275	74260	**3.66**
120	788	20312	73524	**3.62**
121	782	20410	74774	**3.66**
122	777	19055	73352	**3.85**
123	771	19806	74050	**3.74**
124	766	18897	74497	**3.94**
125	755	19256	74779	**3.88**
126	745	19463	73160	**3.76**
127	734	21878	76127	**3.48**
128	723	21334	76190	**3.57**
129	712	20787	74149	**3.57**
130	702	19314	71326	**3.69**
131	691	20315	72975	**3.59**

Table 8: Elemental ratio values from GeoB8323-2

Depth (cm)	Date (CE)	K (cps)	Fe (cps)	**Fe/K**
132	680	19166	72778	**3.80**
133	670	20511	74386	**3.63**
134	659	20421	75866	**3.72**
135	648	20693	74759	**3.61**
136	637	19819	75377	**3.80**
137	627	20252	74504	**3.68**
138	616	19526	72366	**3.71**
139	605	20580	72817	**3.54**
140	595	21599	73219	**3.39**
141	584	20338	67544	**3.32**
142	573	21103	73567	**3.49**
143	563	21331	73957	**3.47**
144	552	20828	72530	**3.48**
145	541	20897	73267	**3.51**
146	530	21003	73547	**3.50**
147	520	21216	73439	**3.46**
148	509	21461	73862	**3.44**
149	498	21285	73934	**3.47**
150	488	19405	68963	**3.55**
151	477	19639	69980	**3.56**
152	466	20422	70523	**3.45**
153	455	19797	69785	**3.53**
154	445	20012	70631	**3.53**
155	434	20642	71157	**3.45**
156	423	19727	69572	**3.53**
157	413	19755	71302	**3.61**

Table 8: Elemental ratio values from GeoB8323-2

Depth (cm)	Date (CE)	K (cps)	Fe (cps)	**Fe/K**
158	402	19427	68550	**3.53**
159	391	19474	69690	**3.58**
160	380	19399	69247	**3.57**
161	370	19126	69090	**3.61**
162	359	19694	69302	**3.52**
163	348	19915	70620	**3.55**
164	338	19684	69964	**3.55**
165	327	20133	71029	**3.53**
166	316	19697	71364	**3.62**
167	306	20336	71315	**3.51**
168	295	19745	71234	**3.61**
169	284	19295	70880	**3.67**
170	273	19155	69254	**3.62**
171	263	19486	70823	**3.63**
172	252	19023	69814	**3.67**
173	241	19220	70701	**3.68**
174	231	19642	70463	**3.59**
175	220	18917	69621	**3.68**
176	209	18474	68818	**3.73**
177	198	17802	62922	**3.53**
178	188	18787	67520	**3.59**
179	177	19794	71863	**3.63**
180	166	19093	71591	**3.75**
181	156	19192	72391	**3.77**
182	145	19750	72976	**3.69**
183	134	19496	74132	**3.80**

Table 8: Elemental ratio values from GeoB8323-2

Depth (cm)	Date (CE)	K (cps)	Fe (cps)	**Fe/K**
184	123	17712	68869	**3.89**
186	102	19889	77240	**3.88**
187	91	19308	76521	**3.96**
188	81	19892	76178	**3.83**
189	70	20119	77774	**3.87**
190	59	19947	77035	**3.86**
191	49	19045	73465	**3.86**
192	38	19276	75918	**3.94**
193	27	19324	75840	**3.92**
194	16	20280	77617	**3.83**
195	6	19986	76736	**3.84**
196	-5	19399	75200	**3.88**
197	-16	20251	76427	**3.77**
198	-26	20614	75777	**3.68**
199	-37	20286	75055	**3.70**
200	-48	20319	74312	**3.66**
201	-59	21013	75829	**3.61**
202	-69	20803	75008	**3.61**
203	-80	21090	74994	**3.56**
204	-91	20622	74469	**3.61**
205	-101	20468	74277	**3.63**
206	-112	21360	74828	**3.50**
207	-123	20709	73025	**3.53**
208	-134	20847	71920	**3.45**
209	-144	21216	74014	**3.49**
210	-155	21009	73367	**3.49**

Table 8: Elemental ratio values from GeoB8323-2

Depth (cm)	Date (CE)	K (cps)	Fe (cps)	**Fe/K**
211	-166	21208	73266	**3.45**
212	-176	20113	70511	**3.51**
213	-187	21449	72595	**3.38**
214	-198	22634	75060	**3.32**
215	-208	21783	72534	**3.33**
216	-219	21757	72683	**3.34**
217	-230	22680	73680	**3.25**
218	-241	22093	74093	**3.35**
219	-251	22693	74699	**3.29**
220	-262	22300	75038	**3.36**
221	-273	22035	74285	**3.37**
222	-283	20973	71456	**3.41**
223	-294	22113	74355	**3.36**
224	-305	21195	72758	**3.43**
225	-316	21442	74430	**3.47**
226	-326	21309	73524	**3.45**
227	-337	21280	74597	**3.51**

C Organic analysis

Table 9: Abundance measurements from GeoB8323-2

Depth (cm)	Age (CE)	Concentration (ng/g)						CPI (27-33)	ACL (27-33)
		nC29	**SD**	**nC31**	**SD**	**nC33**	**SD**		
1	1950	***573***	**59**	***2512***	**278**	***1083***	**143**	15.4	31.1
5	1914	***600***	**54**	***2693***	**260**	***1189***	**137**	15.3	31.1
11	1866.5	***607***	**74**	***2778***	**361**	***1254***	**195**	15.3	31.1
15	1845	***492***	**54**	***2094***	**247**	***913***	**129**	14.4	31.1
20	1819	***864***	**87**	***3272***	**352**	***1401***	**181**	13.5	31.0
25	1793	***822***	**109**	***2828***	**402**	***1261***	**214**	11.4	30.9
30	1767	***595***	**59**	***2046***	**218**	***894***	**114**	13.3	30.9
35	1740	***795***	**95**	***2956***	**379**	***1408***	**216**	13.2	31.0
40	1717	***602***	**74**	***2128***	**279**	***951***	**149**	13.7	30.9
44	1655	***783***	**90**	***2815***	**348**	***1272***	**188**	13.1	31.0
50	1582	***821***	**95**	***3098***	**385**	***1460***	**217**	13.3	31.0
55	1520	***838***	**79**	***3059***	**307**	***1414***	**170**	13.1	31.0
60	1459	***596***	**69**	***2160***	**267**	***969***	**143**	12.4	31.0
64	1409	***1020***	**127**	***3720***	**495**	***1721***	**274**	12.8	31.0
70	1335	***1050***	**128**	***3892***	**506**	***1827***	**285**	12.2	31.0
74	1286	***392***	**50**	***1444***	**195**	***607***	**98**	12.4	30.9
80	1212	***885***	**114**	***3407***	**471**	***1623***	**269**	13.2	31.0
86	1139	***563***	**47**	***2138***	**192**	***1019***	**110**	13.4	31.0
90	1089	***562***	**63**	***2143***	**255**	***1001***	**143**	13.4	31.0
95	1028	***776***	**65**	***2957***	**265**	***1341***	**144**	12.7	31.0
100	966	***645***	**60**	***2421***	**240**	***1118***	**133**	12.7	31.0
105	905	***814***	**69**	***3226***	**293**	***1558***	**170**	13.3	31.0

Table 9: Abundance measurements from GeoB8323-2

Depth (cm)	Age (CE)	Concentration (ng/g)						CPI (27-33)	ACL (27-33)
110	843	***529***	**58**	***1990***	**235**	***906***	**128**	13.2	31.0
120	788	***727***	**47**	***2894***	**201**	***1346***	**112**	12.7	31.0
125	755	***454***	**46**	***1826***	**198**	***858***	**111**	13.0	31.0
130	702	***328***	**36**	***1362***	**159**	***660***	**92**	13.5	31.1
134	659	***1032***	**117**	***4190***	**510**	***1984***	**289**	13.8	31.1
140	595	***413***	**34**	***1618***	**141**	***708***	**74**	14.0	31.0
144	552	***550***	**47**	***2118***	**194**	***964***	**106**	13.0	31.0
150	488	***300***	**24**	***1125***	**97**	***521***	**54**	12.1	31.0
160	380	***1038***	**96**	***3855***	**382**	***1833***	**218**	12.2	31.0
170	273	***829***	**67**	***2983***	**258**	***1438***	**149**	11.5	31.0
180	166	***538***	**56**	***1876***	**209**	***897***	**119**	12.0	31.0
190	59	***828***	**88**	***3019***	**344**	***1423***	**194**	11.9	31.0
200	-48	***904***	**85**	***3432***	**346**	***1605***	**194**	11.9	31.0
210	-155	***559***	**53**	***1958***	**200**	***875***	**107**	12.2	30.9
220	-262	***599***	**51**	***2094***	**189**	***965***	**104**	13.0	31.0

Table 10: Carbon isotope results from GeoB8323-2

Depth (cm)	Date (CE)	$\delta^{13}C_{29}$ (‰)	σ (29) (‰)	$\delta^{13}C_{31}$ (‰)	σ (31) (‰)	$\delta^{13}C_{33}$ (‰)	σ (33) (‰)
0.5	1950	***-27.8***	0.3	*-26.4*	0.1	*-24.6*	0.1
5	1914	***-28.4***	0.1	*-26.5*	0.2	*-24.8*	0.1
11.5	1867	***-28.7***	0.3	*-26.0*	0.1	*-24.5*	0.3
15	1845	***-27.9***	0.4	*-26.5*	0.1	*-24.7*	0.3
20	1819	***-28.6***	0.1	*-26.5*	0.2	*-25.2*	0.6
25	1793	***-27.6***	0.2	*-25.9*	0.0	*-23.8*	0.2
30	1767	***-27.9***	0.2	*-25.6*	0.1	*-24.1*	0.4
35	1740	***-27.7***	0.1	*-26.2*	0.0	*-24.3*	0.0
40	1717	***-28.1***	0.2	*-26.0*	0.2	*-24.3*	0.1
44	1655	***-27.3***	0.3	*-25.9*	0.0	*-24.0*	0.1
50	1582	***-27.6***	0.0	*-26.1*	0.1	*-23.6*	0.2
55	1520	***-27.7***	0.1	*-26.0*	0.1	*-24.0*	0.4
60	1459	***-27.7***	0.4	*-26.1*	0.1	*-24.2*	0.2
64	1409	***-27.5***	0.2	*-26.0*	0.2	*-24.8*	0.2
70	1335	***-27.8***	0.4	*-26.1*	0.1	*-24.8*	0.2
74	1286	***-27.9***	0.1	*-25.9*	0.0	*-24.2*	0.1
80	1212	***-28.5***	0.1	*-25.7*	0.1	*-24.4*	0.1
86	1139	***-28.0***	0.1	*-25.8*	0.2	*-24.3*	0.2
90	1089	***-27.7***	0.4	*-25.7*	0.1	*-24.4*	0.1
95	1028	***-27.6***	0.2	*-26.0*	0.3	*-24.1*	0.4
100	966	***-27.8***	0.3	*-26.0*	0.1	*-24.1*	0.1
105	905	***-27.9***	0.2	*-25.7*	0.2	*-24.5*	0.1
110	843	***-27.8***	0.1	*-26.0*	0.1	*-24.4*	0.2
120	788	***-26.9***	0.1	*-26.0*	0.2	*-24.3*	0.4
125	755	***-27.9***	0.0	*-26.0*	0.1	*-24.3*	0.0

Table 10: Carbon isotope results from GeoB8323-2

Depth (cm)	Date (CE)	$\delta^{13}C_{29}$ (‰)	σ (29) (‰)	$\delta^{13}C_{31}$ (‰)	σ (31) (‰)	$\delta^{13}C_{33}$ (‰)	σ (33) (‰)
130	702	***-27.7***	0.2	*-26.1*	0.1	*-24.1*	0.2
134	659	***-27.3***	0.2	*-26.0*	0.1	*-24.6*	0.2
140	595	***-27.5***	0.3	*-26.0*	0.1	*-24.1*	0.3
144	552	***-27.8***	0.4	*-25.9*	0.0	*-24.3*	0.1
150	488	***-27.5***	0.2	*-25.9*	0.0	*-24.4*	0.1
160	380	***-28.1***	0.1	*-25.9*	0.0	*-24.1*	0.0
170	273	***-28.0***	0.1	*-25.5*	0.2	*-23.7*	0.3
180	166	***-27.6***	0.0	*-25.6*	0.1	*-23.7*	0.3
190	59	***-27.5***	0.1	*-26.1*	0.0	*-23.9*	0.0
200	-48	***-27.7***	0.2	*-26.1*	0.1	*-24.3*	0.2
210	-155	***-27.7***	0.4	*-26.2*	0.0	*-24.3*	0.2
220	-262	***-27.9***	0.1	*-26.1*	0.2	*-24.6*	0.1

Table 11: Hydrogen isotope results from GeoB8323-2

Depth (cm)	Date (CE)	$\delta\mathbf{D_{29}}$ **(‰)**	σ (29) (‰)	δD_{31} (‰)	σ (31) (‰)	δD_{33} (‰)	σ (33) (‰)
0.5	1950	***-131***	1	*-137*	1	*-137*	1
5	1914	***-131***	4	*-134*	1	*-137*	0
11.5	1866.5	***-138***	1	*-136*	2	*-142*	1
15	1845	***-133***	2	*-134*	1	*-137*	1
20	1819	***-134***	0	*-135*	1	*-135*	2
25	1793	***-137***	3	*-135*	0	*-138*	0
30	1767	***-137***	1	*-139*	1	*-138*	1
35	1740	***-138***	1	*-140*	1	*-139*	2
40	1717	***-140***	1	*-142*	1	*-144*	0
44	1655	***-139***	2	*-138*	1	*-140*	3
50	1582	***-134***	3	*-136*	1	*-139*	2
55	1520	***-138***	3	*-140*	1	*-140*	2
60	1459	***-138***	0	*-139*	0	*-140*	3
64	1409	***-135***	3	*-138*	0	*-139*	2
70	1335	***-138***	1	*-139*	1	*-140*	0
74	1286	***-145***	1	*-143*	0	*-143*	0
80	1212	***-134***	2	*-141*	3	*-138*	1
86	1139	***-142***	2	*-141*	2	*-144*	3
90	1089	***-141***	0	*-141*	2	*-143*	1
95	1028	***-138***	1	*-139*	0	*-138*	3
100	966	***-142***	0	*-141*	0	*-143*	1
105	905	***-138***	2	*-142*	1	*-140*	0
110	843	***-139***	1	*-141*	0	*-140*	1
120	788	***-139***	2	*-139*	1	*-139*	2
125	755	***-141***	0	*-140*	1	*-142*	0

Table 11: Hydrogen isotope results from GeoB8323-2

Depth (cm)	Date (CE)	$\delta\mathbf{D_{29}}$ **(‰)**	σ (29) (‰)	δD_{31} (‰)	σ (31) (‰)	δD_{33} (‰)	σ (33) (‰)
130	702	***-135***	1	*-136*	0	*-138*	1
134	659	***-134***	1	*-136*	0	*-139*	1
140	595	***-141***	0	*-141*	0	*-142*	0
144	552	***-140***	1	*-139*	1	*-141*	1
150	488	***-142***	0	*-140*	1	*-140*	1
160	380	***-138***	1	*-135*	1	*-139*	1
170	273	***-140***	1	*-138*	2	*-141*	1
180	166	***-141***	0	*-142*	0	*-144*	0
190	59	***-141***	0	*-141*	1	*-142*	1
200	-48	***-140***	0	*-140*	0	*-139*	2
210	-155	***-143***	1	*-140*	0	*-140*	1
220	-262	***-140***	1	*-140*	2	*-142*	0

Table 12: Apparent fractionations between leaf wax and source water compared between taxanomic categories (adapted from Sachse et al. 2012).

	eC$_{29}$/MAP (‰)				
Plant group	**Median δD**	**S.D.**	**n**	**95% C.I.**	**% Sample**
C_3 gymnosperms	*-110*	*24*	*15*	*12*	
C_3 dicots	*-118*	*30*	*168*	*4*	
C_3 weighted average	-113	18	183		50
C_4 monocots (e.g. grasses)	-139	25	56	7	20
CAM (monocots & dicots)	-114	22	17		30
Mixed vegetation ϵ estimate	-118	12			
Core-top δD	-131				

Table 13: SST results from alkenone analysis of GeoB8323-2

Depth (cm)	Date (CE)	C37:3	C37:2	*UK'37*	σUK'37	**SST (°C)**	σ SST (°C)
5	1914	527	565	*0.517*	0.000	**14.35**	0.00
11.5	1867	483	473	*0.494*	0.003	**13.64**	0.08
15	1845	402	362	*0.473*	0.004	**12.99**	0.13
20	1819	692	574	*0.454*	0.005	**12.41**	0.15
25	1793	1172	1053	*0.474*	0.005	**13.03**	0.14
30	1767	526	480	*0.477*	0.000	**13.13**	0.01
35	1740	728	665	*0.477*	0.004	**13.11**	0.12
40	1717	365	317	*0.465*	-	**12.76**	-
44	1655	832	660	*0.442*	0.000	**12.07**	0.01
50	1582	662	453	*0.407*	0.003	**11.01**	0.10
55	1520	625	714	*0.534*	0.003	**14.84**	0.09
60	1459	763	686	*0.472*	0.004	**12.97**	0.12
64	1409	552	477	*0.464*	0.000	**12.71**	0.01
70	1335	692	716	*0.509*	0.004	**14.10**	0.12
74	1286	634	756	*0.543*	0.002	**15.13**	0.06
80	1212	456	468	*0.507*	0.004	**14.03**	0.11
86	1139	363	334	*0.479*	0.001	**13.19**	0.04
90	1089	520	688	*0.568*	0.005	**15.88**	0.16
95	1028	612	517	*0.457*	0.004	**12.51**	0.12
100	966	494	448	*0.474*	0.004	**13.04**	0.14
103	929	335	424	*0.559*	0.002	**15.60**	0.06
105	905	559	702	*0.556*	0.001	**15.52**	0.04
107	880	414	600	*0.592*	0.002	**16.60**	0.05
110	843	591	764	*0.564*	0.002	**15.77**	0.06
112	832	436	570	*0.567*	0.007	**15.85**	0.21
115	815	742	822	*0.526*	0.000	**14.60**	0.01

Table 13: SST results from alkenone analysis of GeoB8323-2

Depth (cm)	Date (CE)	C37:3	C37:2	*UK'37*	σUK'37	**SST (°C)**	σ SST (°C)
120	788	371	424	*0.534*	0.005	**14.85**	0.15
125	755	517	640	*0.553*	0.001	**15.43**	0.04
130	702	228	309	*0.576*	0.005	**16.12**	0.16
134	659	368	328	*0.473*	0.006	**13.01**	0.18
140	595	317	273	*0.463*	0.001	**12.70**	0.02
144	552	307	379	*0.552*	0.000	**15.40**	0.01
150	488	259	359	*0.581*	0.001	**16.28**	0.03
160	380	377	380	*0.503*	0.005	**13.91**	0.14
170	273	355	323	*0.477*	0.002	**13.13**	0.06
180	166	552	498	*0.475*	0.005	**13.07**	0.14
190	59	669	728	*0.522*	0.004	**14.49**	0.11
200	-48	600	713	*0.544*	0.004	**15.15**	0.13
210	-155	272	322	*0.271*	-	**15.11**	-
220	-262	466	601	*0.563*	0.001	**15.74**	0.02

Table 14: TEX86 and BIT values from GeoB8323-2

Date (CE)	GDGT 0	GDGT 1	GDGT 2	GDGT 3	GDGT 4	GDGT 4'	TEX_{86}	SST (°C)	IS	I	II	III	BIT
	1302	**1300**	**1298**	**1296**	**1292**	**1292**			**744**	**1050**	**1036**	**1022**	
1914	5524005	616292	299212	91444	4286576	92894	*0.44*	**14.19**	424019	615780	321491	217014	**0.21**
1867	4044123	377169	181407	53799	3107564	62891	*0.44*	**14.31**	127976	232361	148560	99264	**0.13**
1845	2879569	254715	138585	36069	2404131	46858	*0.47*	**15.86**	77930	151687	96918	74731	**0.12**
1819	4009919	367486	173668	48698	2807046	71344	*0.44*	**14.50**	146959	233491	149673	114218	**0.15**
1793	4970358	492435	238406	68607	3750944	91250	*0.45*	**14.69**	174745	465442	259222	178674	**0.19**
1767	4679906	446675	218215	65638	3588741	82672	*0.45*	**14.93**	142784	319490	180254	110648	**0.15**
1767	4943056	471321	228388	69429	3693950	91517	*0.45*	**15.04**	157338	351468	196001	107333	**0.15**
1740	3498432	333649	172960	44439	2917258	56634	*0.45*	**14.94**	138074	280062	152211	89753	**0.15**
1717	3715321	336747	153659	63666	2967118	68616	*0.46*	**15.48**	100770	308491	162646	93514	**0.16**
1655	3708466	341445	164212	47763	3008322	70048	*0.45*	**15.03**	152043	278859	150719	94573	**0.15**
1582	3782331	344425	148997	49103	2932123	79271	*0.45*	**14.62**	168663	235722	149098	91740	**0.14**
1520	6273428	634723	291362	84832	4616513	90292	*0.42*	**13.08**	506193	448193	284541	193151	**0.17**
1459	1877218	157559	74839	20828	1669042	37269	*0.46*	**15.38**	144231	120798	79497	50499	**0.13**
1409	2259660	187845	87845	24752	1915272	35885	*0.44*	**14.31**	91754	132370	84340	54829	**0.12**
1335	3370898	294804	152371	40550	2633239	56522	*0.46*	**15.42**	174755	224975	139475	94175	**0.15**
1286	4055058	378299	175907	48160	3019857	60970	*0.43*	**13.51**	278854	210815	148163	91672	**0.13**
1212	6164243	600939	296395	94445	4861040	160817	*0.48*	**16.71**	95798	324725	226521	150139	**0.13**

Table 14: TEX86 and BIT values from GeoB8323-2

Date (CE)	GDGT 0	GDGT 1	GDGT 2	GDGT 3	GDGT 4	GDGT 4'	TEX_{86}	SST (°C)	IS	I	II	III	BIT
1139	4440050	435288	196625	61274	3587302	81666	*0.44*	**14.09**	185521	261307	177231	113369	**0.13**
1089	7276388	761740	351395	109573	5156591	143444	*0.44*	**14.38**	346598	451883	328829	216225	**0.16**
1028	4085371	382532	182273	55520	3252908	72314	*0.45*	**14.73**	247658	214846	150495	97042	**0.12**
966	4339516	397194	206712	61250	3837256	85722	*0.47*	**16.24**	252093	256148	175085	112219	**0.12**
905	7210112	722149	346974	109086	5069189	134262	*0.45*	**14.87**	394349	370099	277697	186958	**0.14**
843	9667151	1214725	577012	174430	6829089	173022	*0.43*	**13.68**	435863	574407	416903	279811	**0.16**
815	10420262	1754394	722398	225292	6869195	274851	*0.41*	**12.16**	625531	786289	505726	329440	**0.19**
788	7749743	850205	395585	126804	5569950	153122	*0.44*	**14.40**	763663	579038	395205	251945	**0.18**
755	6551800	687377	329672	101480	4910998	134563	*0.45*	**14.98**	599275	541442	365948	250247	**0.19**
702	7407329	762912	358679	110238	5082613	143904	*0.45*	**14.58**	741818	644836	470787	328710	**0.22**
659	4180533	366414	181418	53780	3319246	72738	*0.46*	**15.31**	221136	270171	180543	122515	**0.15**
595	4144002	375416	181626	55602	3240508	66788	*0.45*	**14.71**	383236	290382	203849	149397	**0.17**
552	7039327	739305	356872	111561	5128486	144999	*0.45*	**15.11**	852208	608806	444976	313455	**0.21**
488	5498428	524727	230212	71556	3591694	88122	*0.43*	**13.27**	686757	560142	342476	234896	**0.24**
380	3455587	316786	153222	45656	2893157	61346	*0.45*	**14.94**	247190	247704	154325	98266	**0.15**
273	6557712	666276	320360	102220	5032733	154116	*0.46*	**15.79**	398063	392023	277346	182953	**0.14**
166	5970750	586512	286070	86300	4568737	110166	*0.45*	**14.97**	262674	393944	251793	158813	**0.15**
59	5448882	598477	276108	84528	4178244	136414	*0.45*	**15.12**	521011	516886	350668	227960	**0.21**

Table 14: TEX86 and BIT values from GeoB8323-2

Date (CE)	GDGT 0	GDGT 1	GDGT 2	GDGT 3	GDGT 4	GDGT 4'	TEX_{86}	SST (°C)	IS	I	II	III	BIT
-48	7182143	721884	343838	102800	5132307	132537	*0.45*	**14.56**	734841	630510	433208	285394	**0.21**
-48	8857873	858335	414064	125417	6897727	166828	*0.45*	**14.97**	831595	745965	515267	343039	**0.19**
-155	8502929	935058	474207	128018	6149010	245322	*0.48*	**16.51**	791875	736006	524733	365323	**0.21**
-262	3752335	330503	152519	46978	2969345	60801	*0.44*	**14.25**	333899	240222	187655	137436	**0.16**

Table 15: Comparison between alkenone and TEX86 SST and the resulting upwelling index ΔT

Age (CE)	$SST_{UK'37}$ (°C)	SST_{TEX86} (°C)	**TEX-UK'37 (ΔT)**
1914	14.19	14.35	**-0.16**
1867	14.31	13.64	**0.67**
1845	15.86	12.99	**2.87**
1819	14.50	12.41	**2.08**
1793	14.69	13.03	**1.66**
1767	15.04	13.13	**1.91**
1740	14.94	13.11	**1.83**
1717	15.48	12.76	**2.72**
1655	15.03	12.07	**2.96**
1582	14.62	11.01	**3.61**
1520	13.08	14.84	**-1.75**
1459	15.38	12.97	**2.41**
1409	14.31	12.71	**1.60**
1335	15.42	14.10	**1.33**
1286	13.51	15.13	**-1.63**
1212	16.71	14.03	**2.68**
1139	14.09	13.19	**0.91**
1089	14.38	15.88	**-1.51**
1028	14.73	12.51	**2.22**
966	16.24	13.04	**3.19**
929		15.60	
905	14.87	15.52	**-0.66**
880		16.60	
843	13.68	15.77	**-2.09**
832		15.85	
815	12.16	14.60	**-2.44**

Table 15: Comparison between alkenone and TEX86 SST and the resulting index ΔT

Age (CE)	$SST_{UK'37}$ (°C)	SST_{TEX86} (°C)	**TEX-UK'37 (ΔT)**
788	14.40	14.85	**-0.45**
755	14.98	15.43	**-0.46**
702	14.58	16.12	**-1.54**
659	15.31	13.01	**2.31**
595	14.71	12.70	**2.01**
552	15.11	15.40	**-0.29**
488	13.27	16.28	**-3.01**
380	14.94	13.91	**1.03**
273	15.79	13.13	**2.66**
166	14.97	13.07	**1.90**
59	15.12	14.49	**0.63**
-48	14.56	15.15	**-0.60**
-155	16.51	15.11	**1.40**
-262	14.25	15.74	**-1.49**